Novel THz-based concepts for synchronization and diagnostics at 4th generation THz lightsources

vorgelegt von
M. Sc.
Min Chen
ORCID: 0000-0001-5230-360X

an der Fakultät II - Mathematik und Naturwissenschaften
der Technischen Universität Berlin
zur Erlangung des akademischen Grades

Doktor der Naturwissenschaften
- Dr. rer. nat. -

genehmigte Dissertation

Promotionsausschuss:

Vorsitzender: Prof. Dr. Andreas Knorr
Gutachter: Prof. Dr. Michael Gensch
Gutachter: Prof. Dr. Simon Elliot Wall
Gutachter: Prof. Dr. Thomas Cowan

Tag der wissenschaftlichen Aussprache: 03. Mai 2022

Berlin 2022

Abstract

Pump-probe experiments using ultrashort light pulses are an important method for investigating ultrafast dynamic processes in matter. Here, high-field terahertz (THz) pulses have become indispensable for selectively pumping technologically relevant low-energy degrees of freedom, such as plasmons, phonons, and magnons. Compared to the commonly used laser-based THz sources, *electron accelerator*-based sources can have significant advantages, i.e., higher pulse energy, repetition rate, spectral density, and tuning range of the emitted THz radiation. These unique advantages make accelerator-based THz sources largely superior for exploring intense THz interaction with matter leading to technologically relevant phenomena such as THz high harmonic generation (HHG), ultrafast spin dynamics, coherent control of molecular orientation/vibration, etc. However, because of the complexity of modern accelerators, precise synchronization – corresponding to the femtosecond timescale of the investigated physical processes – between accelerator-based radiation and external laser systems is highly challenging.

In this thesis, a set of techniques for achieving ultra-precise synchronization is demonstrated to increase the temporal resolution of pump-probe experiments that combine accelerator-based THz sources with table-top laser systems. These techniques further enable comprehensive diagnostics of electron bunch properties and accelerator instabilities. The first one is the double-Arrival Time Monitor (ATM)-based pulse- and field-resolved arrival time correction technique, which is an advancement of the established pulse-resolved *post mortem* data sorting technique at the TELBE THz facility. The new scheme provides real-time information about the properties of individual pulses from all TELBE THz sources, including pulse arrival time, intensity, and THz frequency. It increases the pulse to pulse temporal resolution from 50 fs (RMS) (achieved by the single ATM) to 25 fs (RMS) in THz time-domain spectroscopy (TDS) experiments, when the initial timing jitter is about 500 fs (RMS).

This thesis also demonstrates the successful implementation of the THz-slicing method-based all-optical passive synchronization method, enabling fs-level synchronization between two independent optical sources. The feasibility of this THz-slicing method is first shown using a table-top setup with two mode-locked laser systems. Its performance is further characterized by several benchmark experiments at the high-field THz user facility TELBE. In a THz-TDS benchmark experiment, the 540 fs (RMS) timing jitter is suppressed by the THz-slicing technique to around 44 fs (RMS). Most importantly, this method enables – for the first time – the successful operation of a THz time-domain Scattering-type Scanning Near-field Optical Microscopy (s-SNOM) experiment in conjunction with the accelerator-based THz radiation from the TELBE source, yielding a spatial resolution on the order of 100 nm when the sample is irradiated by a THz pulse with a central frequency of 0.9 THz. This achievement paves the

way for other ultrafast techniques that require heterodyne detection or long signal acquisition times at accelerator-based THz sources.

Zusammenfassung

Ultraschnelle Pump-Probe-Experimente mit ultrakurzen Lichtpulsen sind eine wichtige Methode um ultraschnelle dynamische Prozesse in Materie zu untersuchen. Hier sind Hochfeld-Terahertz (THz)-Pulse unverzichtbar geworden, um technologisch relevante niederenergetische Freiheitsgrade, wie Plasmonen, Phononen und Magnonen, selektiv anzuregen. Im Vergleich zu den üblicherweise verwendeten laserbasierten THz-Quellen weisen Quellen auf Basis von *Elektronenbeschleunigern* signifikante Vorteile auf, wie z.B. höhere Pulsenergie, Wiederholrate, spektrale Dichte und abstimmbarer Frequenzbereich der emittierten THz-Strahlung. Diese einzigartigen Vorteile machen beschleunigerbasierte THz-Quellen höchst attraktiv für die Erforschung der Wechselwirkung von Materie mit intensiver THz-Strahlung. Typische Experimente und Untersuchung sind z.B. THz High Harmonic Generation (HHG), ultraschnelle Spindynamik oder die kohärente Kontrolle der molekularen Orientierung/Schwingung. Aufgrund der Komplexität moderner Beschleunigeranlagen ist die präzise Synchronisation – entsprechend der charakteristischen Femtosekunden-Dynamik der untersuchten physikalischen Prozesse – zwischen beschleunigerbasierter Strahlung und externen Lasersystemen eine große Herausforderung.

Um die zeitliche Auflösung von Pump-Probe-Experimenten zu erhöhen, bei denen beschleunigerbasierte THz-Quellen mit Tabletop-Lasersystemen kombiniert werden, wurde in dieser Arbeit zwei Methoden zur Erzielung ultrapräziser Synchronisation entwickelt und demonstriert. Die zugrundeliegenden Techniken ermöglichen zusätzlich eine umfassende Diagnostik der Eigenschaften von Elektronenpaketen und Beschleunigerinstabilitäten. Die erste Methode ist die auf einem doppelten Ankunftszeitmonitor (ATM) basierende puls- und feldaufgelöste Ankunftszeitkorrekturtechnik, die eine Weiterentwicklung der etablierten pulsaufgelösten *post mortem*-Datensortierungstechnik an der TELBE-THz-Anlage ist. Das neue Verfahren liefert Echtzeitinformationen über die Eigenschaften einzelner THz-Pulse aus dem Beschleuniger, einschließlich der Ankunftszeit, Intensität und Frequenz der THz-Pulse. Es erhöht die zeitliche Puls-zu-Puls-Auflösung von 50 fs (RMS) (erreicht durch den einzelnen ATM) auf 25 fs (RMS) in THz-Zeitbereichsspektroskopie (TDS)-Experimenten, wenn der anfängliche Timing-Jitter etwa 500 fs (RMS) beträgt.

Die zweite Methode ist die neu entwickelte, vollständig optisch passive Synchronisationsmethode, die auf einem THz-slicing genannten Prozess beruht. Die Methode ermöglischt die Synchronisation auf fs-Niveau zwischen zwei unabhängigen optischen Quellen ermöglicht. Die Machbarkeit dieser THz-Slicing-Methode wird zunächst anhand eines Testexperiments mit zwei modengekoppelten Lasersystemen gezeigt. Ihre Leistungsfähigkeit wird durch mehrere Benchmark-Experimente an der Hochfeld-THz-Anlage TELBE weiter charakterisiert. In einem THz-TDS-Benchmark-Experiment wird der 540 fs (RMS) Timing-Jitter durch die THz-Slicing-

Technik auf etwa 44 fs (RMS) reduziert. Vor allem aber ermöglicht diese Methode zum ersten Mal den erfolgreichen Betrieb eines *THz-Zeitbereichs* Scattering-type Scanning Near-field Optical Microscopy (s-SNOM)-Experiments in Verbindung mit der beschleunigerbasierten THz-Strahlung der TELBE-Quelle. Hiermit wird die zeitaufgelöste THz-Spektroskopie mit einer räumlichen Auflösung in der Größenordnung von 100 nm möglich. Diese technische Entwicklung könnte den Weg für ähnliche ultraschnelle Experimente ebnen, die eine Heterodyn-Detektion oder lange Signalerfassungszeiten an beschleunigerbasierten THz-Quellen erfordern.

Dedicated to my family.

Acknowledgements

It was a lucky day for me to be accepted as a Ph.D. student of Prof. Michael Gensch to work at TELBE – a cutting-edge high-field THz source user facility at HZDR, Dresden. I am not only amazed but also have learned a lot from Prof. Gensch's rigorous scholarship, strong leadership, and efficient project management. Therefore, I would like to sincerely thank Prof. Gensch for offering me the valuable opportunity to join the high-field THz-driven phenomena group.

I would like to express my most profound appreciation to my first-hand supervisor Dr. Sergey Kovalev, who has inexhaustible ideas and solid professional knowledge in THz optics. His extensive experience and hands-on coaching are my lifetime benefits.

In addition, I would like to extend my sincere thanks to Dr. Jan-Christoph Deinert. His generous assistance during the revision of this thesis gave me great help. I am also grateful to Dr. Bertram Green, Dr. Thales de Oliveira, Dr. Igor Ilyakov, Dr. Alexey Ponomaryov, and Dr. Nilesh Awari for a significant contribution to the experiments during the beamtime, both in day and night. I'll never forget your willingness to help me, to encourage me, and to question me.

I also wish to thank Prof. Thomas Cowan for offering me the special "Directors' Beamtime" at TELBE.

I owe my parents, DAI Yunxia and CHEN Tingyuan, a debt of gratitude for supporting me through more than seven years of studies across Eurasia – from China to Germany. I also want to thank my wife, Haosheng Wu, for standing by me through pain and pleasure.

Table of Contents

List of Figures

List of Tables

Acronym

ADC	Analog-to-digital Converter
AFM	Atomic Force Microscopy
ARPES	Angle-resolved Photoemission Spectroscopy
ALS	Advanced Light Source
ATM	Arrival Time Monitor
BAM	Bunch Arrival Time Monitor
BBO	Barium Borate
BP	Bandpass
BCM	Bunch Compression Monitor
BPM	Bunch Position Monitor
CEP	Carrier-Envelope Phase
CDR	Coherent Diffraction Radiation
CSR	Coherent Synchrotron Radiation
CMOS	Complementary Metal-Oxide-Semiconductor
CTR	Coherent Transition Radiation
DAQ	Data Acquisition
EO	Electro-optic
EOM	Electro-optic Modulator
ELBE	Electron Linac for beams with high Brilliance and low Emittance
FEL	Free-Electron Laser
FLASH	Free-Electron Laser in Hamburg
FTIR	Fourier-transform Infrared Spectroscopy
fs	femtosecond

GT	Glan-Taylor
HWP	Half Waveplate
HZDR	Helmholtz-Zentrum Dresden-Rossendorf
HGHG	High Gain Harmonic Generation
HHG	High Harmonic Generation
LTEM	Laser Terahertz Emission Microscopy
LCLS	Linac Coherent Light Source
MLO	Master Laser Oscillator
MZI	Mach-Zehnder Interferometer
nC	nanocoulomb
OR	Optical Rectification
OCXO	Oven-controlled Crystal Oscillator
ps	picosecond
pC	picocoulomb
PID	Proportional–integral–derivative
QWP	Quarter Waveplate
RF	Radiofrequency
SASE	Self-Amplified Spontaneous Emission
SD	Spectral Decoding
SHG	Second Harmonic Generation
SLAC	Stanford Linear Accelerator Center
SPPS	The Sub-picosecond Pulse Source
SNR	Signal-to-noise Ratio
SRF	Superconducting Radiofrequency
s-SNOM	Scattering-type Scanning Near-field Optical Microscopy
THG	Third Harmonic Generation
THz	terahertz
THz-TDS	THz Time-domain Spectroscopy
HRFZ-Si	High resistivity float zone silicon

VUV Vacuum Ultraviolet

XFEL X-ray Free-electron Laser

XUV Extreme Ultraviolet

1

Introduction

Terahertz (THz) radiation refers to electromagnetic radiation in the spectral range from 100 GHz to 30 THz which lies between the infrared and microwave ranges of the electromagnetic spectrum [1, 2]. THz-related research and applications have grown rapidly during the past decades in many areas with tremendous advancement in the development of THz generation and detection techniques. THz methodology has been significantly involved in the fields of astronomy [3], biology [4, 5], solid state physics [6, 7], chemistry [8] etc., as many low-energy degrees of freedom, e.g., rotational modes of molecules, elementary and collective modes in condensed matter lie within the THz region. In terms of real-world applications, THz-based technology is either used or shows great potential in a number of use cases, such as broadband and ultra-high bandwidth communication [9], security [10], and biomedicine [11, 12].

In recent years, the increased interest in observing THz-induced nonlinear phenomena in condensed matter physics and in resonant THz control of material properties boosted the demand for intense THz radiation sources [13, 6, 14, 7, 15]. Here, intense THz radiation refers to THz radiation with peak electric field in the range of 0.1-1 MV/cm in focus.

Common ways to generate strong THz pulses are based on nonlinear optical approaches such as optical rectification [16, 17], laser-driven gas plasma discharge [18], and photoconductive switches [19]. These methods can generate broadband, single-cycle THz radiation between 0.05 and 10 THz with maximal pulse energies of up to ∼500 µJ [20].

Although laser-based methods have advantages in terms of energy conversion efficiency, they are still significantly limited in providing THz radiation with a high repetition rate and high spectral brightness while maintaining the high peak field strength of the pulse. Typically, intense laser-based THz sources operate at repetition rates up to a few kilohertz. The low repetition rate limits their application in repetition-rate-hungry experiments such as time-domain THz s-SNOM or time-resolved THz Angle-resolved Photoemission Spectroscopy (ARPES). These techniques require the THz source to have a repetition rate on the order of hundred kilohertz up to megahertz while maintaining a strong enough field or pulse energy, respectively.

Accelerator-based THz sources can provide THz radiation with strong peak fields, high spectral brightness, and high repetition rates [21, 22]. This thesis focuses on diagnostic

development for superradiant THz sources and its application. These high-field sources can provide Carrier-Envelope Phase (CEP) stable high-energy pulses with broad frequency tunability, unprecedented repetition rates.

The THz generation mechanism in these types of sources can be briefly outlined as follows: First, electrons are accelerated to relativistic speeds while being compressed in time into sub-picosecond bunches, each with a charge on the order of picocoulomb (pC) to nanocoulomb (nC). These highly compressed electron clouds are then utilized to superradiantly emit electromagnetic radiation either by transversal acceleration or by passing through, or close to, media with varying dielectric properties. The first case can be realized by, e.g., bending magnets, the latter by metal foils with an aperture (termed Coherent Diffraction Radiation (CDR)) or without aperture (Coherent Transition Radiation (CTR)). Especially interesting are periodically varying magnetic structures, called undulators, emitting spectrally tunable multicycle narrow-band THz radiation. By tuning the electron bunch energy, the undulator magnetic field strength, and other parameters, the properties of the emitted THz radiation such as frequency, bandwidth, become controllable [23, 24].

These attributes make superradiant THz lightsources, whose THz radiation pulse energy can be beyond 100 µJ, extremely attractive as THz radiation sources for research on high-field THz-driven processes.

However, the attractive features provided by accelerator-based THz sources have in the past been counterbalanced by a number of drawbacks such as high complexity, high cost, and various instabilities. As a result, several intrinsic intricacies are restricting their application in ultrafast pump-probe experiments.

One of such complications is the synchronization between accelerator-based THz pulses and external laser pulses from table-top laser systems when both are combined in pump-probe experiments. The time delay between the THz pump and typically 800 nm probe pulses has to be precisely defined, and any jitter is detrimental to the temporal resolution of the pump-probe experiment. In the case of an ultrafast pump-probe experiment based on a femtosecond table-top THz source, a temporal resolution down to a few femtoseconds can be easily realized since pump and probe pulses can be intrinsically synchronized by means of beam splitting. In contrast, for accelerator-based THz sources, more effort on synchronization is needed to achieve a similar temporal resolution, since pump and probe pulses are generated by two independent sources.

Nowadays, there are several strategies to reach the required high precision synchronization at the femtosecond (fs)–level. One direct method, which is the most widely used, is to lock the electron accelerator, the external laser system, and various accelerator modules to an ultra-stable master clock [25] using a stabilized fiber link timing distribution system [26, 27]. However, this active-feedback method usually can only achieve synchronization in the level of a few tens of fs (RMS), which is significantly larger than the desired 10 fs synchronization level.

The second technique to achieve fs-level timing resolution is via the *post mortem* arrival time correction method. This method corrects the sequence of the experimental data based on the actual arrival time of each pulse as measured by an Arrival Time Monitor (ATM) system [28, 29, 30, 31]. Please note, the *post mortem* data correction technique requires coarse synchronization as a precondition. In this context, it can be considered as a data

processing-based improvement of conventional synchronization methods. A specific type of such an ATM scheme has been developed and benchmarked within this thesis, and the results are presented in Chapter 3.

Some ATM concepts can not only yield information about the arrival time but also record multi-dimension properties of individual pulses, such as temporal profile, frequency, and intensity. With this additional information, more details can be deduced from the pump-probe experiments, such as frequency-related or pulse intensity-related responses. Furthermore, detailed information on the emitted THz properties enables the ATM also to be used as a diagnostic tool, giving insights into electron bunch properties for accelerator research. Reviewing the implementation of this method, the pulse- and field-resolved *post mortem* analysis approach has already proven itself as a very efficient and robust method to achieve few tens of fs synchronization levels and for studying various electron bunch instabilities [28, 30, 32].

The third approach is through achieving intrinsic synchronization between accelerator-based sources and external laser systems by novel optical schemes such as seeding or slicing. A part of this thesis is about a newly developed slicing concept called THz-slicing. Details about this scheme are described in Chapter 4. In this scheme, a portion of a stretched, picosecond long laser pulse is sliced by an accelerator-generated THz pulse via interaction in an Electro-optic (EO) crystal. The sliced pulse is then intrinsically synchronized to the accelerator-based THz pulse and hence can be used as probe pulse for pump-probe experiments. This approach does not disturb the electron bunch, and it is applicable for high-charge beams at high repetition rates. The passive, all-optical nature of the THz-slicing technique circumvents any restrictions that may arise from the *post mortem* data correction approach: heterodyne detection or long integration times can be used without sacrificing temporal resolution. As a result, this approach has great potential to enable new types of ultrafast experiments on THz-driven ultrafast dynamics at accelerator-based THz sources.

To summarize, studies of a pulse- and field-resolved THz diagnostic and of a newly developed THz-slicing-based synchronization method are presented. First, a new sequential ATM is discussed, which utilizes two THz sources from TELBE, namely the CDR and the undulator source, to provide real-time information on the properties of individual pulses from multiple accelerator-based THz sources. It is experimentally shown that this approach can enable sub-femtosecond timing accuracy in synchronization between 4th generation lightsources and an external femtosecond laser system, which is extremely difficult to achieve with other techniques. Moreover, this technique enables studying the complex dynamics of single electron bunches. The results are described in Chapter 3. Secondly, the newly developed THz-slicing method is demonstrated and benchmarked at first using only laser-based sources. Here, it is shown that the jitter between the two light sources can be reduced to be below 10 fs even if these two sources have a few picosecond (ps) of initial timing jitter. The results are presented in Chapter 4.

Finally, the first implementation of the THz-slicing technique at an accelerator-based lightsource is demonstrated and benchmarked by successfully performing three different types of time-resolved experiments. The corresponding results are presented in Chapter 5.

1.1 Outline of the thesis

This thesis consists of six chapters. Chapter 1 is the introduction of the thesis. Chapter 2 reviews the state-of-the-art of high-field THz sources, THz-based diagnostics, and synchronization techniques, as well as a description of the superradiant THz user facility TELBE at Helmholtz-Zentrum Dresden-Rossendorf (HZDR). Chapter 3 describes the double-ATM-based pulse- and field-resolved THz diagnostic technique developed and tested within this thesis. Results about its application for increasing the temporal resolution of the pulse-resolved Data Acquisition (DAQ) system and obtaining additional information about electron bunches are presented. Chapter 4 describes the proof-of-principle experiment of the THz-slicing technique developed and tested in this thesis that enables the intrinsic synchronization between THz and the laser pulse. Chapter 5 presents three benchmark experiments in which the applicability of the THz-slicing scheme is demonstrated. Three benchmark experiments are performed: (i) linear THz Time-domain Spectroscopy (THz-TDS), (ii) nonlinear THz-TDS and (iii) the first successful time-domain s-SNOM experiment at a superradiant THz facility. The last summary and outlook chapter discusses the advantages and disadvantages of different synchronization methods, their optimal application scenarios, and application potential in other 4th generation lightsources. The entire work was performed at the TELBE facility at HZDR in Dresden.

2

Basics and Methods

2.1 Accelerator-based superradiant THz sources

Before the development of accelerator- and laser-based THz sources, the generation of radiation in the THz range was based primarily on the principle of thermal emission. Thermal light sources have proven themselves as very reliable and stable sources due to their simplicity. For example, in Fourier-transform Infrared Spectroscopy (FTIR), sources such as mercury lamps [33], globar [34], or others are typically still in use nowadays. Theses sources are typically operated provide a broadband spectrum and have an inherently low spectral density. In the last two decades, after tremendous progress in ultrashort pulsed laser development, a number of coherent, pulsed THz sources based on photoconductive antennas or nonlinear frequency conversion in various nonlinear media were developed. However, such laser-based THz sources also have several limitations, such as low conversion efficiency, typically in the sub-1% range, and comparably low damage threshold of the nonlinear media utilized for the THz generation process. Moreover, the typical THz emission of this type of laser-based THz sources is, similar to the thermal emission-based sources, spectrally broadband and narrow bandwidth can only be achieved at the cost of intensity.

These limitations result in a typically low spectral density and relatively low pulse energy of laser-generated THz radiation, especially at high repetition rates, i.e., beyond a few kHz, which severely limits their application for nonlinear THz spectroscopy experiment. For example, the highest optical-to-THz conversion efficiency was reported to be around 3.8 % by applying the titled-pulse-front method with a cryogenically cooled $LiNbO_3$ crystal at 1 kHz repetition rate [35]. For the conventional Optical Rectification (OR)-based method using ZnTe crystals, the conversion efficiency turns out to be only 3.5×10^{-5} [36]. To increase the output THz pulse energy in both of these cases, one needs to increase the input optical pulse energy. However, this typically results in damaging the nonlinear optical crystals because of the high peak power of the light pulses. To the best of our knowledge, the highest pulse energy is reported to be 436 µJ generated from the $LiNbO_3$ crystal at 10 Hz repetition rate with 0.77 % efficiency [20].

Another important class of intense THz sources is based on relativistic electron bunches. These sources attracted a lot of interest recently because of their potential to provide coherent THz radiation with much higher brilliance, high repetition rate, high spectral density, and continuous frequency tunability covering a frequency range from few hundreds of GHz to few tens of THz [37, 38]. There are different physical mechanisms based on which THz emission from relativistic electrons is achieved. In the following, a few mechanisms will be briefly introduced.

Synchrotron radiation

One primary method to obtain THz radiation from relativistic electron bunches is based on transversal acceleration (deflection) of the electrons propagating in magnetic fields due to Lorentz forces. This type of radiation is called synchrotron radiation [39]. The principle of the generation of synchrotron radiation is shown in Figure 2.1.

The electrons are accelerated to close to the speed of light c, propagating in a magnetic field that is orthogonal to the propagation direction of the electrons, so that the electrons experience the Lorentz force. Due to the nature of Lorentz force, it does no cause any change in the absolute value of the electrons' speed, but leads to transverse deflection (acceleration) of the electron bunch, which then generates electro-magnetic radiation according to Maxwell's equations. The radiation, known as synchrotron radiation, is emitted tangentially to the electron beam trajectory. The emitted power P_s produced per electron can be described by Larmor's formula [2],

$$P_s = \frac{e^2 a^2}{6\pi\varepsilon_0 c^3}\gamma^4, \tag{2.1}$$

where a is the acceleration, e is the elementary electron charge, ε_0 is the vacuum permittivity, and γ represents the ratio of the mass m of the electron to its rest mass m_0, as given by Equation 2.2:

$$\gamma = \frac{m}{m_0} = \frac{1}{\sqrt{1-(v/c)^2}}, \tag{2.2}$$

where v is the speed of the electron. As can be seen, the emitted power strongly depends on the electrons' speed and can only assume high values when v approaches the speed of light. Please note that the synchrotron radiation has linear polarization in the plane of the trajectory of the electron bunch, and that is perpendicular to its propagation direction and in-plane of the bending magnetic field.

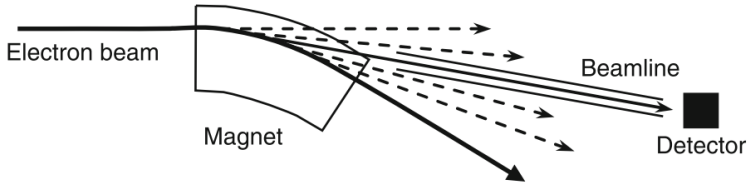

Figure 2.1: The relativistic electron beam emits synchrotron radiation when it is accelerated perpendicularly to its velocity by a bending magnet. Taken from [2]. Republished with permission of Springer-Verlag, permission conveyed through Copyright Clearance Center, Inc.

Transition and diffraction radiation

Two other mechanisms to obtain THz emission from relativistic electron bunches are based on the so-called transition radiation and diffraction radiation. Transition radiation is generated when an electron bunch passes through the interface between materials with different dielectric constants [40]. Diffraction radiation is generated when the electron bunch passes nearby a conducting material [41]. The commonality of these two types of radiations is, that the Coulomb field of the electron bunch experiences a change of the dielectric environment, which eventually leads to THz emission. Because of this similarity, only the theoretical description of the transition radiation will be presented in this thesis. Please note, forward and backward radiation is emitted after the electron bunch hits the target, as can be seen in Figure 2.2.

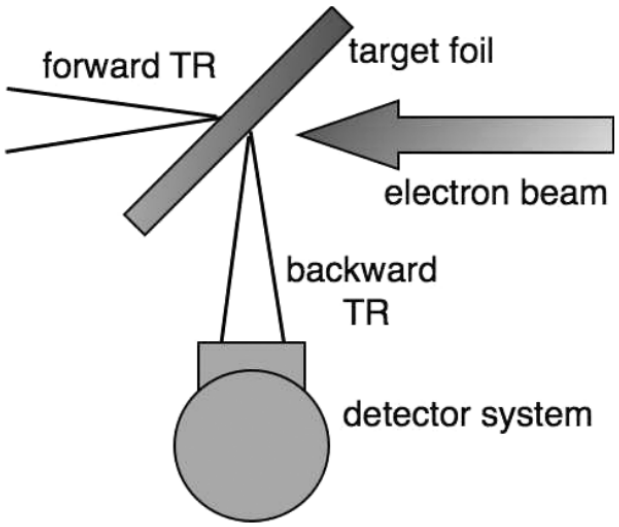

Figure 2.2: Schematic of transition radiation generation. A forward and backward transition radiation are emitted after the electron bunch hits the target foil. A detector is implemented to measure the backward transition radiation. Taken from [37].

In the case of a single electron bunch, the emitted spectral energy per unit frequency interval of transition radiation is given by the Ginzburg–Frank relation:

$$\frac{d^2W}{d\omega d\Omega} = \frac{e^2}{4\pi^3\epsilon_0 c}\frac{\beta^2\sin^2\theta}{\left(1-\beta^2\cos^2\theta\right)^2}, \tag{2.3}$$

where β is the ratio between the speed of electron and the speed of light, θ is the angle between electron trajectory and emitted radiation, and ω is the angular frequency of the emitted radiation [40, 37].

Figure 2.3 shows the target screen used for diffraction/transition radiation generation at the TELBE THz facility. The type of generated radiation can be switched from diffraction radiation to transition radiation by moving the aperture in the target screen slightly off-axis relative to the electron bunch trajectory. Please note, that transition and diffraction radiation are both radially polarized.

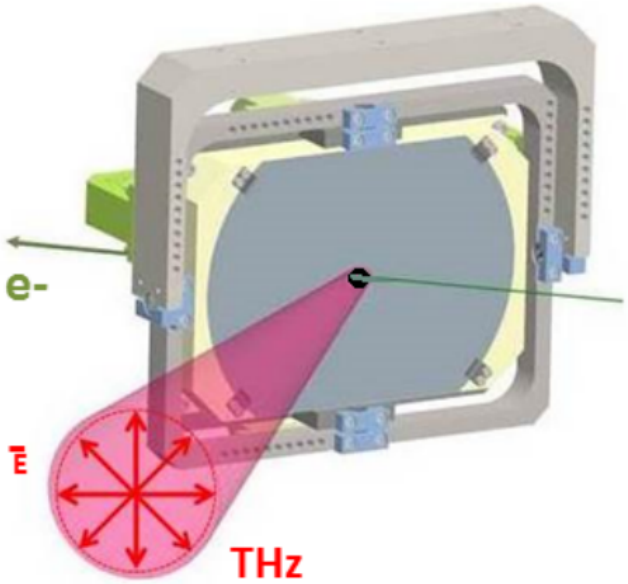

Figure 2.3: The diffraction/transition radiation radiator at the TELBE user facility. Diffraction radiation is generated when electron bunches pass through the aperture at the center of the metallic screen. Transition radiation is generated when electron bunches pass through the material, in the situation that the screen is slightly displaced from the axis of the electron bunch trajectory. Taken from [42].

Superradiant emission

Apart from the speed and charge of the electron bunch and type of THz generation process, there is another critical factor that determines the coherency and the power of the emitted THz radiation: the electron bunch length. As illustrated in Figure 2.4(a), an electron bunch of length L_b larger than the wavelength of the emitted radiation leads to the loss of coherence and potentially destructive interference of the radiation emitted by each of the electrons. Under this condition, often referred to as spontaneous regime, the overall radiated power is linearly proportional to the number of electrons within the bunch. Conversely, when the electron bunch is compressed to a length significantly smaller than the radiated wavelength λ, all electrons in the bunch radiate coherently, resulting in superradiant emission. In this superradiant regime, the radiated power is proportional to the square of the number of electrons in the bunch. The importance of this dependence becomes particularly clear when considering that nowadays, highly compressed bunches with charges on the order of hundreds of picocoulombs, corresponding to 10^8 electrons per bunch, can be routinely generated in modern linear accelerators. Such a large population of electrons per bunch results in superradiant emission which will be many orders of magnitude more intense than emission in the spontaneous regime.

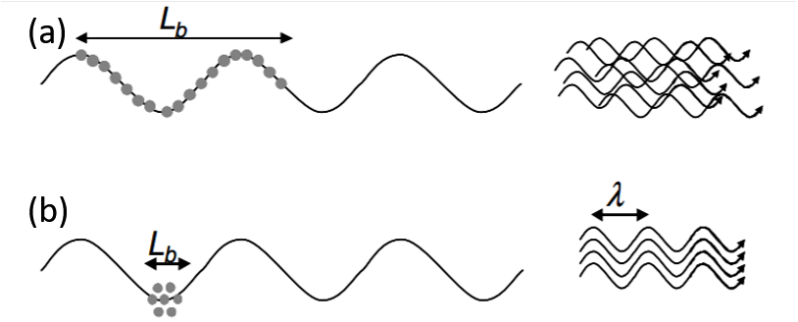

Figure 2.4: Schematic illustration of the superradiant emission principle. L_b and λ are the electron bunch length and the wavelength of the emitted radiation, respectively. (a) When the electron bunch length is longer than the wavelength of the emitted radiation, incoherent, spontaneous emission is induced. (b) When electron bunch length is shorter than the wavelength of the emitted radiation, superradiant emission becomes dominant. Taken from [43]. Reprinted with permission, Copyright 2008 IEEE.

In general, the total power P of the radiation emitted from a compressed electron bunch is given by [44]:

$$P = [(1 - f_\lambda)N + f_\lambda N^2]P_\mathrm{s} \tag{2.4}$$

where P_s is the power emitted by a single electron, N is the number of electrons in the electron bunch, and f_λ is the form factor that describes the degree of coherence. For electron bunches with an electron density distribution of Gaussian shape, the form factor is given by $f_\lambda = \exp\left[-(2\pi\sigma/\lambda)^2\right]$, where σ is the RMS length of the electron bunch. For longer emission wavelength, the form factor approaches unity, and thereby the superradiant emission (the second term in Equation 2.4), which is proportional to N^2, becomes dominant [2]. Compared to achieving superradiant radiation in the shorter wavelength, achieving superradiant radiation in the THz range is relatively easier in terms of the electron bunch length. For example, the superradiant radiation in 300 GHz becomes dominant when the electron bunch duration is shorter than 3.3 ps. Oppositely, to have dominant superradiant radiation at 800 nm, the electron bunch duration has to be shorter than 2.7 fs, which is much harder to realize.

In the following, the application of the principle of superradiance at various types of accelerators such as storage rings and linear accelerators, using different types of radiators, will be described. This includes facilities that are already operational or in the planning phase. A brief history of the development of accelerator-based superradiant THz sources is also included.

2.1.1 Storage rings in low-α operation mode

Because of its circular design, in storage rings, the electron bunch length is hard to be compressed and is typically in the range of a few tens of millimeters. For example, at BESSY II, the electron bunch length under single bunch operation is around 5 mm (∼70 ps bunch duration) [45]. At PETRA III, the electron bunch length is 13 mm, which corresponds to a bunch duration of 40 ps [46]. Such a long bunch duration is insufficient to allow superradiant THz emission, i.e., at wavelengths below 1 mm. To enable superradiant radiation at THz frequencies, additional measures are required to compress the bunch length further, e.g., by special tuning of the optics of the storage ring.

In 2002, an approach based on the so-called *low-α* mode of operation succeeded in generating steady-state superradiant THz radiation from 300 GHz to 1 THz, with a repetition rate of 1.25 MHz, at the storage ring BESSY II [45, 47].

The bunch length could be reduced to the picosecond regime through a reduced first-order momentum compaction factor enabled by compensating the dispersion partially with quadrupoles [37, 48].

In this case, according to [37], the bunch length σ is given by the following equation:

$$\sigma = |\alpha| R (\frac{\Delta p}{p})(\frac{f_{\mathrm{rev}}}{f_s}), \tag{2.5}$$

where α is the momentum compaction factor, $\Delta p/p$ is the momentum deviation, R is the average ring radius, f_{rev} is the revolution frequency of electron bunches and f_s is the α-dependent longitudinal synchrotron oscillation frequency [48]. Therefore, a short bunch length can be obtained by creating a setting with a relatively low value of α.

At BESSY II, operating in low-α mode, the electron bunch length can be compressed to 1 mm (corresponding to 3 ps) and thereby intense THz radiation can be generated in the sub 1 THz regime.

2.1.2 Superradiant THz sources at SASE FELs

Advances in linear accelerator technology have led to the development of the so-called 4th generation of synchrotron lightsources such as XUV-FELs and X-ray Free-Electron Laser (FEL) with the purpose to generate extremely intense pulsed UV and X-ray radiation via the so-called Self-Amplified Spontaneous Emission (SASE) process [49]. Early on, proposals were made to add THz radiators, in particular CTR/CDR sources or undulators, downstream of the short-wavelength sources [23]. One reason for theses was that the availability of the additional superradiant THz radiation broadens the spectral range of the radiation available for user experiments and thereby also broadens the scientific scope of the facility. Another reason is that the quality of the electron bunch after passing through the XUV or X-ray undulator, in most facilities, is still good enough to generate superradiant THz radiation of exceptional bandwidth and pulse energy since the electron bunch length required for the SASE process is much shorter than the one required for superradiant THz emission while the bunch charge is comparably high.

In other words, highly intense superradiant THz radiation can be generated with comparably moderate modifications of an existing facilities. In addition, the THz pulse is intrinsically synchronized with the X-ray pulse because both originate from the same electron bunch [50]. In terms of pump-probe experiments that use both wavelengths, this is another benefit of this scheme.

XUV and X-ray radiation are generated in undulator structures (the typical overall length is more than 100 m) via the SASE process: in the first section of the long undulator section, spontaneous incoherent synchrotron radiation is generated from the highly charged electron bunches. Acting as seed radiation, this radiation causes a self-modulation of the electron bunch density at the wavelength of the emitted radiation and results in microbunching of the electron bunch [49]. Along this process, energy will be transferred from the free electrons to

the emitted radiation. When the resulting properties of the electron microbunches satisfy the resonance condition, highly intense coherent radiation will be emitted. The resonance condition is given by [49]:

$$\lambda_R = \frac{\lambda_u}{2\gamma^2}\left(1 + \frac{K^2}{2}\right), \tag{2.6}$$

$$K = \frac{eB_0}{2\pi m_0 c}\lambda_u, \tag{2.7}$$

where, λ_R is the wavelength of the emitted radiation, λ_u is the undulator period, γ is the Lorentz factor (see Equation 2.2), K is a parameter referring to the magnetic field strength of the undulator, e is the elementary charge, B_0 is the maximal transverse magnetic field that the undulator can reach, m_0 is the rest mass of a single electron and c is the speed of light.

Since the wavelength of the emitted radiation can be tuned by adjusting the magnetic field strength of the undulator or the electron bunch energy, the output spectrum of the FEL is, in principle, widely and continuously tunable. For the case of electron bunch energies in the GeV level, the emitted radiation can be in the nm wavelength range. As the electron bunch length for the SASE FEL is typically much smaller than the requirement for superradiant THz emission, the spent electron bunch from the SASE FEL can easily meet the conditions for superradiant THz emission.

One seminal example of installing an additional superradiant THz source at an X-ray Free-electron Laser (XFEL), is the CTR source at the Linac Coherent Light Source (LCLS), which was the first operational hard X-ray FEL in the world. The CTR source at LCLS was placed 31 m downstream of the X-ray undulator. Electron bunches with a bunch charge of 150-350 pC and pulse durations of 50-100 fs (FWHM) were used to generate THz radiation via passing through a 2 µm thick beryllium disk. A maximum THz pulse energy of 200 µJ emitted into a broad THz bandwidth from 3 to 30 THz has been reported [51].

Another pioneering work was done at the Free-Electron Laser in Hamburg (FLASH), which is a single-pass SASE FEL driven by a 1 GeV superconducting linear accelerator. It can emit extremely bright ultra-short Vacuum Ultraviolet (VUV) pulses tunable in a wide spectral range of 6.9 - 47 nm, with an average XUV pulse energy from 10 to 50 µJ [52, 53].

At FLASH, superradiant THz radiation is produced by a planar electromagnetic undulator placed directly after the last XUV undulator with 9 periods, each with a length of 40 cm. As can be seen in Figure 2.5, the electron bunches first propagate through the undulator to generate pulses in the Extreme Ultraviolet (XUV) to soft X-ray frequency range via the SASE process. Afterwards, the spent electron bunches pass through the THz undulator and generate superradiant THz pulses. Finally, the electrons are dumped using a bending magnet. The THz radiation is redirected by a mirror, which has a 10 mm open aperture at the center, to the THz beamline. The highly collimated XUV pulses are transmitted through this aperture [24]. A dedicated 65 m long beamline transports the THz radiation towards the endstation to perform the pump-probe experiments with the soft X-ray and THz pulses.

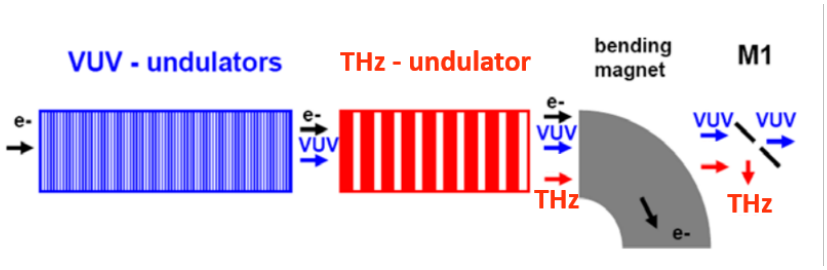

Figure 2.5: Schematic of the XUV and THz undulator at FLASH. Spent electron bunches from the XUV undulators pass through the THz undulator for THz radiation generation. Taken from [24]. Republished with permission of Elsevier; permission conveyed through Copyright Clearance Center, Inc.

The wavelength of the THz undulator emission covers the range from 1 to 300 THz, with pulse durations of 30 fs-10 ps and pulse energies up to 150 µJ. The longest achievable wavelength/lowest achievable THz frequency depends on the electron beam energy, as illustrated in Figure 2.6.

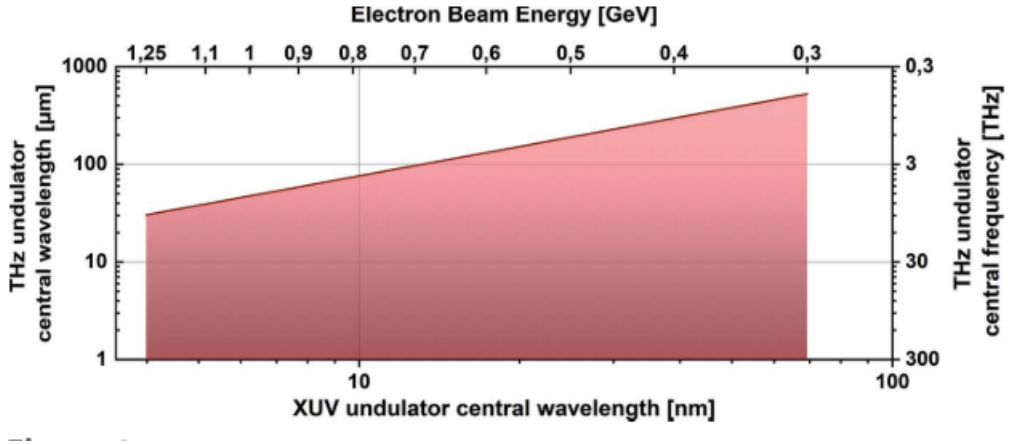

Figure 2.6: Relationship between the THz and XUV spectrum of FLASH. The shaded area denotes the tunable fundamental THz wavelength range (left vertical axis), as a function of the XUV wavelength (lower horizontal axis) and the electron bunch energy (upper horizontal axis). Taken from [54]. Republished with persimmon of the CC-BY License.

Plans about installing THz undulators into the last generation XFELs are discussed at the European XFEL [55], and at Linac Coherent Light Source-II (LCLS-II) [56], to generate narrow-band THz radiation. With the combination of these advanced sources of THz and X-ray, many new scientific opportunities will become available.

Compared to the XUV FEL FLASH, the electron beam energy within 8.5 to 17.5 GeV at the European XFEL is much higher. In order to generate undulator radiation in the THz regime, much higher magnetic fields and much longer undulator period lengths are required. Therefore, conventional undulator technology would need to be replaced by superconducting undulator technology because of the much higher magnetic field it can provide. [55]. A compact 8-period undulator, applying NbTi-based superconducting undulator technology, with a period length of 1 m, and on-axis peak field of 7.3 T has been proposed to generate narrow-band, frequency-tunable THz radiation within the frequency range of 3 to 100 THz and with a fundamental pulse energy up to 2 m J at 3 THz at a megahertz repetition rate [57, 55].

At LCLS II, where the beam energy is around 4 GeV, it is envisioned to incorporate a 10-period normal conducting THz undulator downstream of the soft X-ray undulators, as shown in Figure 2.7. This THz undulator is supposed to emit THz pulses with frequencies in the range of 3-20 THz with pulse energies of up to 100 µJ at 100 kHz repetition rate [58].

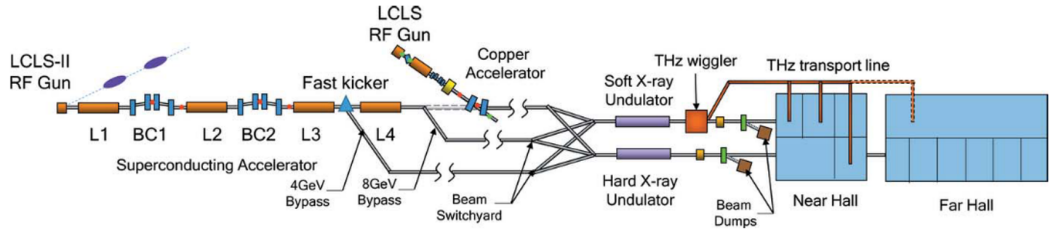

Figure 2.7: Schematic of the planned THz sources at LCLS II. The THz wiggler is supposed to be installed downstream of the soft X-ray undulators. Taken from [58]. Republished with persimmon of the CC-BY License.

2.1.3 Dedicated linac-based superradiant THz sources

The high electron bunch kinetic energy (∼GeV) designed specifically for X-ray pulse generation in the XFELs is not always favorable for the generation of superradiant THz radiation via THz undulators. The high electron bunch energy requires much stronger magnetic fields in the undulator to emit radiation in the THz frequency range. To reach such high magnetic fields, comparably complex undulator technologies need to be applied to keep the length of the undulator periods within a reasonable range. This particularly the case for THz frequencies below 3 THz [55].

Further, the default parasitic operation of the THz sources at XUV and XFELs restricts the parameter space of the electron bunch properties for THz generation, since the accelerator settings will normally be optimized for the generation of the XUV and X-ray pulses.

Following the particular demand from the scientific community for high-power THz sources, first *dedicated* linac-based superradiant THz sources have been designed and built. In this new class of linac-based superradiant THz sources, highly compressed and highly charged relativistic electron bunches of lower energy in the few 10 to few 100 MeV range in are used to generate superradiant THz radiation via a single pass through one or more radiators. In contrast to parasitic sources at SASE FELs, these dedicated sources offer much higher degree of control over the electron beam properties and hence provide higher flexibility with respect to the THz pulse parameters.

A seminal work on high-intensity THz radiation generation from ultrashort electron bunches was carried out at the energy-recovered linac (ERL) at the Jefferson Laboratory in 2002, where comparably low-energy electron bunches (∼ 40 MeV) could be compressed to a duration of around 500 fs for the generation of superradiant THz radiation via Coherent Synchrotron Radiation (CSR) from a bending magnet [59]. As the linac was driven by superconducting radiofrequency cavities, it could provide broadband THz pulses (300-600 GHz) at a high repetition rate up to 75 MHz.

In 2003, another superradiant THz source built at the linac at the Brookhaven National Laboratory came into operation. The linac produced electron bunches with ∼500 pC charge and ∼1 ps bunch length at 2.5 Hz repetition rate. Via CTR, broadband THz pulses with

frequencies up to 1 THz and pulse energy up to 100 µJ could be generated at a repetition rate of a few Hz [60].

In China, a compact superconducting Radiofrequency (RF) accelerator has been built at Peking University to generate superradiant THz radiation from a 10-period planar undulator. The facility can generate THz pulses with pulse energies up to 0.29 nJ at a repetition rate of 16.25 MHz, with a tunable frequency range between 0.24-0.42 THz from electron bunches with the energies between 2.4-3.1 MeV [61].

In Dresden, a unique linac-based dedicated superradiant THz user facility named TELBE has been built at the Helmholtz-Zentrum Dresden-Rossendorf (HZDR). This facility is based on a superconducting linac called ELBE, which can provide electron bunches with a kinetic energy up to 40 MeV operating in the quasi-cw regime with repetition rates up to 13 MHz. At TELBE, two types of THz radiators are installed, namely one CDR screen that can generate broadband THz pulses, and one undulator that can produce tunable narrowband THz pulses [62, 32]. Details about the TELBE user facility, at which the work in this thesis was performed, will be introduced in the next section.

2.2 THz user facility TELBE

2.2.1 ELBE superconducting linear accelerator

The Electron Linac for beams with high Brilliance and low Emittance (ELBE) is an linear electron accelerator built at HZDR for the generation of various types of secondary radiation (see Figure 2.8). There are two types of injectors that can be used for THz generation. One is the thermionic injector that can produce electron bunches with bunch charge up to 100 pC at a repetition rate of up to 13 MHz. Another one is the Superconducting Radiofrequency (SRF) injector, the ultimate goal with it is to produce much higher bunch charges up to 1 nC at up to 500 kHz repetition rate [62]. Currently, superradiant THz emission generated from electron bunch with bunch charges of 200–300 pC at typical repetition rates of 100 kHz has been achieved [63].

At present, the electron beam generated at ELBE drives two infrared free-electron lasers (FELBE), pulsed sources for bremsstrahlung (γELBE), neutrons (nELBE), positrons (pELBE), as well as the superradiant THz facility TELBE. The layout of ELBE and the endstations are shown in Figure 2.8. Currently, for the operation of TELBE, ELBE is running at repetition rates between 25 kHz and 250 kHz with a bunch charge up to 250 pC using the SRF photocathode injector. Optionally, the thermionic injector can be used as electron source which can provide highest repetition rates at lower bunch charge up to 13 MHz. In addition to enabling higher bunch charges and hence higher THz pulse energies, the SRF photocathode injector also shows better stability with respect to pulse energy and timing jitter of the emitted THz pulses.

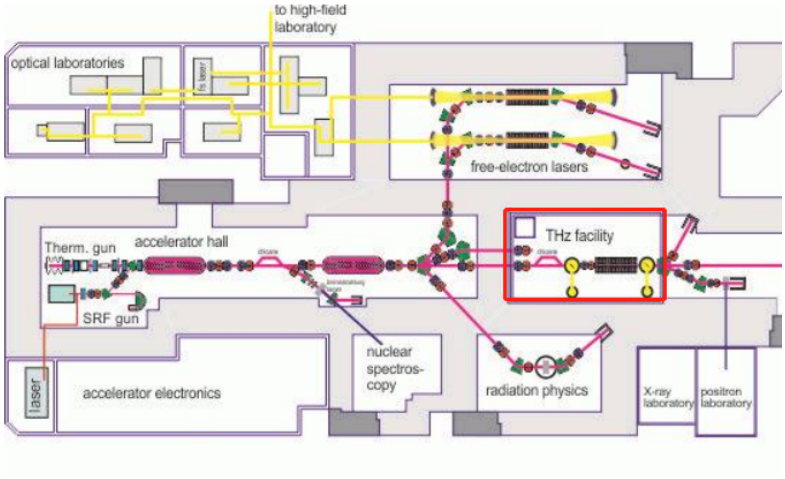

Figure 2.8: Layout of ELBE accelerator and all end-stations. The red rectangle shows the location of TELBE inside the ELBE facility. Modified from [64].

2.2.2 Synchronization and diagnostics at TELBE

High-field THz pulses with field strengths up to a few MV/cm are expected to enable novel THz-driven nonlinear dynamics in matter such as nonlinear THz photonics, spintronics and coherent manipulation of the electronic states and lattice degrees of freedom of matter. In order to perform time-resolved pump-probe experiments of the above-listed types of dynamic processes, a synchronization system capable of synchronizing the THz radiation from the TELBE to a femtosecond laser system is required. However, despite all efforts to improve conventional synchronization techniques, a timing jitter on the order of a few hundred femtoseconds between the accelerator-based light pulses and external laser pulses is a typical limit for such large-scale facilities. This timing jitter has to be further minimized to increase the temporal resolution of the time-resolved pump-probe experiments to the a few tens of femtoseconds regime or even below.

More generally, the fluctuations of the electron bunch properties (such as bunch length, bunch energy, bunch shape and trajectory) can lead to fluctuations of the THz pulse in terms of pulse energy, pulse arrival time, and pulse spectrum. These fluctuations originate from the instability of the interplay of the large number of constituent parts of the accelerator itself. To increase the stability of the THz sources at TELBE, a number of diagnostic instruments have been implemented to study the origin of these fluctuations.

In this section, a brief introduction about the timing signal distribution system of ELBE and the synchronization system of TELBE will be presented. The operation principle of the implemented beam diagnostic instruments: Bunch Arrival Time Monitor (BAM), Bunch Position Monitor (BPM) and Bunch Compression Monitor (BCM) will also be shortly described in this section.

2.2.2.1 Synchronization system of TELBE

Similar to other facilities, at ELBE, a system delivering a timing signal to synchronize various components of the facility has been installed [64] as shown in Figure 2.9. An Oven-controlled Crystal Oscillator (OCXO) oscillating at 13 MHz provides a highly stable RF

reference signal. A Proportional–integral–derivative (PID) controller is used to lock the Master Laser Oscillator (MLO), a commercial laser system from Onefive GmbH, to the RF reference signal. The master optical oscillator operates at repetition rate of 78 MHz (the 6^{th} harmonic of 13 MHz), at a wavelength of 1560 nm and with ultra-low timing jitter smaller than 6 fs. After a fiber splitter and an amplifier, the timing signal is further delivered to the injection laser of the electron gun and other endstations, including TELBE [64, 65].

In the TELBE lab, a commercial fs Ti:sapphire laser system from Coherent Inc. serves as probe in pump-probe experiments. The laser system consists of a laser oscillator (Model: Vitara) and a Ti:Sapphire amplifier (Model: RegA 9000). The system can generate laser pulses with pulse energies up to 6 µJ at a central frequency of 800 nm, with 100 fs (FWHM) pulse duration and 10 nm bandwidth. In 2020, the laser system was upgraded to be able to provide pulses with 35 fs (FWHM) duration. Please note, in this thesis, only the THz-slicing benchmark experiments shown in Chapter 5 utilized the 35 fs duration laser pulse. Other experiments are performed with the 100 fs laser pulse. The THz-laser synchronization is realized by locking the laser oscillator to the MLO through the commercial device Synchrolock AP produced by Coherent Inc. [66], as can be seen in Figure 2.9.

Depending on the experimental requirements, the Synchrolock [66] can provide coarse THz-laser synchronization with an accuracy in the range from 500 fs to 4 ps (RMS) when RF synchronization is in use. Using a length-stabilized fiber link, synchronization level below 140 fs (RMS) can be reached [67]. To achieve a temporal resolution on the order of few tens of femtoseconds, further efforts utilizing arrival time correction techniques have been developed and implemented [32]. Details about the pulse-resolved DAQ system using this technique will be introduced in Subsection 2.2.4.

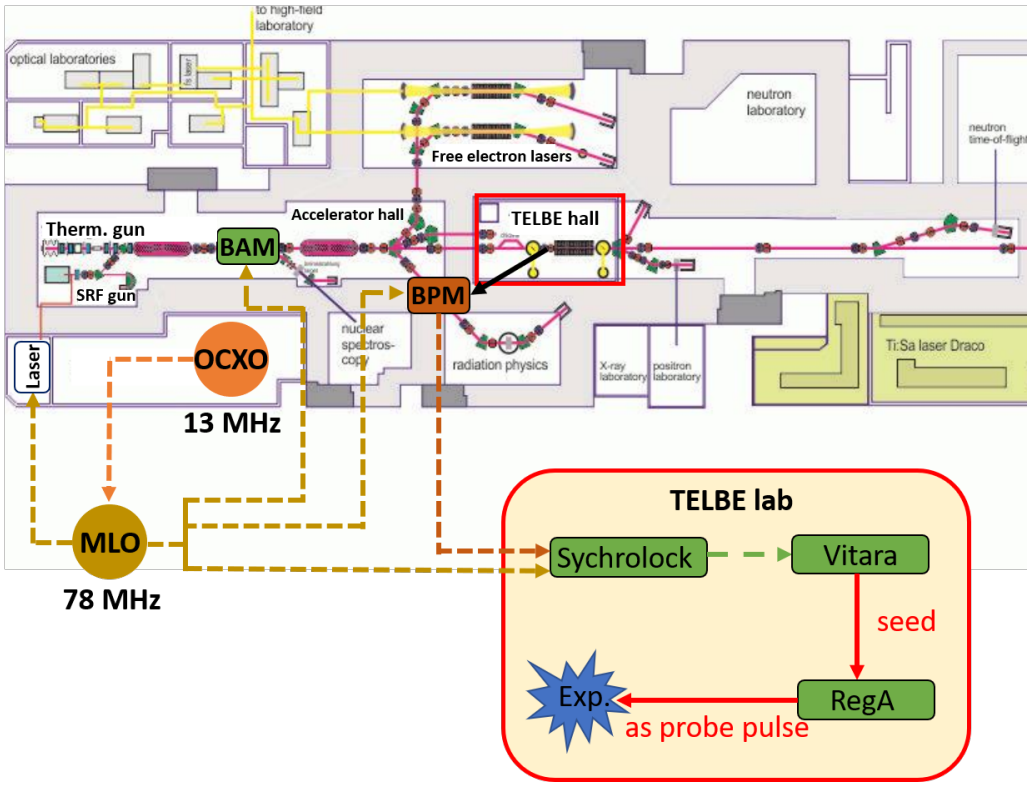

Figure 2.9: The synchronization layout of the laser systems inside the TELBE lab is shown in the red rectangle. The signal from the BPM placed in the TELBE hall is used as arrival time signal and sent to the Synchrolock in the TELBE lab for synchronization. The origin of the black arrow pointing to the BPM indicates its actual position in the TELBE hall (see Figure 2.13). Modified from [64].

2.2.2.2 Conventional electron bunch diagnostics at ELBE

Bunch arrival time monitor (BAM)

At ELBE, there are several types of electron bunch diagnostic equipment such as BAM, BPM, and BCM. Here, we very briefly introduce the operation principle of these diagnostics units. For more detailed information, please see Ref. [64]. As an example shown in Figure 2.13, a BAM is placed right in front of the entrance of the THz undulator. A BAM consists of three main parts, the RF pick up, the electro-optic modulator, and the Analog-to-digital Converter (ADC) readout.

As illustrated in Figure 2.10, the RF pickup is placed close to the beamline, so that passing electron bunches generate an RF signal induced by their electric field. Then, the RF pickup signal is sent to the Electro-optic Modulator (EOM), whose core element is a Mach-Zehnder Interferometer (MZI) that compares the optical length of two arms. The principle of the MZI can be briefly explained as follows: The reference signal is split into two parts to transmit independently through two arms of the MZI. After applying the RF pickup signal to one arm, the refractive index of one arm is modulated and hence leads to a phase shift compared to the reference signal. After interference between the reference and the modulated signal, the bunch arrival time information is imprinted into the intensity modulation of the reference signal at the output of the MZI [64].

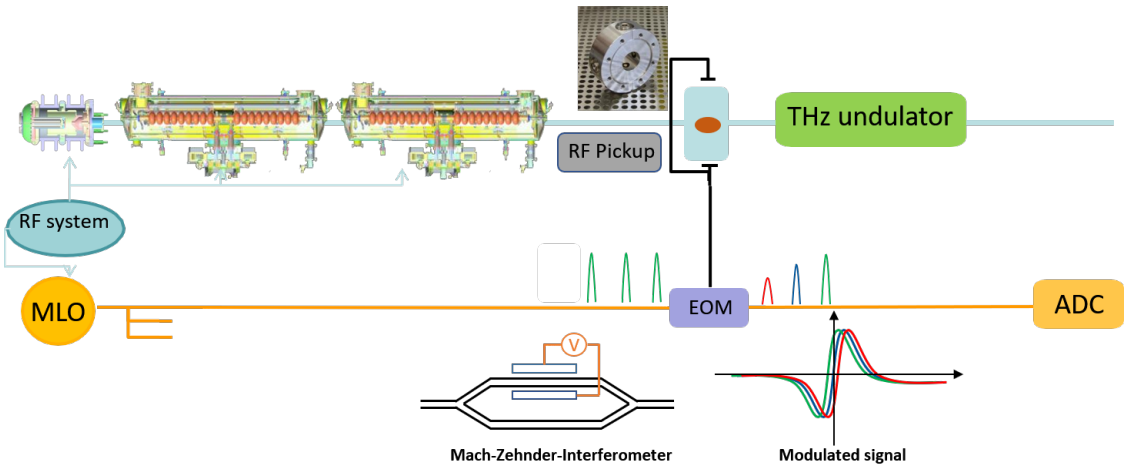

Figure 2.10: Operation principle of BAM. The MZI in EOM converts the arrival time difference between the RF pickup signal and the reference signal into intensity modulation of the reference signal that can be read out by an ADC. Taken from [64].

Bunch position monitor (BPM)

Another diagnostic instrument is the BPM (see Figure 2.11). One BPM is implemented right upstream of the THz undulator (see Figure 2.13). Determining the exact bunch position is highly important, since it has a strong influence on the emittance of the undulator [68]. The BPMs installed at ELBE are of the stripline BPM type. This BPM type utilizes the image current generated on the inner surface of a metallic beamtube when an electron bunch propagates through it at relativistic speed [69]. The longitudinal distribution of the image current on the inner wall surface changes with the beam structure. The image current distribution can be expressed by Equation 2.8,

$$I_{\mathrm{img}}(r,\alpha,\varphi) = \frac{I_0}{2\pi R}\frac{R^2-r^2}{R^2+r^2-2Rr\cos(\varphi-\alpha)}, \tag{2.8}$$

where α and r are the polar coordinates of the electron beam, φ is the polar coordinate of the probe point, I_0 is the average current of the beam, and R is the inner radius of the transmission tube [70]. The schematic diagram of the BPM and the coordinate system can be seen in Figure 2.11.

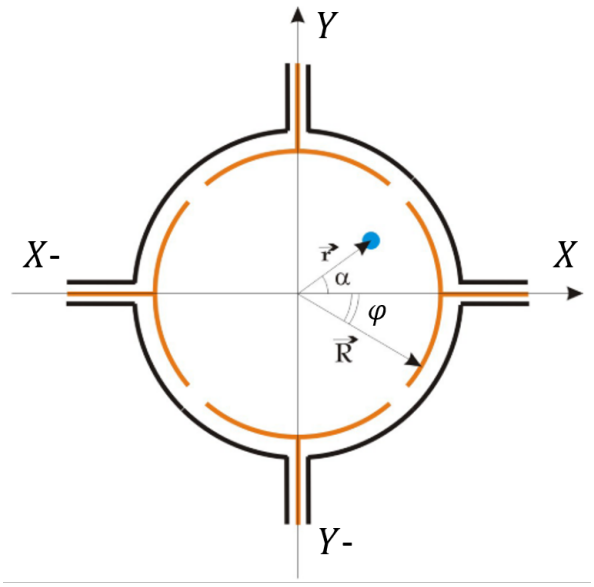

Figure 2.11: Coordinate system of the stripline BPM. The blue circle denotes the electron beam position. X and Y represent the horizontal and vertical electrodes, respectively. Modified from from [68].

Omitting the mathematical derivation, the beam position in a rectangular coordinate system can be written as the function of the integral currents measured on the X, $X-$, Y and $Y-$ electrodes [68], as shown by Equation 2.9 and 2.10

$$x = \frac{R}{2}\frac{\theta/2}{\sin(\theta/2)}\frac{I_X - I_{X-}}{I_X + I_{X-}}, \tag{2.9}$$

$$y = \frac{R}{2}\frac{\theta/2}{\sin(\theta/2)}\frac{I_Y - I_{Y-}}{I_Y + I_{Y-}}, \tag{2.10}$$

Bunch compression monitor (BCM)

Another electron beam diagnostic instrument is the BCM. According to the principle of superradiance mentioned previously, the spectral distribution of the emitted radiation strongly depends on the electron bunch longitudinal shape, as described by Equation 2.4. Therefore, through measuring the frequency content of the superradiant emission, one can estimate the electron bunch duration. Also, with constant bunch charge, the total emitted power is a function of the electron bunch length, and thus also can be used for bunch length estimation.

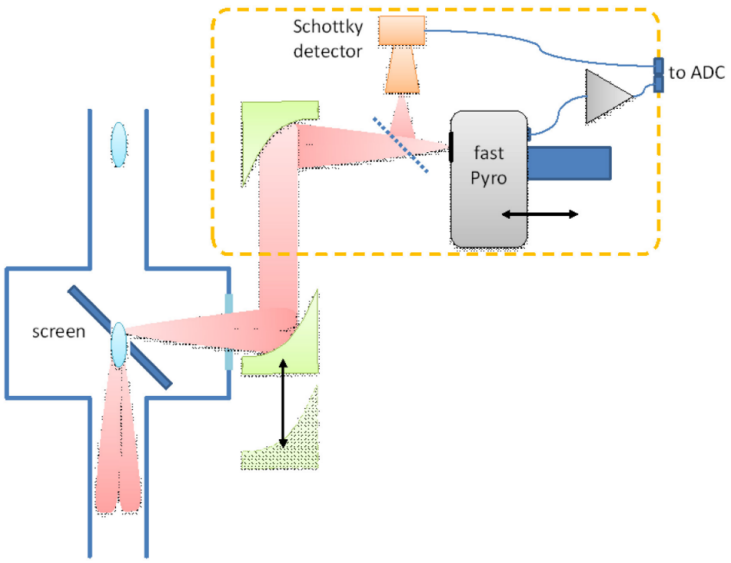

Figure 2.12: Structure of the BCM installed in front of the THz undulator of the TELBE facility. THz backward CDR radiation is sent to the BCM with two movable parabolic mirrors. The focusing beam is further split into to arms, one goes to a Schottky detector, and the other one goes to one pyroelectric detector. Modified from [64].

At TELBE, a BCM is built just in front of the THz undulator in the accelerator hall with one pyroelectric detector and one Schottky diode detector, aiming at detecting the emitted THz pulses energy at repetition rate up to a few hundreds of kilohertz. The layout of the BCM can be seen in Figure 2.12.

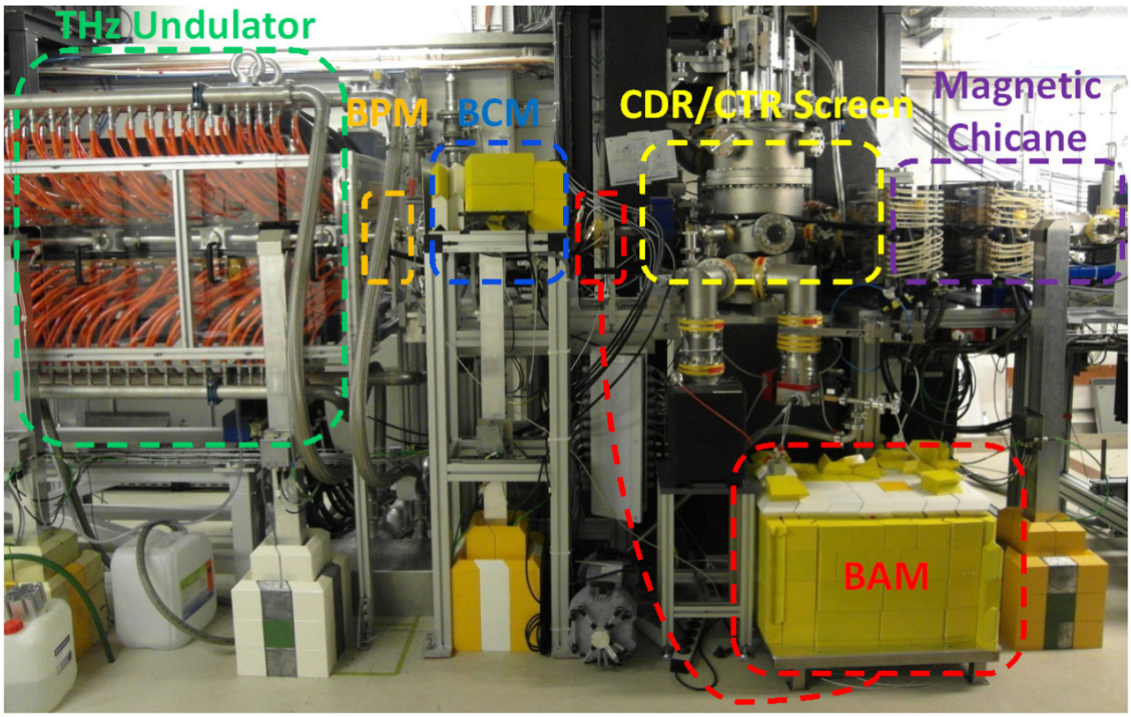

Figure 2.13: Photograph of the layout of the BCM, BPM and BAM in the TELBE source hall. The BAM is placed close to the CDR screen. The BPM and BCM are placed between the THz undulator and the CDR source. Taken from [64].

2.2.3 Superradiant THz sources at TELBE

At TELBE, there are two THz sources operational for user experiments. The first one is a CDR source. The principle of CDR has been introduced in Section 2.1. Such a source can be realized as a metal disc with a circular hole at the center, allowing electron bunches pass through, can be used as a CDR source. In the ELBE beamline, the screen is made of an aluminum-coated silicon wafer with a 4 mm central aperture. The CDR source can generate broadband THz pulses with frequencies ranging from 0.1 to 1.2 THz [42].

The other superradiant THz source is an electromagnetic undulator that consists of eight anti-parallel magnetic dipoles. As Figure 2.14 shows, the straight trajectory of the electron bunch is changed to a sinusoidal trajectory when the electron bunch experiences the Lorentz force during its pass through the undulator. Hence, the superposed synchrotron radiation emitted at each turn of the electron bunch results in the emission of narrowband multi-cycle THz pulses at the end of the undulator [71]. The undulator source at TELBE is designed for generating narrowband THz pulses in the frequency range of 0.1-3 THz [42]. The fundamental frequency of the undulator can be tuned by changing the magnetic field strength of the electromagnet or the energy of the electron bunch, as the Equations 2.11 and 2.12 describe. The resonance condition is given by [49]:

$$\lambda_R = \frac{\lambda_u}{2\gamma^2}\left(1 + \frac{K^2}{2}\right), \tag{2.11}$$

$$K = \frac{eB_0}{2\pi m_0 c}\lambda_u, \tag{2.12}$$

where, λ_R is the wavelength of the emitted radiation, λ_u is the undulator period, γ is the Lorentz factor (see Equation 2.2), K is a parameter referring to the magnetic field strength of the undulator, e is the elementary charge, B_0 is the maximal transverse magnetic field that the undulator can reach, m_0 is the mass of single electron and c is the speed of light. Please note, because of the radiation generation mechanism of the undulator, the emitted THz radiation also contains the higher odd numbered harmonics of the fundamental frequency [41].

In the ELBE beamline, the CDR screen is placed upstream of the undulator, as can be seen in Figure 2.14. After passing through the CDR screen, the electron bunches propagate towards the THz undulator. For convenience, in this thesis, the THz pulses generated by CDR and undulator sources are called CDR pulse and undulator pulse, respectively.

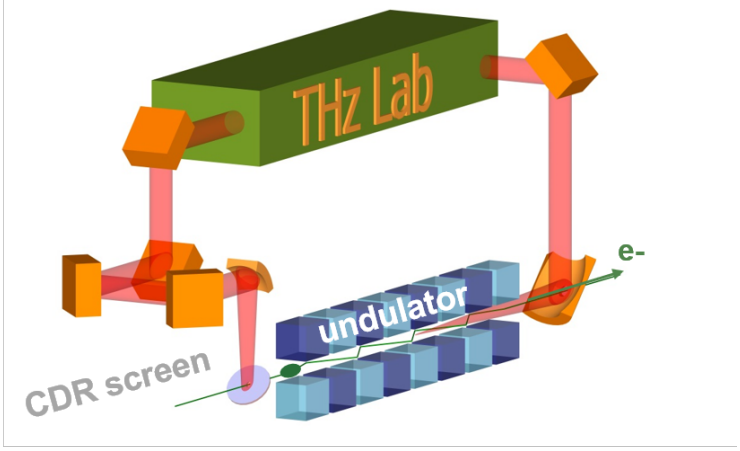

Figure 2.14: Layout indicating the relative position of electron bunch path, CDR screen, undulator, and the THz beamline guiding the CDR and undulator radiation to the above THz lab (TELBE). Taken from [42].

It should be noted, that the CDR and undulator pulses are generated by the same electron bunch, therefore, both pulses are intrinsically synchronized [62, 32]. This feature is very important and has various implications. Most importantly, this feature allows precise timing of the pulses from one of the sources by timing pulses from the other source, which is the fundamental idea behind the pulse-resolved data acquisition system that is described in Section 2.2.4.

Figure 2.15(a) shows the single-cycle waveform of the CDR pulse measured by means of EO sampling and Figure 2.15(b) shows the temporal shape of the undulator pulse when the fundamental frequency is tuned to 0.7 THz.

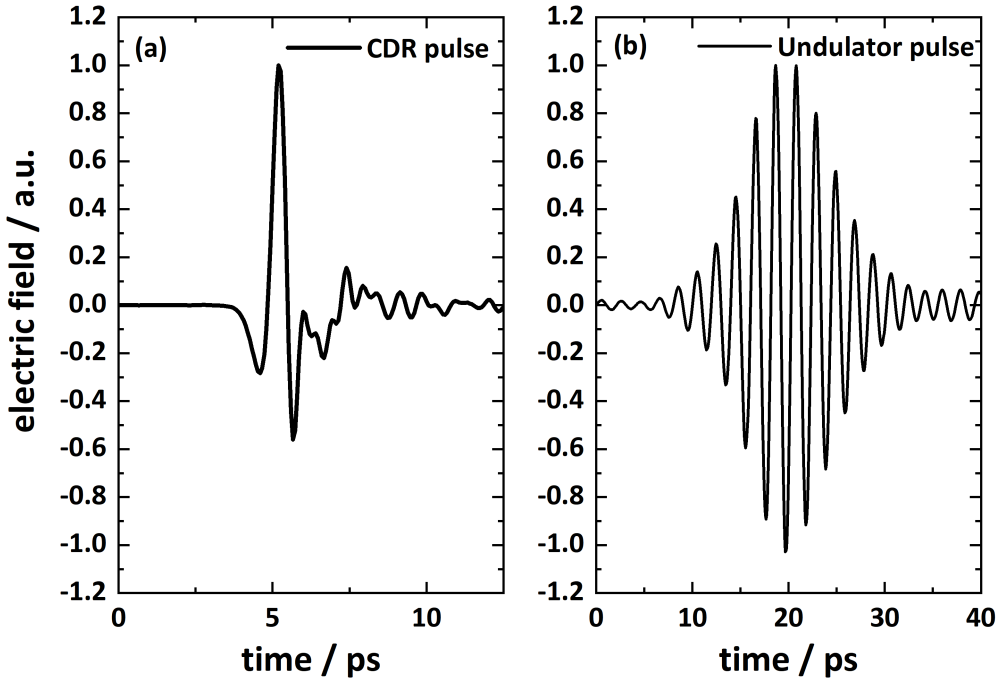

Figure 2.15: Pulse waveform of the CDR and the undulator pulse measured by means of EO sampling. (a) CDR pulse waveform. (b) Undulator pulse waveform. Please note, the fundamental frequency of undulator radiation was tuned to 0.7 THz while a 0.7 THz bandpass filter was inserted into the undulator pulse beamline. The presented data are measured with the pulse-resolved DAQ system (see subsection 2.2.4), which could compensate the timing jitter.

2.2.4 Pulse-resolved data acquisition system at TELBE

2.2.4.1 Structure of the pulse-resolved data acquisition system at TELBE

As mentioned before, the current synchronization system at TELBE allows the synchronization between the THz radiation generated by the undulator and the table-top laser system at a level of few hundreds of femtoseconds. However, this is not enough for performing pump-probe experiments with sub-cycle temporal resolution, when the central frequency of the pump THz pulse is higher than 300 GHz. An alternative route towards increasing the precision of the synchronization, or more specifically, the temporal resolution of the pump-probe experiment is to precisely measure the relative arrival time between the THz sources and the laser for every single pulse. The timing jitter of the experiment can thereby be corrected according to the measured *real* arrival time. This kind of method, known as *post mortem* data correction, is one way to increase the temporal resolution beyond the jitter limit. This method has been implemented at a number of different accelerator facilities [72, 28].

At TELBE, a pulse-resolved DAQ system was implemented to correct the timing of THz pump-probe experiment (the THz pulse is used as pump pulse and the laser pulse is used as probe pulse) on femtosecond timescales [32].

The system contains two main parts that are referred to as *modules*: The Arrival Time Monitor (ATM) module and the ultrafast experiment module, as seen in Figure 2.16. The function of the ATM is to measure the relative arrival time between the THz pulse and the external laser pulse. In the ultrafast experiment module, a pulse-resolved signal from a sample will be recorded simultaneously with the ATM operation.

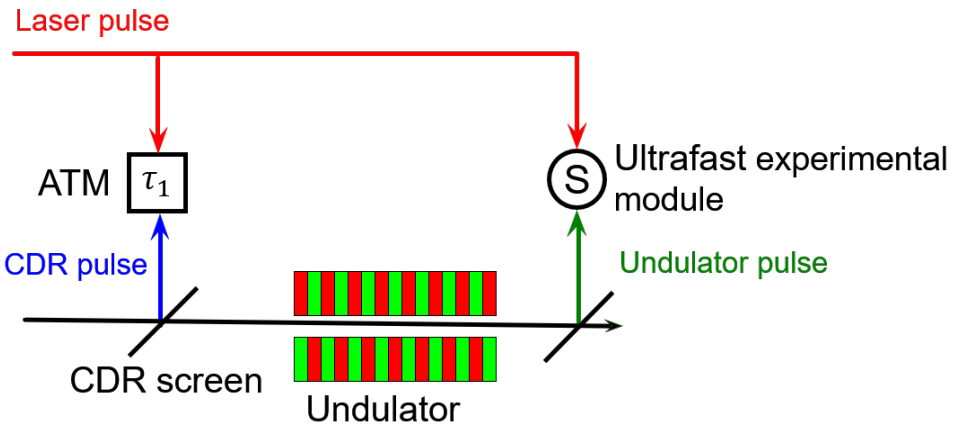

Figure 2.16: Block diagram showing the pulse-resolved DAQ system. The fs probe laser beam is split into two paths. One path is guided into the ATM for the arrival time measurement. This measurement yields τ_1 as the relative arrival time of THz and laser pulse. The other path is guided to the actual pump-probe experiment, where the undulator pulse is used as pump. In general, the ATM gives the arrival time information and the ultrafast experimental module gives the corresponding experimental signal.

The working principle of the ATM is based on the so-called Spectral Decoding (SD) approach, which will be introduced in detail in the Section 2.3. In general, the ATM module utilizes the spectral decoding approach to imprint the electric field of the THz pulse onto the temporally chirped spectrum of the laser pulse. Thereby, temporal information is converted into spectral information. By reading out and recording the spectrum of every single laser

pulse in the ATM with a grating spectrometer, the relative arrival time between the laser and the THz pulse can be deduced. A example of two typical SD traces measured by the CDR ATM (the ATM measures relative arrival time between each CDR and the laser pulse) is shown in Figure 2.17. From the primary peak position $P_{1,2}$ of the SD trace, the relative arrival time can be read out directly.

The actual experiments on THz-driven dynamics in matter are carried out by means of pump-probe experiments. Regardless of the exact type of the experiment, the probe laser pulse, after interaction with the sample, carries the information of the experiment (measured in the ultrafast experimental module, see Figure 2.16), which is then recorded by the ADC of the DAQ system. The arrival time of each pulse is corrected after the measurement by the timing values determined by the ATM.

Besides arrival time correction, as the integral part of the *post mortem* data correction technique, the THz intensity fluctuation can be recorded for each pulse by the THz intensity monitor for *post mortem* THz intensity correction or further accelerator diagnostics. For this purpose, a pyroelectric detector is installed in the TELBE lab to record the intensity of every single THz undulator pulse.

2.2.4.2 Data analysis procedure

In order to achieve high temporal resolution and sensitivity in the experiment, the as-measured data needs to be corrected with the relative arrival time measured by the ATM and optionally the THz pulse intensity measured by the pyroelectric detector.

For each THz pulse, a dataset consisting of several parameters (τ_1, I, T, S) is measured, where τ_1 is the relative arrival time between the THz pulse and the probe laser pulse, I is the THz pulse intensity, T is the delay line position and S is the signal measured in the ultrafast experiment module. Please note, during the ultrafast pump-probe experiment, the THz-induced dynamics are measured in the time-domain by changing the relative delay T between the pump and the probe pulse by moving a mechanical delay stage in the laser beampath.

The whole *post mortem* data treatment process requires three main steps, (i) the arrival time assignment, (ii) the arrival time correction and (iii) the data binning which are described in the following.

Arrival time assignment

The arrival time information is deduced from the SD trace measured by the ATM. The raw data taken by the spectrometer of the ATM is the THz-modulated spectrum of the chirped pulse where wavelength corresponds to the arrival time. For details about the spectral decoding technique used by the ATM, please refer to Section 2.3.

Before actually deducing the arrival time form the spectrum, it is very important to calibrate the ATM to obtain the *pixel-wavelength-arrival time* mapping relation that can be used for the arrival time assignment. The pixel to wavelength mapping of the detector array is a fixed parameter of the spectrometer in the ATM, which can be characterized by a calibration lamp. The wavelength to arrival time mapping is then determined by the chirp rate of the chirped pulse, which can be measured by observing the spectral shift by adding known

time delays. For the CDR ATM, the *pixel-wavelength-arrival time* mapping turns out to be 11.9 fs/pixel. This parameter is the most important parameter in the *post mortem* sorting process.

As can be seen in Figure 2.17, the SD trace of the CDR pulse (the blue trace in Figure 2.17) has one primary peak (P_1) owing to the quasi single-cycle waveform of the CDR pulse. The peak position of the primary peak can be used to deduce the actual relative arrival time τ after applying the *pixel-wavelength-arrival time* mapping. Therefore, from the SD trace of each pulse, the CDR-laser pulse relative arrival time can be deduced.

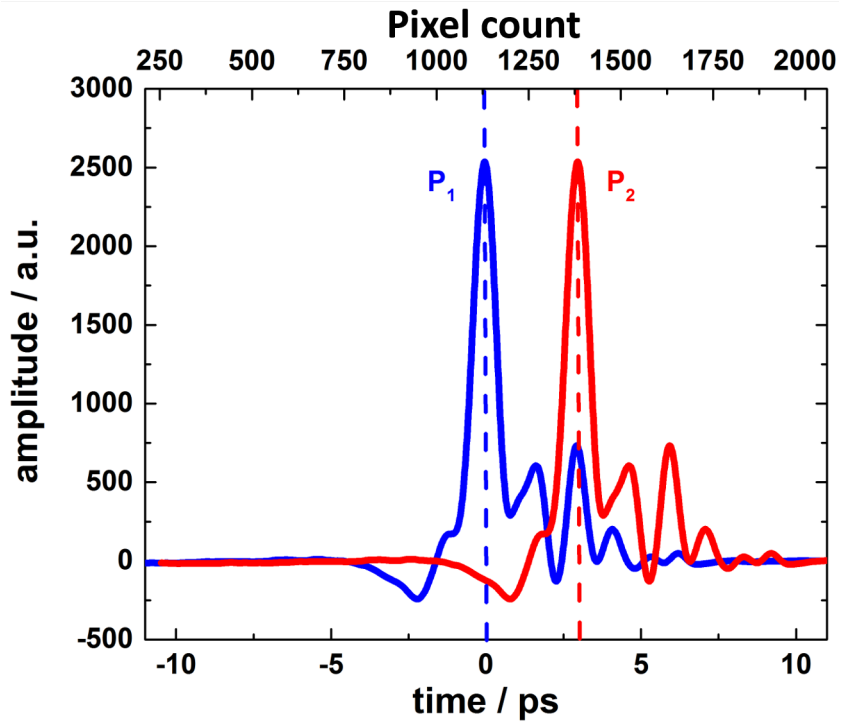

Figure 2.17: SD traces as measured by the CDR ATM. The blue and red SD traces represent two THz-pulses with different arrival time relative to the laser pulse. The upper x-axis shows the pixel count on the spectrometer sensor and the lower x-axis shows the arrival time using the pixel-wavelength-arrival time mapping. P_1 and P_2 denote the primary peak positions of both traces, respectively.

Arrival time correction

The *determined* arrival time of each pulse can be used for arrival time correction, i.e., for re-sorting the data points according to their actual *determined* arrival time. As an illustration, the EO sampling (see Section 2.3 for details about EO sampling.) measurement result of the undulator pulse is shown as raw data and after applying data correction in Figure 2.18. The raw experimental signal (S) shown in Figure 2.18(a), is plotted using only the delay line position (T), without the correction of the *real* arrival time τ. Figure 2.18(b) shows the EO sampling trace after applying arrival time correction: $(T + \tau, S)$. It can be clearly seen that a significant enhancement of the Signal-to-noise Ratio (SNR) is achieved after data correction.

Data binning

Data binning is the last step of the *post mortem* data treatment process aiming at reducing the random noise. During data binning, the signal of the data points that have both nearly

the same arrival time and that lie in a defined small interval of intensity (ΔI) will be averaged: $S_{\text{binned}} = \bar{S}|_{t=T+\tau}$. After signal averaging, the data set is reduced to $(t = T + \tau, S_{\text{binned}})$, as can be seen in Figure 2.18(c). An optimal temporal resolution of 13 fs (RMS) can be reached with the currently used single ATM-based DAQ system. Please note, the achievable temporal resolution also depends on the operation status of the accelerator, i.e., when the accelerator is operating unstably, the temporal resolution also decreases accordingly.

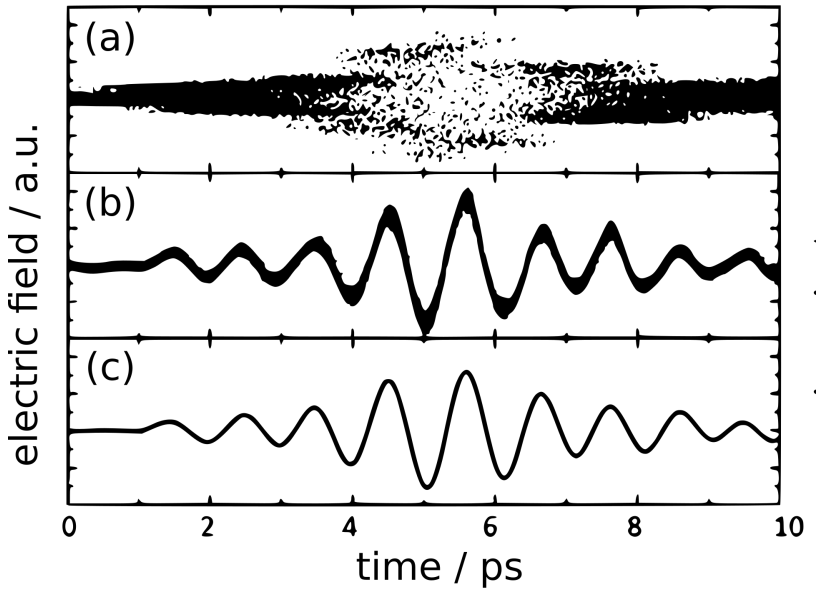

Figure 2.18: Individual steps of the *post mortem* data treatment procedure in the pulse-resolved DAQ system. (a) The undulator waveform plotted using the as-measured raw data. (b) The undulator waveform plotted after applying arrival time correction. (c) The time-corrected undulator waveform plotted with data binning. Taken from [32].

2.3 THz detection techniques

The results shown in this thesis were obtained by using various THz detection and characterization techniques. The most important parameters that need to be measured are the THz pulse energy and the THz waveform.

THz detection methods can be roughly divided into two main categories: methods using incoherent detectors and methods utilizing coherent detection in the time-domain. The main difference between these approaches is that, for incoherent direct detectors, typically only the intensity/pulse energy of the signal is measured. Exemplary direct detectors are Bolometers, Golay cells, or pyroelectric detectors. These detectors absorb the energy of the THz wave in an appropriate absorber material. This eventually leads to a temperature increase which is converted into an electrical signal.

In time-domain coherent detection, both the amplitude and the *phase* of the THz electric field are measured. The most commonly used coherent detection methods are photoconductive antennas and EO sampling. The two fundamental approaches and corresponding detector types are explained in more detail in the following.

2.3.1 Incoherent pyroelectric THz detectors

As mentioned in previous sections, a high-speed pyroelectric detector is implemented at TELBE for pulse-resolved THz intensity monitoring. Pyroelectric materials, such as InAsSb and $LiTaO_3$, exhibit surface charges induced by the spontaneous electric polarization of the unit cell of the crystal. In the thermodynamic equilibrium state, the surface charge does not lead to any macroscopic dipole. However, a thermodynamic change can be induced by, e.g., incident radiation that results in a reduction of the surface charge [73]. This change of the surface charge is then detected by the electrodes attached to the two sides of the material and further converted to a voltage or current change depending on the type of the electric circuit. Therefore, after choosing an appropriate absorber for THz radiation, THz radiation can be detected by pyroelectric materials by measuring voltage or current changes.

A structural scheme of a conventional pyroelectric detector is shown in Figure 2.19. The absorber material absorbs the energy of the THz radiation and then transmits the heat to the pyroelectric material. The heat-induced voltage change is guided by the top and bottom electrode to the amplifier, where it is read out.

The pyroelectric detectors used at TELBE were developed at DESY [74] for THz radiation detection. This detector can operate at a maximal repetition rate of 1 MHz.

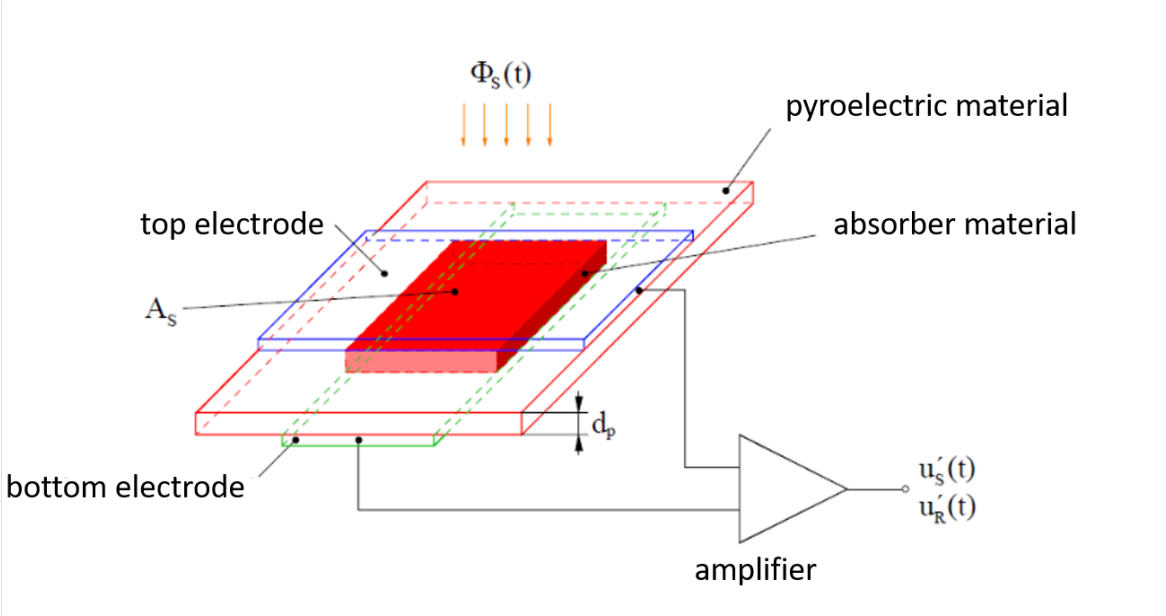

Figure 2.19: Schematic of a pyroelectric detector. The detector contains a sensitive element for improving the radiation absorption, a pyroelectric material, a pair of top and bottom electrode to extract the current, and a signal amplifier. A_s is the area of the sensitive element. $\Phi_s(t)$ is the incident radiation flux. d_p is the thickness of the pyroelectric material. $\tilde{u}_{s'}$ is the RMS value of the sinusoidal signal voltage at the detector output. $\tilde{u}_{R'}$ is the RMS value of the noise voltage at the detector output. Taken from [75].

2.3.2 Electro-optic sampling

2.3.2.1 Free space electro-optic sampling in electro-optic crystals

As a coherent detection technique, free space EO sampling measures the temporal waveform of a THz pulse in the time domain recording both its amplitude and phase information. Figure

2.20 illustrates the scheme of the EO sampling process. In this method, a THz pulse and a linearly polarized ultrashort near infrared probe laser pulse propagate collinearly through an EO crystal.

Because of the Pockels effect, the electric field of the THz pulse induces a change of the refractive indices of the EO crystal. Different polarization components of the optical pulse experience a different refractive index that leads to phase retardation between them. After exiting the EO crystal, the polarization state of the probe pulse carries the electric field strength-information of the THz pulse. After passing through a Quarter Waveplate (QWP) and a Wollaston prism, two orthogonal components of the probe pulse are separated spatially and then detected independently by two photodiodes. When the probe pulse propagates without interaction with the THz pulse, the photodiodes' signal is balanced – by adjusting the orientation of the QWP – so that the detector gives zero signal. In presence of the THz pulse, an imbalanced signal is thereby created between both orthogonal components which is proportional to the electric field strength of the THz pulse.

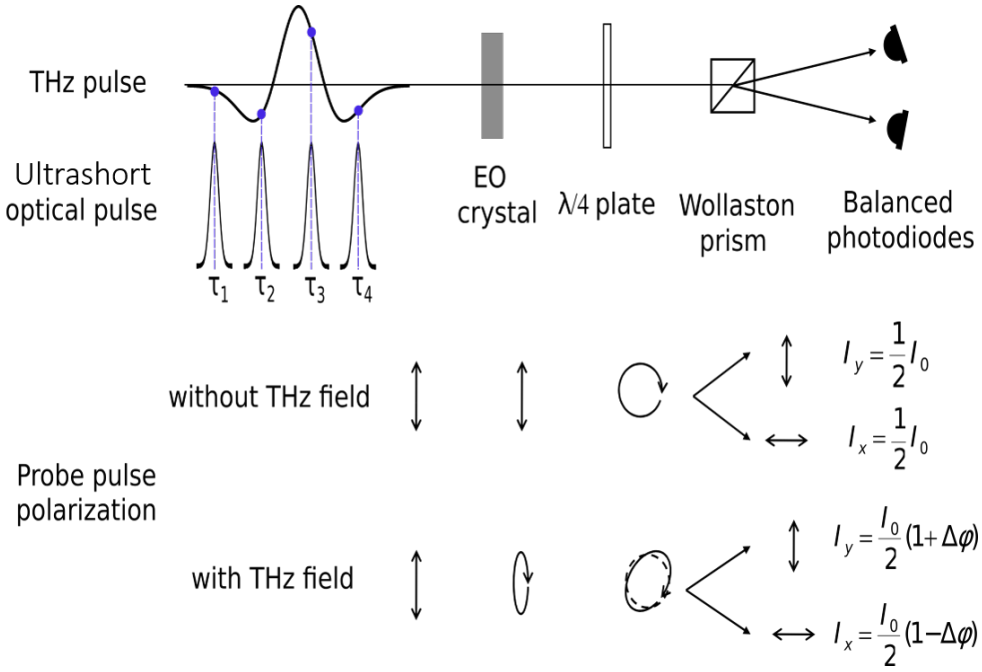

Figure 2.20: Schematic diagram of the free space EO sampling, showing the elements used for EO sampling and the polarization state of the probe pulse after each element with and without the presence of the THz pulse. $\tau_{1,\ldots 4}$ indicates the relative delay between THz and probe pulse. I_0, I_x, and I_y represent the intensity of the probe pulse, the intensity of the horizontally polarized component and the intensity of the vertically polarized component, respectively. $\Delta\varphi$ is the THz field-induced differential phase retardation of the probe pulse. Modified from [73]. Republished with permission of Springer; permission conveyed through Copyright Clearance Center, Inc.

The whole process is now described in detail: after propagating with the THz pulse for a distance L (the thickness of the EO crystal) in the EO crystal made of, e.g., ZnTe, the two orthogonal components of the probe pulse experience a differential phase retardation of $\Delta\phi$ caused by the Pockels effect. The phase retardation $\Delta\phi$ can be written as:

$$\Delta\phi = (n_y - n_x)\frac{\omega L}{c} = \frac{\omega L}{c} n_{\mathrm{O}}^3 r_{41} E_{\mathrm{THz}}, \tag{2.13}$$

where n_x and n_y are the refractive indices experienced by the x and y polarization component of the probe pulse, ω is the central frequency of the probe pulse, c is the speed of light in vacuum, n_O is the refractive index of the EO crystal at frequency ω, r_{41} is the EO coefficient of the EO crystal that belongs to the $\bar{4}3m$ space group in case of the typically used ZnTe crystal [76], and E_{THz} is the electric field strength of the THz pulse. This equation shows the linear dependence of field retardation and THz field strength.

The intensity of the two orthogonal polarization components I_x and I_y, which are separated by the Wollaston prism and then detected, can be expressed by:

$$\begin{aligned} I_x &= \frac{I_0}{2}(1 - \sin\Delta\phi) \approx \frac{I_0}{2}(1 - \Delta\phi), \\ I_y &= \frac{I_0}{2}(1 + \sin\Delta\phi) \approx \frac{I_0}{2}(1 + \Delta\phi), \end{aligned} \tag{2.14}$$

where I_0 is the intensity of the probe pulse incident on the ZnTe crystal. Please note, that here the small signal approximation $(I_y - I_x)/(I_y + I_x) \ll 1$ is used. In this approximation, second order effects on THz fields are neglected and $\sin\Delta\phi \approx \Delta\phi$ is assumed. The difference signal I_s between the two photodiodes can be obtained by substituting I_x with I_y [73, 77, 78]:

$$I_s = I_y - I_x = I_0\Delta\phi = \frac{I_0\omega L}{c} n_{\mathrm{O}}^3 r_{41} E_{\mathrm{THz}} \propto E_{\mathrm{THz}}. \tag{2.15}$$

As can be seen from Equation 2.15, the output signal is directly proportional to the THz electric field strength, and hence this method can retrieve the whole THz pulse waveform by changing the relative temporal delay between the probe and the THz pulse, as shown in Figure 2.20.

However, there are a few factors that limit the performance of the EO sampling in practice: such as (i) probe pulse duration, (ii) phase mismatch between the THz and the probe pulse, (iii) absorption and dispersion inside the EO crystal, and (iv) Fabry-Perot effects induced by the EO crystal [78]. Among all these factors, the phase mismatch is the most critical one since they determine the cut-off frequency of the EO sampling, i.e. the highest THz frequency that can be detected.

In general, the spectrum of the EO sampling signal $I_s = I_y - I_x$ can be expressed by Equation 2.16 [78].

$$I_{\mathrm{s}}(\omega_{\mathrm{THz}}) \propto A_{\mathrm{opt}}(\omega_{\mathrm{THz}}) \cdot \chi^{(2)}(\omega; \omega_{\mathrm{THz}}, \omega - \omega_{\mathrm{THz}}) \cdot \Delta\Phi(\omega, \omega_{\mathrm{THz}}) \cdot E_{\mathrm{THz}}(\omega_{\mathrm{THz}}), \tag{2.16}$$

where $A_{\mathrm{opt}}(\omega_{\mathrm{THz}})$ is the spectrum of the autocorrelation of the optical probe pulse, $\chi^{(2)}(\omega; \omega_{\mathrm{THz}}, \omega - \omega_{\mathrm{THz}})$ is the second order nonlinear susceptibility of the EO crystal in frequency domain and $\Delta\Phi(\omega, \omega_{\mathrm{THz}})$ is the phase mismatch term. These three factors are effectively acting as a frequency filter.

$A_{\mathrm{opt}}(\omega_{\mathrm{THz}})$ is determined by the probe pulse duration. Figure 2.21 shows the relationship between probe pulse duration and and the spectral sensitivity of EO sampling (only the $A_{\mathrm{opt}}(\omega_{\mathrm{THz}})$ term is taken into consideration in Equation 2.16). As shown by Figure 2.21, the 50 % amplitude response of the 100 fs probe pulse is around 1.25 THz, i.e., shorter probe

pulse should be used when performing EO sampling of THz pulse with frequency higher than 1.25 THz.

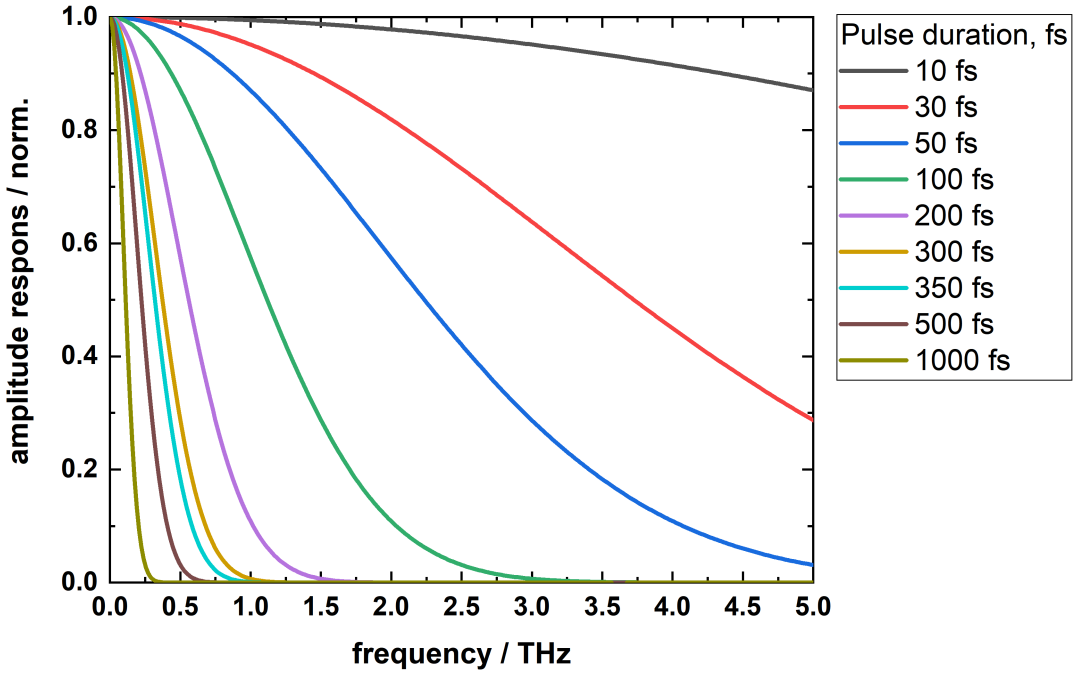

Figure 2.21: Relationship between the probe pulse duration and the spectral sensitivity of EO sampling (Only the $A_{\text{opt}}(\omega_{\text{THz}})$ term is taken into consideration in Equation 2.16). Traces with different colors represent spectral EO sampling responses when probe pulses have pulse duration of 10, 30, 50, 100, 200, 300, 350, 500 and 1000 fs. The cutoff frequency increases when the pulse duration decreases. Please note, all the pulse durations shown in this figure are defined as FWHM pulse duration.

Another critical term affecting the frequency response of the EO sampling method is the phase mismatch term $\Delta\Phi(\omega, \omega_{THz})$, which can be described by Equation 2.17.

$$\Delta\Phi(\omega, \omega_{\text{THz}}) = \frac{e^{i\Delta k(\omega,\omega_{\text{THz}})L} - 1}{i\Delta k(\omega, \omega_{\text{THz}})}, \tag{2.17}$$

where L is the thickness of the crystal and $\Delta k(\omega, \omega_{\text{THz}})$ can be further written as:

$$\begin{aligned} \Delta k(\omega, \omega_{\text{THz}}) &= k(\omega) - k(\omega_{\text{THz}}) - k(\omega + \omega_{\text{THz}}) \\ &\approx \frac{\partial k}{\partial \omega} \cdot \omega_{\text{THz}} - k(\omega_{\text{THz}}) \\ &\approx \omega_{\text{THz}} \cdot (n_{gr} - n_{\text{THz}}), \end{aligned} \tag{2.18}$$

where n_{gr} is the group refractive index of the probe laser pulse and n_{THz} is the refractive index of the THz pulse.

Therefore, in order to ensure a high THz detection sensitivity and cutoff frequency, an appropriate type of EO crystal need to be chosen to ensure a minimal difference between the group velocity of the laser pulse and the phase velocity of THz pulse [73]. For instance, when the probe laser pulse has a central wavelength of 800 nm, ZnTe is highly suitable because of the matching refractive indices $n_{\text{gr}}(\lambda_{\text{probe}} = 812\,\text{nm}) = n_{\text{THz}}(\nu_{\text{THz}} = 1.69\,\text{THz}) = 3.22$.

In practice, when other parameters are fixed, on the one hand, a large EO crystal thickness L, can increase the EO signal according to Equation 2.15. On the other hand, as shown by Equation 2.17, it also limits the highest detectable frequency of the THz pulse. In experiments, a trade-off between EO signal strength and highest detectable frequency needs to be made based on the experimental requirements.

2.3.2.2 Single-shot electro-optic detection technique

Conventional free space EO sampling is a precise and robust technique, but it has one major drawback: It cannot detect THz field transients of single pulses, because the field transients are measured by sequential sampling of many THz pulses with the help of a comparably slow delay stage. This means that only repeated and phase-stable THz pulses can be characterized. The method of single-shot THz detection introduced in this section can overcome these limitations.

One possible implementation of a single-shot THz detection scheme is the so-called Spectral Decoding (SD) method. As illustrated in Figure 2.22, a linearly chirped laser probe pulse propagates collinearity with a THz pulse into an EO crystal. The chirp typically corresponds to a pulse duration on the order of a few picoseconds which ensures temporal overlap with the whole THz pulse. As a consequence, different frequency components of the probe pulse overlap in time with different portions of the THz field while both beams propagate through the EO crystal. Analogous to the free-space EO sampling, the THz field modulates the birefringence of the EO crystal. For more details, please refer to [79].

A set of polarizers before and after the EO crystal only allows transmission of portions of the chirped pulse which correspond to a THz-induced polarization change. Thereby, the polarization modulation of different spectral components is converted into an transmission modulation and can be directly detected by a spectrometer. As shown in Fig. 2.22, the THz field is eventually imprinted onto the spectrum of the chirped probe pulse. By detecting the spectrum of the chirped pulse in an optical spectrometer, the THz pulse's waveform and its relative timing can be retrieved [80].

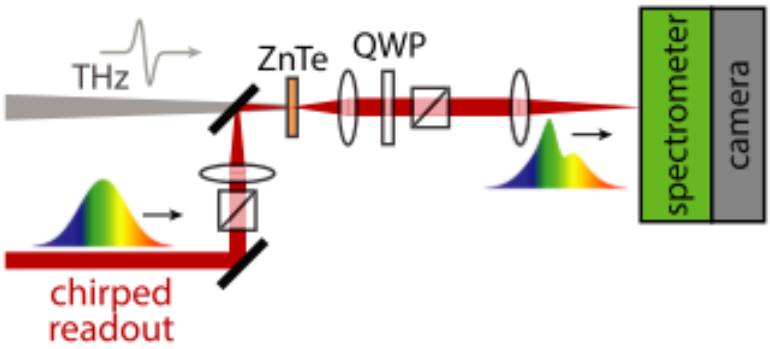

Figure 2.22: Schematic of single-shot EO detection via spectral decoding. A chirped optical pulse and a THz pulse are sent collinearly into a ZnTe crystal, which is placed in between two quasi-crossed polarizers. After the THz-induced polarization modulation within the ZnTe crystal, the chirped pulse is focused into a spectrometer, where the THz field can be measured as an imprint on the intensity spectrum of the chirped pulse. Taken from [80]. Republished with permission of American Institute of Physics; permission conveyed through Copyright Clearance Center, Inc.

In the scheme with two crossed polarizers placed in the path of the chirped probe pulse before and after the EO crystal, as it is shown in Figure 2.22, the electrical field of the optical pulse

$E_{\mathrm{m}}(t)$ modulated by a THz pulse $E_{\mathrm{THz}}(t)$ is given by $E_{\mathrm{m}}(t) = [1 + \alpha E_{\mathrm{THz}}(t)]\, E_{\mathrm{bg}}(t)$, where α is the coefficient representing the overall modulation strength, $E_{\mathrm{bg}}(t)$ is the background optical field leaking through the second crossed polarizer in the absence of the THz pulse, which is caused by the residual birefringence of the EO crystal [81]. For convenience, the above equation can be rewritten as $E_{\mathrm{m}}(t) = E_{\mathrm{bg}}(t) + E_{\mathrm{s}}(t)$, where the signal term is $E_{\mathrm{s}}(t) = \alpha E_{\mathrm{THz}}(t) E_{\mathrm{bg}}(t)$. The interference between these two terms can be expressed in frequency domain by:

$$I_m(\omega) \equiv |\widetilde{E}_m(\omega)|^2 = \alpha^2[|\widetilde{E}_{\mathrm{bg}}(\omega)|^2 + |\widetilde{E}_{\mathrm{s}}(\omega)|^2 + \widetilde{E}^*_{\mathrm{bg}}(\omega)\widetilde{E}_{\mathrm{s}}(\omega) + \widetilde{E}_{\mathrm{bg}}(\omega)\widetilde{E}^*_{\mathrm{s}}(\omega)], \tag{2.19}$$

where $I_{\mathrm{m}}(\omega)$ is the final spectral intensity distribution directly measured by the spectrometer, $\widetilde{E}_m(\omega)$, $\widetilde{E}_{\mathrm{bg}}(\omega)$, and $\widetilde{E}_{\mathrm{s}}(\omega)$ are the Fourier transforms of $E_m(t)$, $E_{\mathrm{bg}}(t)$, and $E_{\mathrm{s}}(t)$, respectively. The background term $|\widetilde{E}_{\mathrm{bg}}(\omega)|^2$ can be directly measured by taking a spectrum when blocking the THz field. The difference spectrum $\Delta I(\omega) \equiv I_m(\omega) - |\widetilde{E}_{\mathrm{bg}}(\omega)|^2$ can be obtained after subtracting the background term [79, 82, 81].

In cases when the amplitude of $E_{\mathrm{THz}}(t)$ is small compared to the background, the signal term $|\widetilde{E}_{\mathrm{s}}(\omega)|^2$ can be neglected and only the interference term $\alpha^2[\widetilde{E}^*_{\mathrm{bg}}(\omega)\widetilde{E}_{\mathrm{s}}(\omega) + \widetilde{E}_{\mathrm{bg}}(\omega)\widetilde{E}^*_{\mathrm{s}}(\omega)]$ is left. By substituting the Fourier transform $\widetilde{E}_{\mathrm{s}}(\omega) = \int_{-\infty}^{\infty} E_{\mathrm{THz}}(t) E_{\mathrm{bg}}(t) e^{i\omega t} dt$, the interference term can be rewritten as:

$$\Delta I(\omega) = \alpha^2[E^*_{\mathrm{bg}}(\omega) \int_{-\infty}^{\infty} E_{\mathrm{THz}}(t) E_{\mathrm{bg}}(t) e^{i\omega t} dt + E_{bg}(\omega) \int_{-\infty}^{\infty} E_{\mathrm{THz}}(t) E^*_{\mathrm{bg}}(t) e^{-i\omega t} dt]. \tag{2.20}$$

Therefore, under the so-called linear operation mode, a linear relationship between the signal and the THz field can be obtained: $\Delta I(\omega) = \alpha^2 \mathbf{B} E_{\mathrm{THz}}(t)$, where $B_{\omega,t} = E^*_{\mathrm{bg}}(\omega) E_{\mathrm{bg}}(t) e^{i\omega t} + E_{\mathrm{bg}}(\omega) E^*_{\mathrm{bg}}(t) e^{-i\omega t}$.

In another case, when the incident THz field is strong enough while enabling much smaller background leakage by tuning the crossed polarizers, the signal term $|\widetilde{E}_{\mathrm{s}}(\omega)|^2$ becomes dominant and the difference spectrum turns into $\Delta I(\omega) \propto |E_{\mathrm{THz}}(t)|^2$. Under this so-called quadratic operation mode, the measured difference spectrum is proportional to the rectification of the THz pulse.

Compared to the conventional free space EO sampling method, the single-shot THz detection method is capable of measuring single-pulse THz field transients without the need of a delay stage. At the same time, the finite bandwidth of the chirped pulse and the operation near the cross-polarization point, can produce severe distortion of the measured THz waveform [83]. Due to this, the single-shot EO detection scheme at TELBE is only utilized for timing determination. The *position* of the main peak in the THz waveform is on the contrary not affected by the distortion and the arrival time can be hence defined by, e.g. the occurrence of maximum THz field strength in the waveform.

In summary, the single-shot THz detection method is used for the ATM systems at TELBE since it enables timing determination based on the THz pulse waveform within one single shot. For determining the exact waveform of the THz pulse, conventional EO sampling is performed, which requires a slow mechanical delay stage for a sequential scan of the THz pulses' field. Besides spectral decoding, there are also other techniques for single-shot THz detection that

can be employed in an ATM, such as spatial or temporal EO sampling. An example of an application of spatial decoding in given in Section 2.4.

2.4 State-of-the-art THz diagnostics at accelerators

2.4.1 Longitudinal electron bunch diagnostics using coherent transition or diffraction radiation

Both CDR and CTR are processes in which part of the kinetic energy of an electron bunch is transformed into THz radiation. This radiation carries information on the characteristics of the respective electron bunch, so that THz emission from these types of radiators can be used for further bunch diagnostics. The underlying physical principles of CTR and CDR are very similar. As described in Section 2.1, the essential difference is that, for CTR, the electron bunch actually propagates *through* the target material, which is a metallic screen at TELBE. For CDR, the screen has an aperture which allows the electron bunch to pass near the actual screen material. In both cases the change of the dielectric environment along the electron bunch trajectory generates broadband THz radiation via Coulomb interaction. Because of the similarity of the emission mechanisms, here, only the method of CTR-based electron bunch length diagnostics will be discussed in detail. Here, a briefly introduction is given based on Ref. [84].

The power spectrum of the CTR signal is given by

$$I(\omega) = N(N-1)I_{\mathrm{e}}|f(\omega)|^2, \tag{2.21}$$

where N is the total number of electrons in the electron bunch, I_e is the radiated power emitted by a single electron and $f(\omega)$ is the so-called form factor of the electron bunch [85]. The form factor can be further described by

$$f(\omega) = \int \rho(z) \exp(i\omega z/c) dz, \tag{2.22}$$

where $\rho(z)$ is the so-called normalized longitudinal electron bunch distribution, i.e. it is assumed that the beam is highly focused transversely.

The normalized longitudinal electron bunch distribution $\rho(z)$ known as

$$\rho(z) = \frac{1}{\pi c} \int_0^\infty \kappa(\omega) \cos[\psi(\omega) - \omega z/c] d\omega, \tag{2.23}$$

can be obtained if $\kappa(\omega) \equiv \sqrt{I(\omega)}$ and the frequency-dependent term $\psi(\omega)$ are known. $\kappa(\omega)$ can be obtained easily since $I(\omega)$ can be directly measured. The other term $\psi(\omega)$ can also be calculated by using the following approximation according to the Kramers-Kroning method.

$$\psi(\omega) = -\frac{2\omega}{\pi} \int_0^\infty dx \frac{\ln[\kappa(x)/\kappa(\omega)]}{x^2 - \omega^2}, \tag{2.24}$$

From the equations listed above, the longitudinal charge distribution $\rho(z)$ can be deduced from a directly measurable parameter: the power spectrum $I(\omega)$.

The power spectrum can be measured either through sequential EO sampling or a THz spectrometer in combination with a THz power detector. Measurements of the latter type

have been routinely performed at the FLASH FEL for femtosecond electron bunch diagnostics for more than one decade [74].

2.4.2 Electron beam length and arrival time monitor based on EO interaction in the nearfield of the electron bunch

Another technique to measure the electron beam length is directly monitoring the near field Coulomb interaction of the relativistic electron bunch with the laser pulse in an EO crystal via the EO effect. This method is based on single-shot THz pulse detection technique [79, 86], as previously described in Section 2.3. The only difference is, that this method utilizes the Coulomb field of the relativistic electron bunch instead of free space THz pulses.

In Figure 2.23, a scheme of an electron bunch length monitor based on spectral decoding is shown. A laser pulse with initial pulse duration of T_0 is chirped to T_c, which is longer than the electron bunch duration. Then the chirped laser pulse interacts with the Coulomb field of the electron bunch inside the EO crystal, which is placed close to the electron bunch trajectory. The ellipticity of the polarization of the chirped pulse is proportional to the Coulomb field of the electron bunch, and hence has the same temporal structure. After tuning the polarizer placed after the EO crystal, the elliptical polarization can be converted into intensity modulation. Finally, with the time-wavelength relationship of the chirped pulse, the bunch profile can be deduced from the modulated spectrum [87].

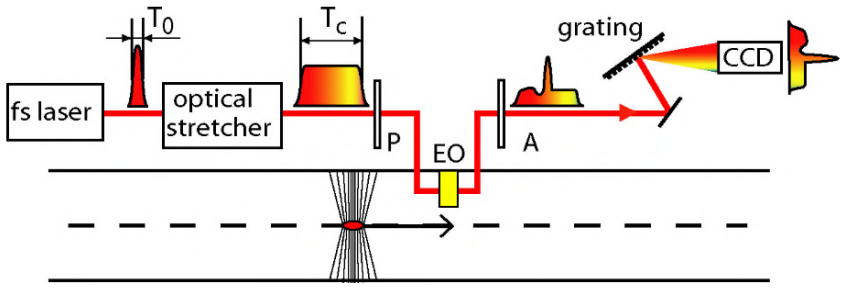

Figure 2.23: Schematic of EO interaction-based electron beam profile monitor. The laser pulse is stretched and then interacts with the Coulomb field of the electron bunch in the EO crystal. The intensity-modulated spectrum of the chirped pulse is obtained by a grating-based spectrometer. Taken from [88].

Another variant of this method known as the spatial decoding technique is shown in Figure 2.24. By changing the incident direction of a chirped laser beam from normal to oblique, the front part (Figure 2.24(a)) and the back part (Figure 2.24(b)) of the electron bunch interact with different portions of the laser pulse. Therefore, the arrival time and the duration of the electron bunch can be measured.

This approach, also known as spatial encoding, has been shown to provide sub-100 fs precision in arrival time measurements at the The Sub-picosecond Pulse Source (SPPS) at Stanford Linear Accelerator Center (SLAC) [89].

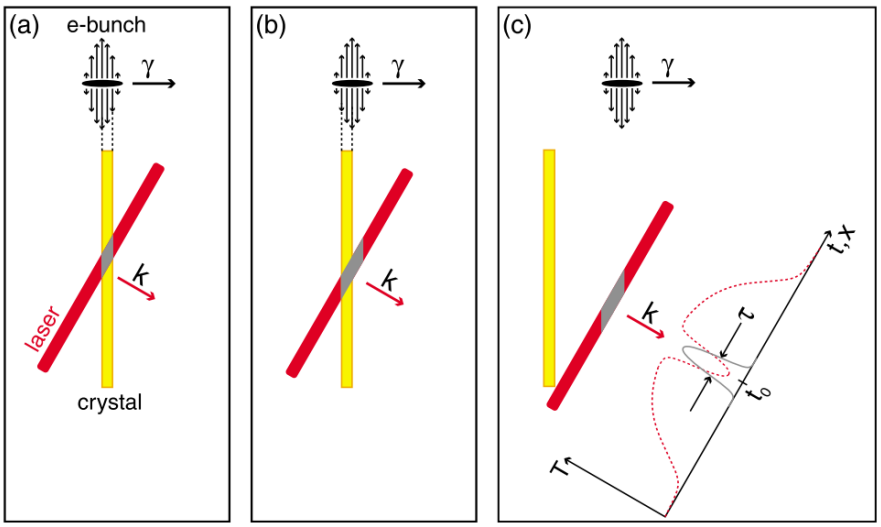

Figure 2.24: Schematic of the ATM based on the EO spatial decoding. The Coulomb field of the electron bunch interacts with the laser pulse, which is incident under an angle relative to the EO crystal which is placed adjacent to the electron bunch trajectory. The gray area is the portion of the laser pulse that interacts with the Coulomb field via the EO effect inside the crystal. The bunch profile is imprinted onto the transmitted laser pulse. In (c), τ is the bunch duration and t_0 is the arrival time of the electron bunch. Taken from [89]. Reprinted figure with permission from A.L. Cavalieri et al, Clocking Femtosecond X Rays, 94, 114801, 2005. Copyright (2005) by the American Physical Society.

2.5 State-of-the-art of intrinsic synchronization techniques at accelerator-based lightsources

2.5.1 Femtoslicing enabled intrinsic synchronization

Up to now, two diagnostic methods which allow active control of the temporal stability between light pulses generated by an accelerator and an external laser have been introduced. A third approach is based on the idea to synchronize the accelerators and the lasers passively or as it is sometimes called intrinsically. One of the first successfully demonstrated concepts was introduced in 1996 [90, 91]. Initially, this so-called "femtoslicing" concept was used to generate femtosecond x-ray pulses at synchrotron storage rings, where the long electron bunch distribution dictated that only long X-ray pulses in the below 10 ps-regime or longer can be generated.

The principle of the slicing process can be understood as follows: an ultrashort femtosecond laser pulse is sent to a radiator overlapping with a relatively long electron bunch. The laser pulse modulates the electron energy of a small portion of the bunch with its high electric field. Thereby, it effectively slices out a portion of the electron bunch. The energy modulation of the electron bunch is later converted into a spatial modulation, which is achieved by passing the bunch through a set of dispersive bending magnets. The sliced electron bunch emits a femtosecond X-ray pulse, when it is passing through a radiator, e.g., another bend magnet. A schematic diagram of the principle is shown in Figure 2.25.

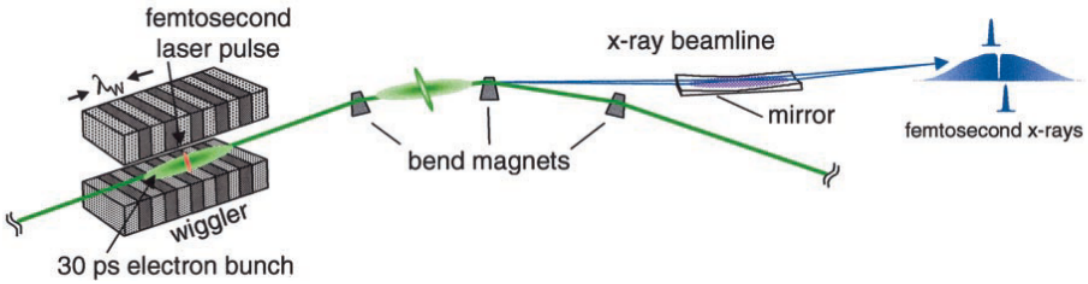

Figure 2.25: Schematic of the "femtoslicing" technology. A femtosecond laser pulse is used to modulate a small portion of the typically 30 ps long electron bunch inside the undulator. λ_w is the period of the undulator. A femtosecond x-ray pulse can be obtained by separating the modulated and the unmodulated portion of the electron bunch. Taken from [91]. Republished with permission of American Association for the Advancement of Science; permission conveyed through Copyright Clearance Center, Inc.

A second advantage of this technique is that the resulting femtosecond X-ray pulse is intrinsically synchronized to the laser pulse as a consequence of the slicing process. With the intrinsically synchronized sliced accelerator-based pulse and the external laser pulse, ultrafast pump-probe experiments can be performed with high temporal resolution without investing additional effort in synchronization. This benefit is significant because it enables few-femtosecond level synchronization without investing into a large expensive timing control scheme or arrival time monitoring system. Moreover, the operational principle allows the source to operate at very high repetition rates, up to few megahertz.

The "femtoslicing" concept was experimentally proven for the first time in 2000 at the Advanced Light Source (ALS) in Berkeley [91].

2.5.2 Seed laser-induced intrinsic synchronization

Another method which leads to intrinsic synchronization between a laser and accelerator-based light pulses is the so-called seeded-FEL scheme.

For an FEL using the High Gain Harmonic Generation (HGHG) method, there are two synchronized external laser systems. Laser pulses from the user laser are used as a probe for pump-probe experiments. Laser pulses from the seed laser are sent into the FEL undulator, copropagating with the electron bunches. During the copropagation of the seed laser pulse and the electron bunch in an undulator known as "modulator", the electron bunch is modulated in energy by the seed laser pulse. This energy modulation is further converted to a density modulation of the electron bunch which generates an XUV/X-ray pulse after passing through another undulator known as "radiator". Because of the modulation relationship between the seed laser and the electron bunch, the FEL pulse and the seed laser pulse are again intrinsically synchronized [92].

Figure 2.26 shows an example of this layout built at the FERMI FEL that uses the HGHG mechanism to generate XUV pulses. The system utilizes an optical laser oscillator to synchronize the seed laser and the user laser for probing the respective dynamics at the experimental endstation. The principle of HGHG enables intrinsic synchronization between the XUV pulse and the seed pulse. The system has been experimentally proven to yield a timing jitter as small as 6 fs (RMS) at the experimental endstation of the FERMI FEL [93, 94].

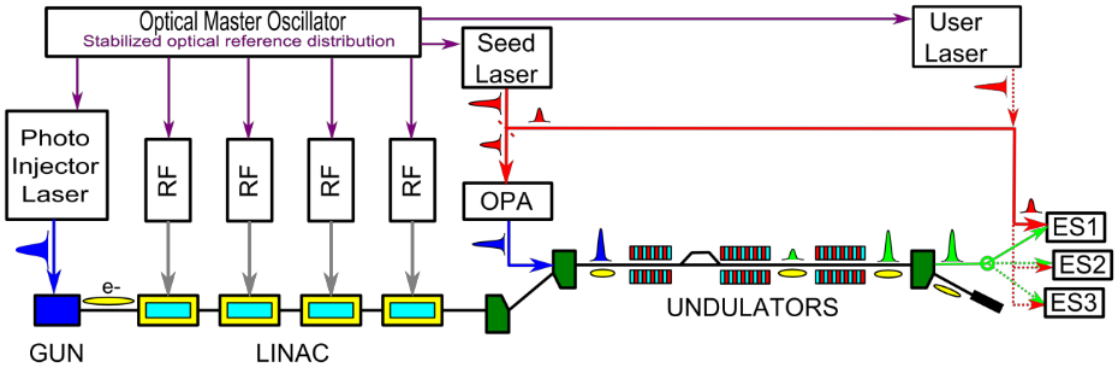

Figure 2.26: Schematic of the seed laser-induced intrinsic synchronization technology. An optical master oscillator is used to distribute the timing signal to the photo-injector laser, RF components, the seed laser and the user laser. The red pulse represents the IR optical pulse, the yellow ellipse represents the electron bunch and green pulse represents the FEL pulse. Taken from [93]. Copyright 2014, Optical Society of America.

Within the framework of this thesis, inspired by the "femtoslicing" concept, another novel intrinsic synchronization method, which is coined as "THz-slicing" has been developed. This method offers the passive, all-optical synchronization of an accelerator-based THz source with a femtosecond laser, as explained in detail in Chapter 4.

3

Upgrade of the pulse- and field-resolved THz diagnostics at TELBE

3.1 Upgrade of the pulse- and field-resolved THz diagnostics at TELBE – Motivation

The current DAQ system with CDR ATM enables the implementation of ultrafast pump-probe experiments at a typical arrival time uncertainty of 13 fs (RMS) [32] which already enabled a number of breakthrough experiments [36, 95]. As explained previously in Section 2.2.4, the relative arrival time between the CDR and laser pulse can be considered as the relative arrival time between undulator and laser pulse as a result of the intrinsic synchronization of CDR and undulator pulse. However, on *rare* occasions, because of strong electron bunch energy fluctuations and/or electron bunch trajectory instabilities, up to a few hundreds of femtoseconds jitter between the CDR source and the undulator source have been observed, as shown in Figure 3.1.

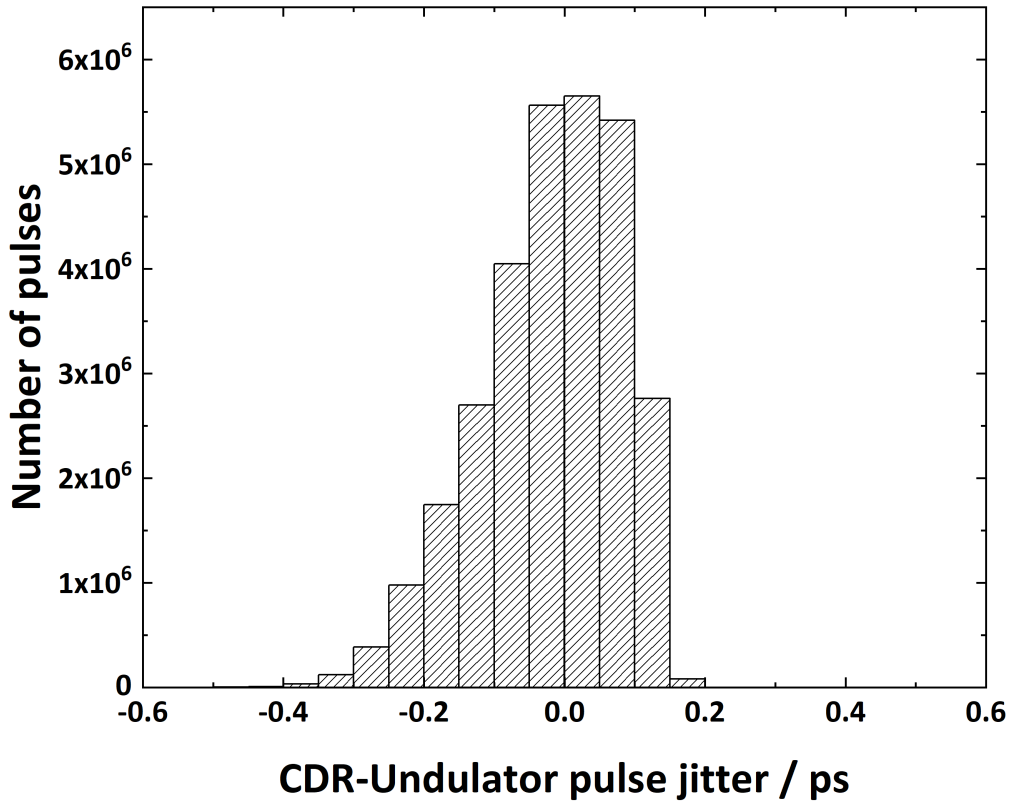

Figure 3.1: Histogram of the undulator-CDR pulse jitter that is measured by the double-ATM-based pulse- and field-resolved THz diagnostics technique developed within this thesis. On this occasion, a significant number of pulses shows a jitter exceeding 100 fs. For details about this method, please see Section 3.2.

The possible accelerator instabilities leading to CDR-undulator jitter, as mentioned above, directly affect the performance of the single CDR ATM. In worst-case scenarios, this may have detrimental effects on the performance of ultrafast pump-probe experiments at TELBE. For this reason, an additional, dedicated undulator ATM was implemented as part of this thesis to measure the undulator-laser arrival time directly in order to avoid the influence of the CDR-undulator jitter and to improve the timing accuracy further [96].

In this chapter, as an upgrade of the routinely used pulse-resolved DAQ method at TELBE, a newly developed double-ATM-based pulse- and field-resolved THz diagnostics technique is introduced. This chapter includes the description of the experimental setup (see Section 3.2), the data analysis method (see Section 3.3) and the experimental results (see Section 3.4) of the new technique. As a result, a 4 fs (RMS) timing precision was achieved with this pulse- and field-resolved THz diagnostics technique.

This new double-ATM scheme is shown in Figure 3.2(a). In the new scheme, two ATMs are installed to measure the relative CDR-laser (τ_1) and undulator-laser (τ_2) arrival times simultaneously.

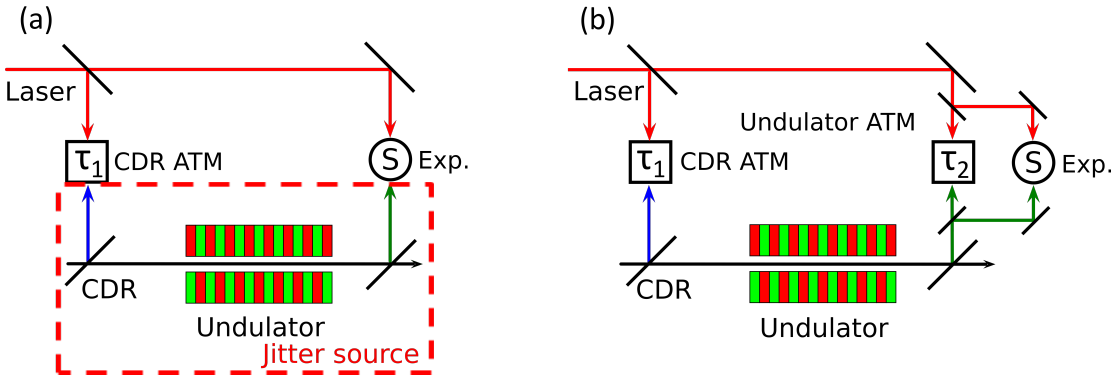

Figure 3.2: Block diagrams of the single and double-ATM DAQ schemes. (a) The double-ATM system implemented within this thesis, where an additional undulator ATM is added to measure the relative undulator-laser pulse arrival time labeled as τ_2. (b) The original single ATM system operated at TELBE since 2016. τ_1 is the relative arrival time between the CDR and laser pulse measured by the CDR ATM while the symbol S indicates the pump-probe experiment. The red dashed rectangle marks the elements of the facility, from which undulator-CDR jitter can originate.

Besides the relative arrival time between the undulator, CDR , and laser pulse, pulse-resolved multidimensional information about the undulator pulse can also be easily deduced from the Spectral Decoding (SD) trace measured by the undulator ATM. The data analysis method for determining the arrival time and the undulator pulse intensity from its SD trace can be found in Subsection 3.3.1 and 3.3.2, respectively. The detailed analysis of the correlations between these multidimensional datasets, such as arrival time-frequency correlation and arrival time-pulse intensity correlation, is described in Subsection 3.4.2.

3.2 Experimental setup

The experimental setup of the double-ATM scheme is shown in Figure 3.3. It consists of two ATMs, which detect the THz pulses from the CDR source and the undulator source in parallel. Further, one pyroelectric detector independently measures the intensity of the undulator pulse. In a typical ultrafast experiment at TELBE, the THz pulses from the undulator serve as pump pulses while fs laser pulses serve as probe. In Figure 3.3, a time-domain spectroscopy experiment is depicted. As a table-top laser source, a commercial regenerative Ti:Sapphire femtosecond laser amplifier was utilized which provides 100 fs pulses with a pulse energy of 5 µJ at a center wavelength of 800 nm at a repetition rate of twice that of the TELBE THz sources. The laser system is synchronized to the accelerator using a commercial Synchrolock AP system from Coherent, Inc., which yields a timing jitter of 500 fs (RMS) (for details see Subsection 2.2.2). The laser beam is split into three beams: the first beam serves as the probe pulse in the CDR ATM, the second beam serves as the probe pulse in the undulator ATM, and the third beam is utilized as a probe laser pulse in the benchmark time-domain spectroscopy experiment.

As described in Section 2.3, both ATMs utilize the single-shot THz detection technique based on SD in the so-called near-crossed-polarizer detection geometry where a pair of almost

orthogonality aligned polarizing prisms are placed before and after the ZnTe crystal to increase the THz-induced modulation depth and to suppress the background [97].

The achievable temporal resolution of the ATM depends on the bandwidth and the chirp rate of the laser pulse, when the spectral resolution of the spectrometer is fixed. When the bandwidth and the initial laser pulse duration is fixed, a shorter chirped pulse duration (smaller chirped rate) leads to a higher temporal resolution of the ATM [86].

The chirped laser pulse duration for the CDR ATM is 10 ps (FWHM) which is achieved by a grating pair stretcher (See Figure 3.3). For the undulator ATM, the probe laser is chirped to 6 ps using two 15 cm long glass rods made from NSF-6 glass. There are two reasons for using a comparably short chirped probe pulse duration of 6 ps (FWHM) for SD of the undulator pulse (the whole undulator pulse duration is around 11 ps at 700 GHz). The first reason is that, owing to the multi-cycle structure of the undulator pulse (see Figures 3.3 and 3.4), ensuring that only a fraction of these cycles stays in the time window of the undulator ATM is sufficient for determining the arrival time. The second reason is that, as mentioned previously, a short probe pulse duration increases the temporal resolution of ATM. Therefore, a pulse duration of 6 ps can be regarded as a trade-off between high temporal resolution and sufficiently large time window of the undulator ATM. Please note that, in contrast to the negative chirp created by grating stretcher, the material dispersion induced by the glass rods results in positive chirp in the undulator ATM [96] and hence leads to an opposite sign of the wavelength-arrival time mapping compared to the CDR ATM [32]. The SD trace is recorded by a linear array camera [98] as in the case of the CDR ATM.

In the benchmark experiment, the undulator was tuned to 700 GHz at a repetition rate of 100 kHz. The laser was operated at repetition rate of 200 kHz, that is twice of that of the undulator, in order to use reference laser pulses for compensation of the laser pulse intensity fluctuations. A 2 mm ZnTe crystal was used for the EO sampling measurement.

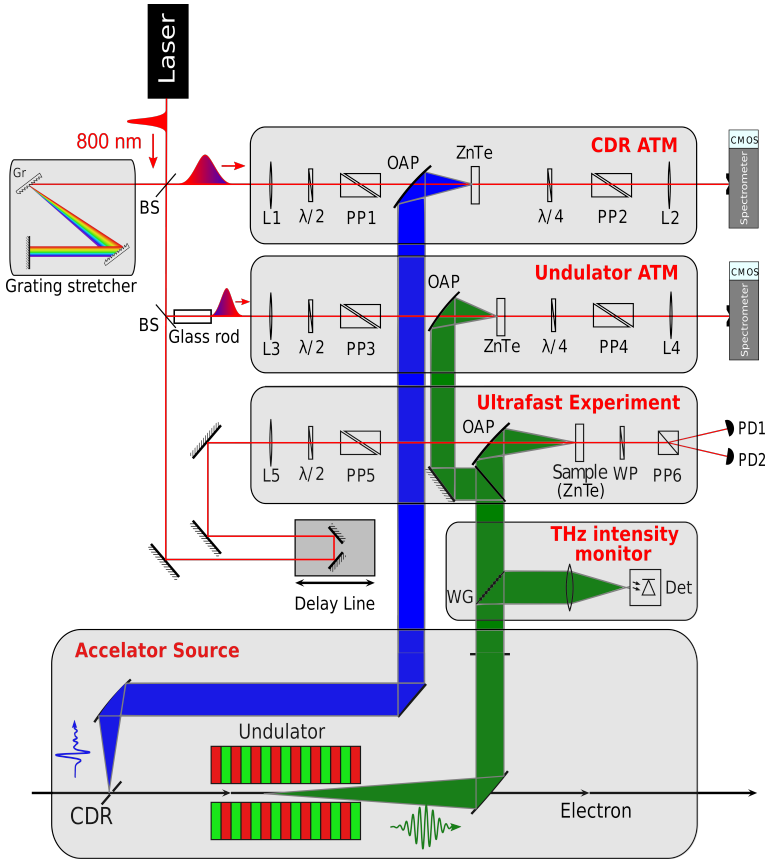

Figure 3.3: Experimental setup of the double-ATM scheme. The setup has been installed and tested at the TELBE THz facility. Two ATMs are employed: one detecting the CDR pulses and one detecting pulses from the undulator. An additional fast pyroelectric detector measures the intensities of each undulator pulse. The benchmark ultrafast experiment used to characterize the scheme was a time-domain spectroscopy experiment measuring the THz waveform emitted by the undulator source via EO sampling.

3.3 Analysis of the double-ATM data

In order to correct the arrival time between the laser and the undulator pulse, a data analysis procedure similar to the one used for the single CDR ATM scheme, as described in Subsection 2.2.4, is utilized.

The data analysis procedure consists of three steps. The first one is the most important one: determining the arrival time from the SD trace through pixel-to-time mapping. In contrast to the original CDR ATM, for the undulator ATM, the nonlinear second order material dispersion induced by the glass rod has to be taken into account. Another difference is that, because of the multi-cycle nature of the undulator pulse and the smaller recorded time window of the undulator ATM, the arrival time deduced from the CDR ATM needs to be used as additional information input to help determine the arrival time from the undulator ATM. Details about this protocol will be explained in the following paragraphs.

The second step is determining the undulator pulse intensity from the undulator SD trace. The third and the last step is the binning of the data. The employed protocol is equivalent to the one described in Subsection 2.2.4.2.

3.3.1 Arrival time determination

3.3.1.1 Linear pixel-to-time mapping

In the case of the CDR ATM, the detected THz waveform is of single cycle nature such that it contains one dominant global peak. This primary peak in the SD trace is chosen as a reference for determining the arrival time marked by P_1, as shown in Figure 3.4(a). This established procedure gives a comparably coarse value of the timing jitter relative to the probe laser and does not account for undulator-CDR-jitter.

For achieving this, the arrival time of the undulator has to be measured, as described before. However, in order to determine the arrival time marked by P_2 in the multi-peak SD trace (see Figure 3.4(b)) from the undulator ATM, the position of one particular peak corresponding to a particular THz field cycle has to be measured throughout the whole measurement. In order to assign a fixed cycle of the undulator pulse it is essential to consider the coarse jitter value from the CDR ATM in the process.

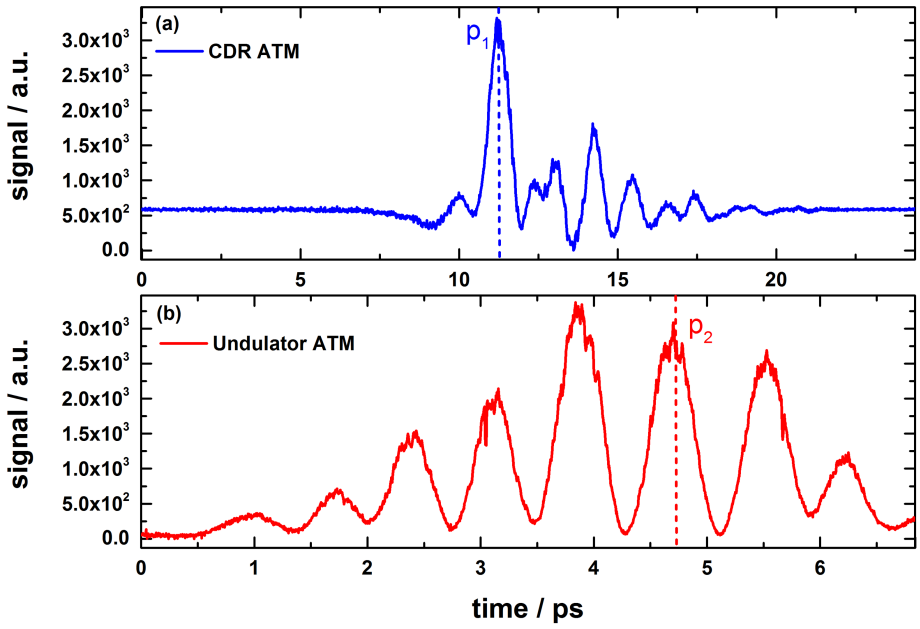

Figure 3.4: Typical SD traces measured by (a) CDR ATM and (b) undulator ATM. The SD trace of the undulator ATM was measured with the undulator tuned to 0.7 THz. Please note the different time windows for CDR and undulator ATM which are a consequence of the different chirp rates in each ATM.

This two-step *peak choosing* method can be described in detail as follows: First, for every THz pulse, the primary peak position is unambiguously determined by the CDR ATM. Since the amplitude of the primary peak is much higher than the rest of the signal, the primary peak position can be easily determined by choosing the peak with the highest amplitude, as shown in Figure 3.5(a). Then, this primary peak position is used to define the so-called *peak searching window* in the undulator SD. For example, the peak position P_{C1} deduced from the CDR ATM (see Figure 3.5(a)) is used to determine the corresponding peak searching window between P_{Low} and P_{High} (red filled area in Figure 3.5(b)) in the undulator SD trace of the undulator

ATM. Then, the locally constrained peak position P_{U1} inside this peak searching window, i.e., the red filled area, is chosen to determine the relative arrival time of the corresponding undulator pulse with respect to the probe laser pulse. Analogously, the relative undulator arrival time P_{U2} of shot 2, shown in blue, can be deduced after defining the shifted peak searching window from the shift of peak position P_{C2}.

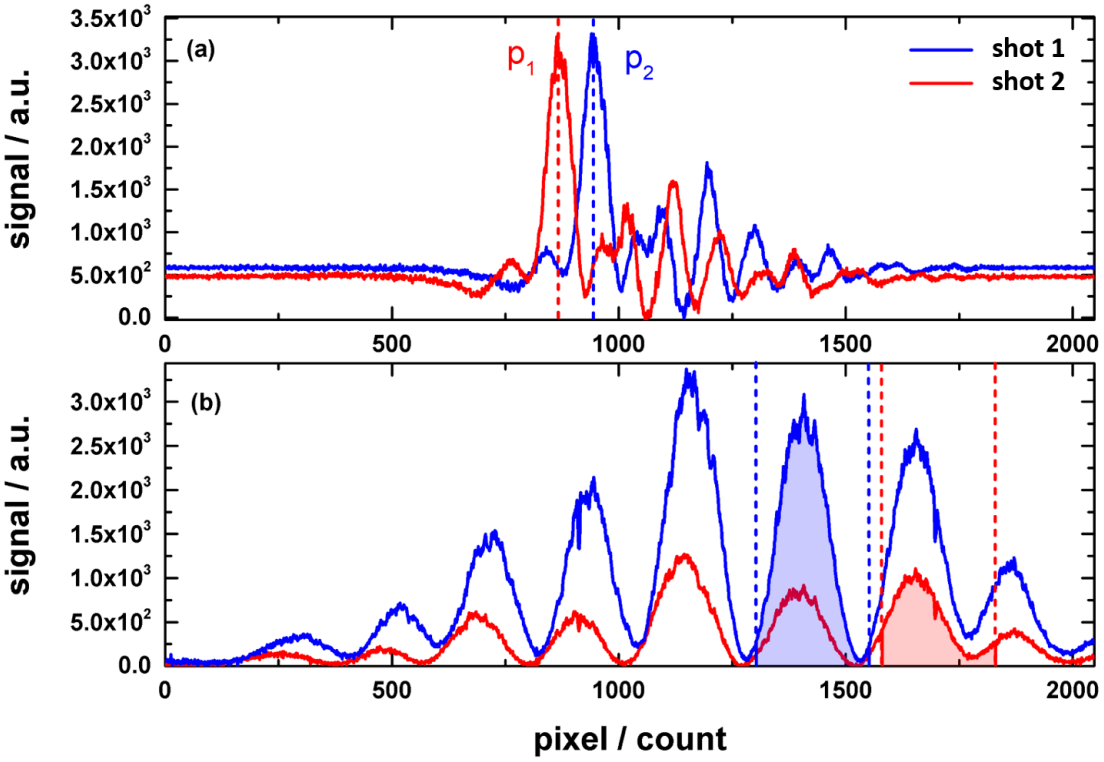

Figure 3.5: Arrival time determination from the SD trace measured by the undulator ATM. The colors blue and red refer to two randomly chosen shots. P_{Low} and P_{High} define the pixel positions of the edges of the peak searching window illustrated by the red shaded area. P_{U1} and P_{U2} are peak positions for the actual relative arrival time determination that correspond to the primary CDR ATM peak positions P_{C1} and P_{C2}, respectively.

In our particular case, the equation for determining the lower and the higher limit (P_{Low} and P_{High}) of the peak searching window are $P_{\mathrm{Low}} = -2.95 \cdot P_{\mathrm{C}} - 125$ px and $P_{\mathrm{High}} = P_{\mathrm{Low}} + 125$ px, where P_{C} denotes the primary peak position obtained from the CDR ATM. The factor of -2.95 refers to the ratio between the resolutions of CDR ATM ($\alpha_{\mathrm{C}} = 11.9\,\mathrm{fs/px}$) and undulator ATM ($\alpha_{\mathrm{U}}$ =4.03 fs/px) and the negative sign comes from the opposite chirp rates of the chirped laser pulses, due to the different types of stretchers. The value of 125 px refers to the FWHM width in pixel of one oscillation period of the undulator pulse, when the frequency of the undulator is tuned to 700 GHz. It is clearly visible that, if we are not tracking the peak searching window based on the primary peak position from the CDR ATM, it is not possible to ensure that always one particular peak, i.e. the same field oscillation cycle, is chosen throughout a measurement.

3.3.1.2 Nonlinear pixel-to-time mapping

As mentioned previously, the second order dispersion induced by the nonlinear dispersion in the NSF-6 glass, needs to be taken into consideration to establish the pixel-to-time mapping of the undulator arrival time.

If we only insert the measured first order pixel-to-time coefficient $\alpha_U = 4.03\,\mathrm{fs/px}$ into the pixel-to-time transformation equation: $\tau_U = \alpha_U \cdot P_U$ without considering the second order dispersion, the errors of arrival time correction will accumulate. A comparison between the linear and nonlinear pixel-to-time mapping is shown in Figure 3.6, where three continuous steps of the EO sampling measurement (one step of the delay stage denotes one sampling point with 0.67 ps time interval) are plotted after data binning. Please note, that the distribution of data points around the time axis for each step is a result of the residual jitter between accelerator and probe laser. The noise at the edges is due to the insufficient number of events in these time regions.

Figure 3.6(a) is generated as described in the following: First, within each step, the pixel number is converted into time by the above mentioned linear pixel-to-time mapping equation. From the graph, we can see clearly that these three steps do not overlap with each other perfectly. Especially, at the far ends of each step, the mismatch becomes more pronounced, as indicated by the green arrows in Figure 3.6(a). This mismatch, physically owing to the second order material dispersion of the glass rods that we used to chirp the laser pulse. The second order material dispersion leads to a nonlinear wavelength-arrival time mapping, i.e., the wavelength of the chirped pulse has the following form: $\lambda \propto At + Bt^2$. As a consequence, the arrival time must be corrected by involving a second order correction term, which can be deduced empirically by fitting the data.

The pixel-to-time transformation equation involving a second order correction term is: $\tau_\mathrm{U} = \alpha_\mathrm{U} \cdot P_\mathrm{U} - \beta_\mathrm{U} \cdot P_U^2$, where τ_U is the deduced arrival time, $\alpha_\mathrm{U} = 4.03$ fs/px is the linear transformation coefficient, β_U is the nonlinear transformation coefficient, and P_U is the peak position of the undulator SD trace. β_U turns out to be $\beta_\mathrm{U} = 4.15 \times 10^{-4}$ fs/px^2 after fitting. As illustrated in Figure 3.6(b), the mismatch at the edges of each step has been corrected and the procedure results in a precise overlap of all the steps.

Summing up, for the CDR ATM, the pixel-to-time transformation equation is $\tau_\mathrm{C}[\mathrm{fs}] = \alpha_\mathrm{C} \cdot P_\mathrm{C}[\mathrm{px}]$ in femtoseconds, where $\alpha_\mathrm{C} = 11.9$ fs/pixel. For the undulator ATM, the pixel to time transformation equation is $\tau_\mathrm{U}[\mathrm{fs}] = \alpha_\mathrm{U} \cdot P_\mathrm{U}[\mathrm{px}] - \beta_\mathrm{U} \cdot P_U^2[\mathrm{px}^2]$ in femtoseconds, where $\alpha_\mathrm{U} = 4.03$ fs/px and $\beta_\mathrm{U} = 4.15 \times 10^{-4}$ fs/px^2.

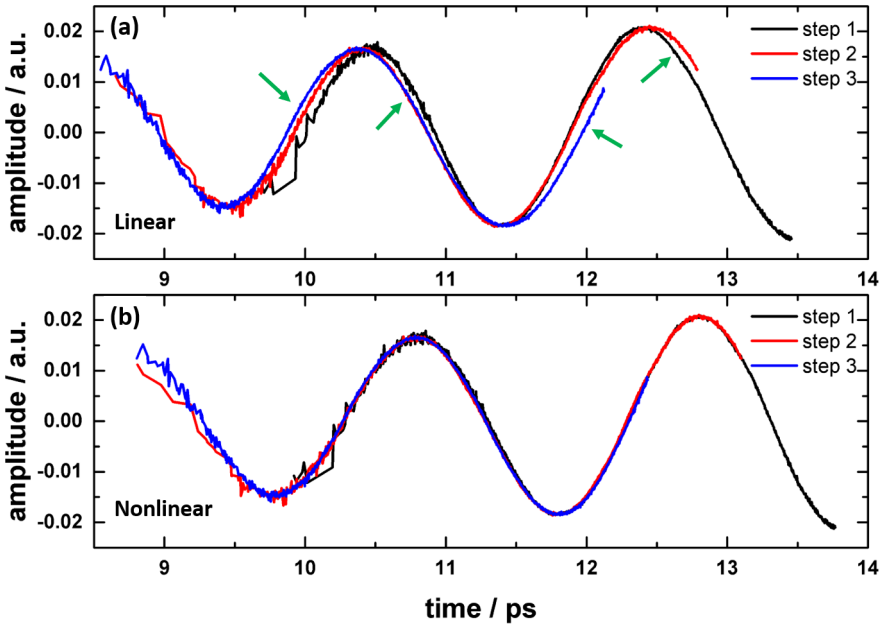

Figure 3.6: Comparison between arrival time determination ability of linear and nonlinear pixel-to-time transformation equations. (a) The result by applying the linear and (b) the nonlinear pixel-to-time transformation equation. The green arrows indicate the places where the retrieved traces show a strong mismatch between each other. (Retrieved traces from 3 continuous steps are shown as an example.)

After deducing the arrival time from the CDR ATM and double-ATM, a 2D histogram (see Figure 3.7) based on these two sets of data can be generated to show the correlation between the arrival time of the CDR and undulator pulse. The τ_C from the CDR ATM and the τ_U from the double-ATM show a quasi-linear relationship as expected because of the intrinsic synchronization relationship between them. Moreover, the only monotonous line in the 2D histogram indicates that during the arrival time determination process, always the correct peak from the multi-cycle pulse was identified and chosen.

In an ideal case, assuming no jitter exists between CDR and undulator, a sharp line should show up in the 2D histogram. The broadening of the line originates from the residual jitter between the CDR and undulator sources.

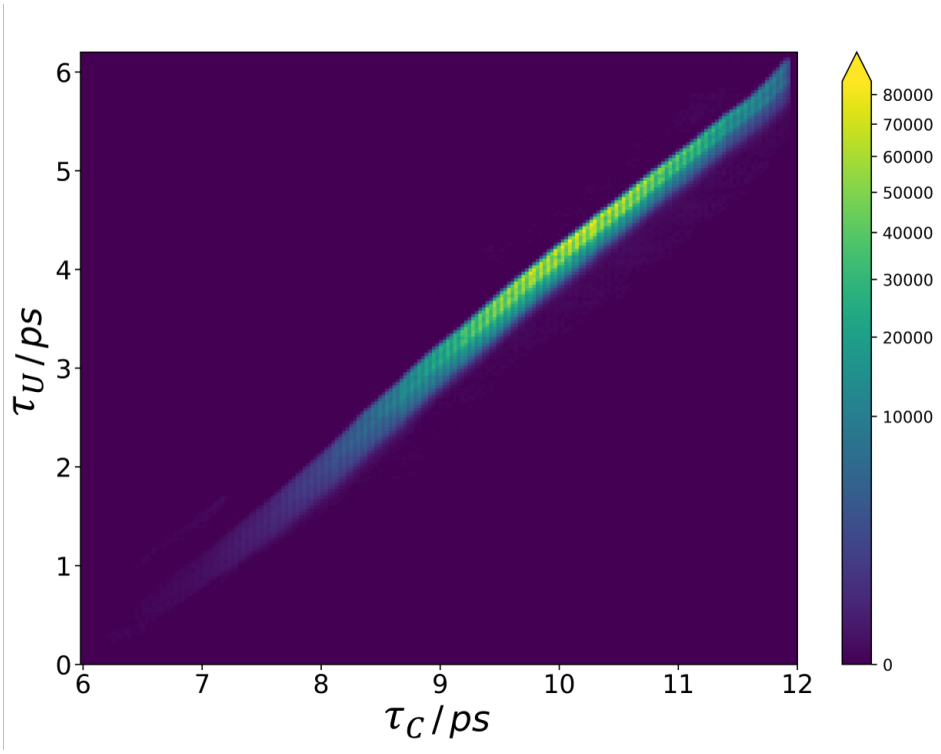

Figure 3.7: 2D histogram correlating the arrival times determined from CDR and double-ATM. The value on color bar means number of events.

3.3.2 Monitoring undulator pulse intensity with undulator ATM

At TELBE, a pyroelectric detector (developed and built at DESY [74]) that is capable to operate at a few hundred kilohertz repetition rate, is installed in the undulator beamline to monitor the THz pulse intensity fluctuations. As can be seen from Figure 3.3, a wire grid THz polarizer is added in the undulator pulse beamline allowing at least 99 % power transmission. The remaining 1 % power of the undulator pulse are reflected and focused onto the active area of the pyroelectric detector.

The undulator ATM developed within this thesis provides an alternative method to determine the undulator pulse intensity from the undulator SD trace. The method is based on the relationship $\Delta I(\omega) \propto |\widetilde{E}_{\mathrm{THz}}(\omega)|^2$, where $\Delta I(\omega)$ is the THz induced spectrum change of the chirped laser pulse, as described in Section 2.3. In this approach, the peak height of the selected peak in the SD trace can be regarded as proportional to the THz pulse intensity.

However, the direct readout of the peak height from the SD trace does not directly represent the undulator pulse intensity because of the inhomogeneous sensitivity function of the ATM system. Therefore, a data correction on the raw data (the direct readout of the peak height) is necessary to obtain the actual undulator pulse intensity from the SD trace.

The whole undulator pulse intensity correction procedure can be separated into two steps: (i) determining the sensitivity function and (ii) correcting the direct readout peak height with the sensitivity function. The sensitivity function of the ATM can be obtained by measuring the readout peak height at each pixel averaged over a large number of pulses: $\mathrm{S}(p) = \bar{I}_{\mathrm{read}}(p)$. Please note, the p in the bracket denotes that they are the function of pixel position. This assumption is valid in the case of a random distribution of the timing jitter. An example of a measured sensitivity function can be seen in Figure 3.8.

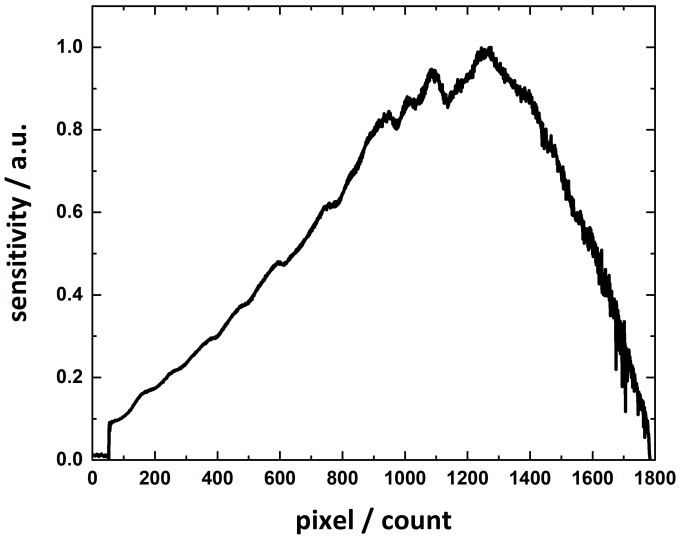

Figure 3.8: Sensitivity function S(p) of the undulator ATM. More than 2.9×10^7 pulses are used for determining the sensitivity function.

By substituting the sensitivity function S(p) into the following equation:

$$\mathrm{I_{cor}}(p) = \mathrm{I_{read}}(p)/\mathrm{S}(p), \tag{3.1}$$

where $\mathrm{I_{read}}(p)$ is the direct readout of the peak height from the SD trace and $\mathrm{I_{cor}}(p)$ is the corrected undulator pulse intensity.

In order to verify the result of the corrected undulator pulse intensity readout, a comparison is made between the histograms of the corrected undulator pulse intensity $\mathrm{I_{cor}}(p)$ obtained from the SD trace (see Figure 3.9(b)) and the undulator pulse intensity readout from the pyroelectric detector $\mathrm{I_{pyro}}$ (see Subsection Figure 3.9(c)). The readout of the pyroelectric detector can be regarded as a reference of the relative undulator pulse intensity (see Subsection 2.2.4.2).

It can be clearly seen by comparing Figure 3.9(a) and (c), before the correction, that the intensity distribution of the direct readout $\mathrm{I_{read}}(p)$ is very different from the one obtained from pyroelectric detector. However, after applying a correction using the sensitivity function S(p), the corrected undulator intensity distribution shows a higher distribution in the lower and higher energy regime, respectively, that is qualitatively similar to the one simultaneously measured by the pyroelectric detector (see Figure 3.9(b) and (c)). The double-peak distribution is reproduced in the histogram as well as the relative heights of the two peaks.

This finding of the qualitative resemblance between the intensity distributions of undulator ATM and pyroelectric intensity monitor clearly indicates the *potential* of the former to serve as pulse-resolved intensity monitor as well. This "free" additional function of the arrival time monitor could be developed further to detect the "absolute" intensity of the undulator pulse. However, further calibration procedures have to be implemented so that a measurement of the absolute pulse energies becomes possible..

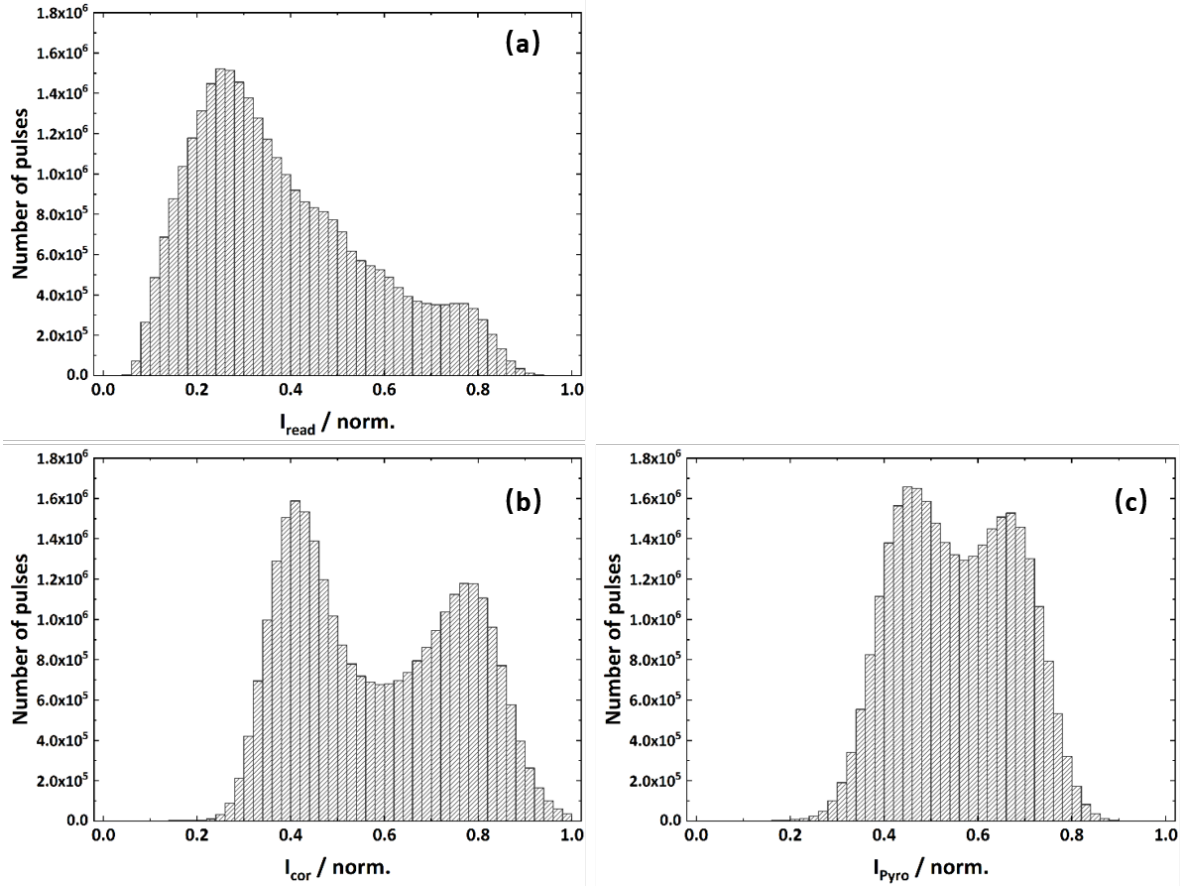

Figure 3.9: Comparison between undulator pulse intensity histograms measured by the pyroelectric detector and the undulator ATM. (a) Histogram of the undulator pulse intensity obtained from the direct readout of the peak heights from the undulator ATM. (b) Histogram of the *corrected* undulator pulse intensity obtained from the undulator ATM. (c) Histogram of the undulator pulse intensity obtained from the pyroelectric detector.

3.4 Results and discussion

3.4.1 Jitter and drift compensation

The aim of implementing the undulator ATM is to improve the temporal resolution of the ultrafast experiment, as the direct measurement of the timing of the undulator pulses enables higher timing accuracy in the *post mortem* data treatment. As a benchmark experiment to test this, a time-domain spectroscopy measurement of the THz waveform of the undulator pulse has been carried out. In the analysis, sequential EO sampling traces retrieved with arrival time correction derived from the CDR ATM and the double-ATM scheme are plotted for comparison in Figure 3.10(a) and (c), respectively. Here, each point represents *a single event*. As a figure of merit of the timing accuracy, we use the distribution width of raw, i.e., not binned, EO sampling data along the time axis. To minimize the effect of intensity fluctuations on the temporal EO sampling distribution, we characterized the EO sampling distribution along the time axis when the THz field is zero (black box in Figure 3.10(a,c)). The data point distribution linewidth around these zero-crossing positions is regarded as pulse-to-pulse temporal resolution, which was also used previously in Reference [99]. In practice, the standard deviation of data points at ten zero-crossing positions was evaluated, chosen symmetrically

around the strongest THz field cycle, which is presented in Figure 3.10(e). As the dash lines in Figure 3.10(e) show, the average of the standard deviations obtained from CDR and double-ATM are 55.75 fs (RMS) and 20.65 fs (RMS), respectively.

As expected, the double-ATM scheme improves timing precision significantly. The linewidth of the EO sampling trace at the zero-crossing positions drops from around 50 fs (RMS) to around 25 fs (RMS), compared to that of the single ATM scheme under the same accelerator conditions. Thereby precision is enhanced by a factor of nearly two. This increase can be attributed to both the higher temporal resolution of the undulator ATM and to the direct measurement of the timing, circumventing possible jitter between the CDR and undulator THz sources. These are the major advances compared to the CDR-only ATM monitor, with which the jitter between the CDR and undulator sources is not corrected. Please note that the temporal resolution determined from the linewidth distribution is an *upper limit* estimation of the timing jitter. The real timing jitter between the undulator and the laser pulse is smaller than the one obtained from the linewidth distribution, since the linewidth distribution also includes, for example, influence from undulator pulse intensity instabilities and detector noise.

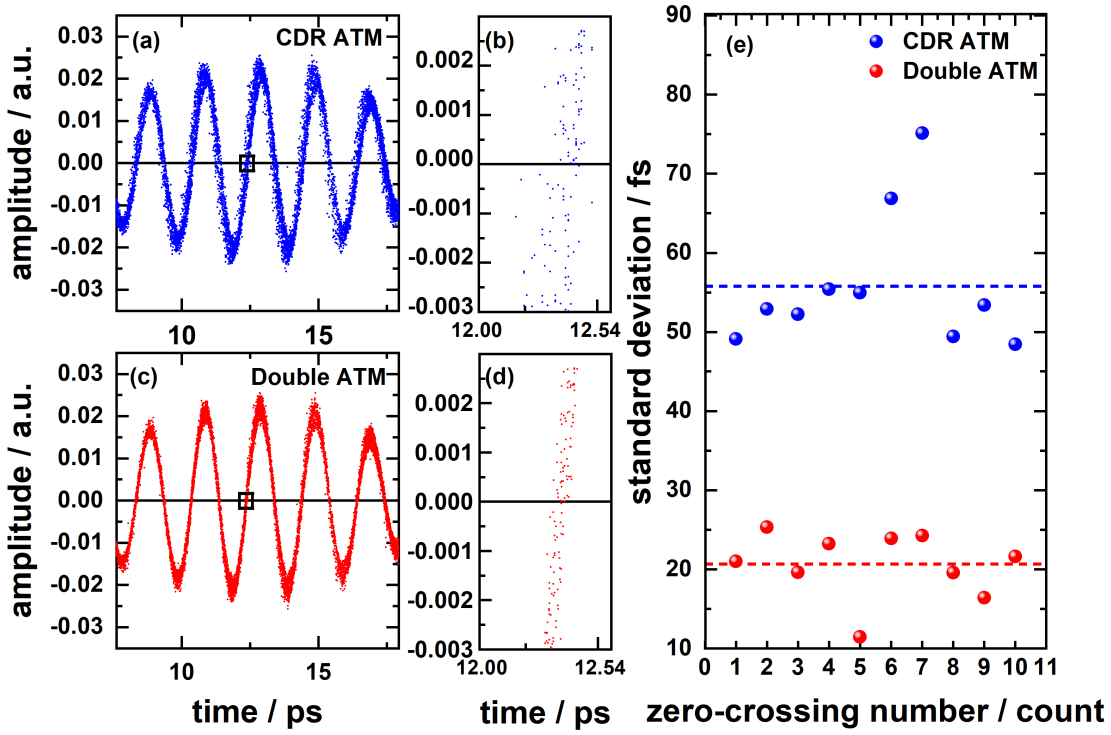

Figure 3.10: Benchmark experiment for the double-ATM scheme – short-term performance. (a) EO sampling trace of one loop measurement after data correction with timing signal from CDR ATM and (c) from double-ATM. (b) and (d) are enlarged views of one zero-crossing point, indicated by the corresponding rectangular area in (a) and (c), respectively. (e) Standard deviations of data points distribution around ten zero-crossing positions corrected by CDR ATM and double-ATM method. The blue and red dash lines in (e) represent the average value of the standard deviations of ten zero-crossings of CDR ATM and double-ATM method, respectively.

In order to study the long-term performance of the double-ATM, data binning was applied to average out the pulse-to-pulse jitter and intensity fluctuations. A set of ten EO sampling traces was measured with ten minutes time interval between measurements as shown in Figure 3.11. The long-term instabilities now can only stem from slow drifts, e.g. due to thermal drifts of the path length in the electron and photon transport beamlines.

As a measure of the drifts, we analyzed the position of the zero-crossings of the binned data. In Figure 3.11(b) and 3.11(d), the zoom for one set around zero-crossing at 11 ps (position of the black box shown in Figure 3.11(a) and 3.11(c)) is presented for single and double-ATM scheme, respectively. To estimate the drifts, we measured the RMS deviation of ten zero-crossings for each set, as shown in Figure 3.11(e). It can be seen that the drifts are significantly reduced when utilizing the double-ATM scheme. The timing precision of the double-ATM scheme was significantly improved over that of the single ATM scheme and can reach values well in the sub-10 fs regime down to 4 fs (RMS).

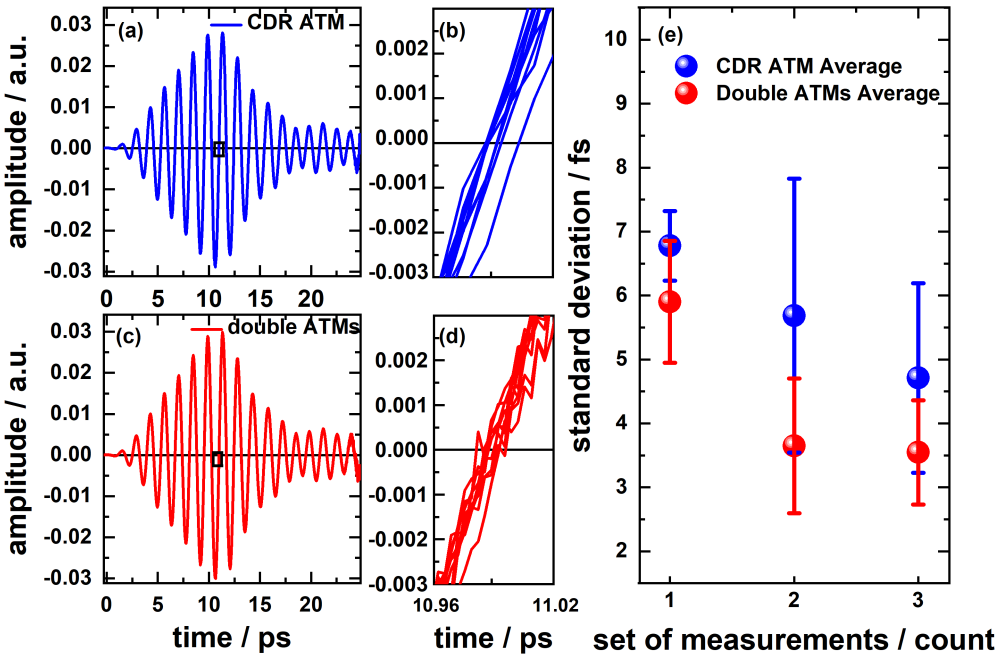

Figure 3.11: Benchmark experiment of the double-ATM scheme – long-term performance. (a) Ten binned EO sampling traces of measurement 1 using the single ATM timing signal. (b) Enlarged view of the black rectangular area in (a). (c) Ten binned EO sampling traces of measurement 1 using the double-ATM timing signal. (d) Enlarged view of the black rectangular area in (c). (e) Averaged standard deviation over ten zero-crossing positions of three set of measurements using the CDR ATM and double-ATM scheme. One set of measurement consists of ten traces. Error bars originate from the distribution of the standard deviations over ten zero-crossings of each measurement.

3.4.2 Correlation between arrival time and intensity instabilities

The full analysis of the simultaneously detected THz waveforms originating from the two independent superradiant THz emitters with femtosecond temporal resolution and high dynamic range open up interesting possibilities to study electron bunch dynamics within the accelerator.

In Figure 3.12, such an analysis is shown aiming at the question whether there is a systematic correlation between intensity fluctuations of the THz undulator source and the time delay between CDR and undulator pulses. Here, the same raw data is used as in Figures 3.10 and 3.11 to visualize the possible systematic correlation between the arrival time difference and the undulator pule intensity. The arrival time difference $\tau_C - \tau_U$ (τ_U: arrival time of the CDR pulses; τ_C: arrival time of the undulator pulses) and the corresponding undulator pulse intensity measured by the undulator ATM are plotted as the values of the X- and the Y-axis in Figure 3.12, respectively. The color of each data point indicates the number of events.

From Figure 3.12, we observe a strong and complex dependence between undulator arrival time (relative to CDR) and its intensity. This behavior may originate from slight electron bunch energy instabilities and spatial variations of the electron bunch trajectories.

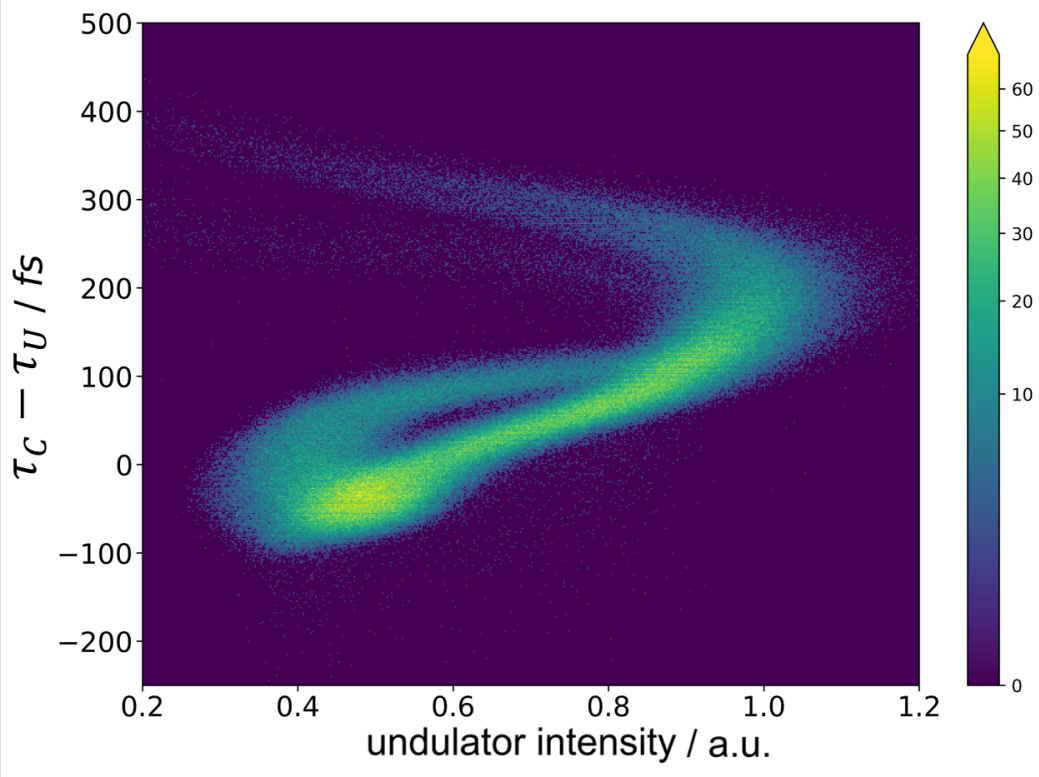

Figure 3.12: Correlation between arrival time difference (CDR to undulator pulse) and undulator pulse intensity. A substantial nontrivial dependency is observed. The color bar represents the number of events.

To understand these correlations further, we made use of the pulse-resolved intensity monitor to specifically evaluate correlations at different undulator THz intensity levels. We observed nontrivial correlations between undulator-CDR timing jitter and undulator pulse intensity. From Figure 3.13(a), pronounced drifts of this relative timing towards positive time delays with decreasing undulator pulse intensities is observed. From the zoom-in view shown in Figure 3.13(b) and (d), the undulator pulse intensity-correlated timing shift can be clearly seen.

By utilizing the double-ATM scheme this jitter level will be compensated to tens of fs and that timing jitter resolution of actual measurements will not be deteriorated by such instabilities (see Figure 3.13 (c)–(e)).

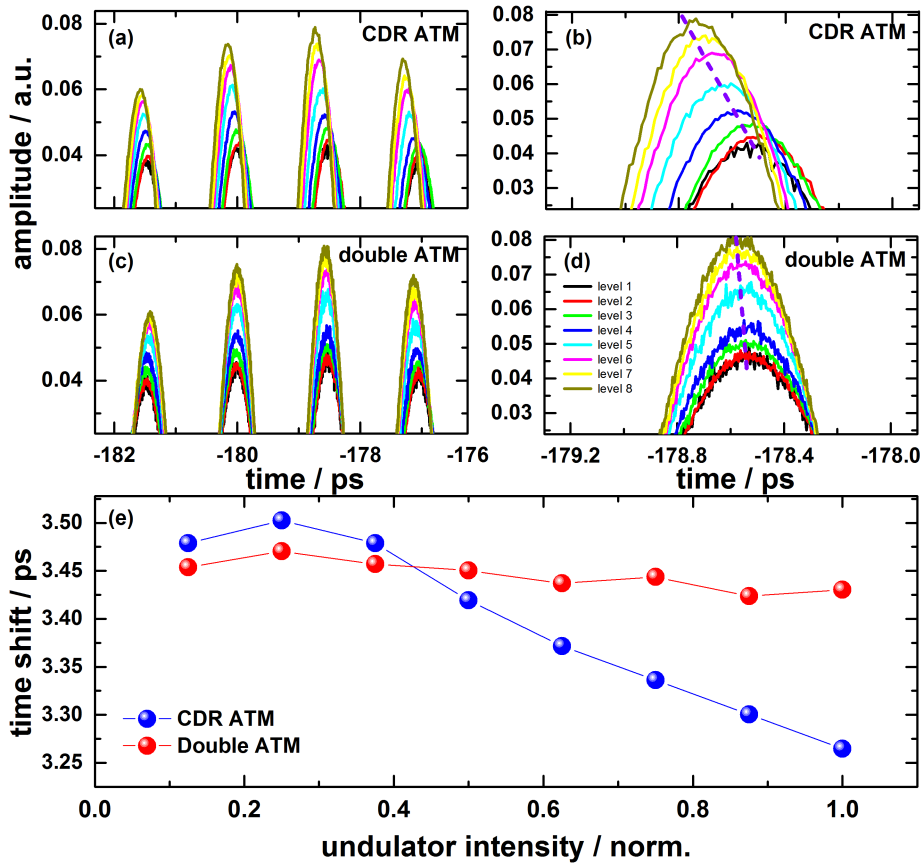

Figure 3.13: Benchmark experiment of the double-ATM scheme — compensation of long term drifts. (a) and (c) EO sampling traces sorted using either the single or double-ATM scheme, respectively. Both are binned with the same THz intensity classification (intensity binning in 8 selected ranges). (b) and (d) are an enlarged view of the strongest peak in (a) and (c), respectively. The purple dashed lines follow the peak position of each trace within a different THz intensity bin. (e) Dependence of the peak position in (b) and (d) on the undulator intensity.

Taking the analysis further, one can also look for systematic correlations between the spectral content and the intensity of the undulator radiation. As can be seen in Figure 3.14, the central frequency of the superradiant undulator pulses also shows a systematic dependence on pulse intensity. It shifts towards lower frequency by up to 6 GHz (0.9 % of its central frequency) upon decreasing intensity levels. Future studies that simulate the possible scenarios of such intensity/timing /frequency correlations, may provide a way to understand the origins of accelerator electron bunch instabilities.

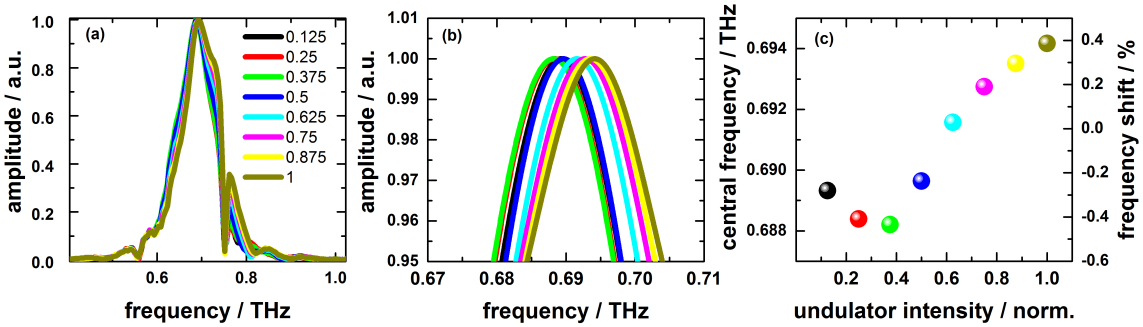

Figure 3.14: Benchmark experiment of double-ATM scheme – indication of electron energy drifts. (a) Normalized spectra derived from the EO sampling traces using the double-ATM scheme as timing signal, shown for different intensity levels. The value in the legend refers to the normalized undulator intensity level in Figure 3.13(e). (b) Enlarged view of the peak area. (c) Spectral peak positions at each undulator THz intensity level. The THz frequency drifts downwards by 6 GHz with decreasing intensity levels.

3.5 Conclusion and outlook

In this chapter, the newly developed double-ATM-based pulse- and field-resolved THz diagnostics technique is demonstrated. This upgrade of the routinely employed single-ATM-based pulse-resolved DAQ approach has proven its ability to improve the pulse to pulse temporal resolution from 50 fs (RMS) (achieved with single ATM) to up to 25 fs (RMS), and to reduce the temporal drift from 6 fs (RMS) to around 4 fs (RMS). In addition, the undulator ATM shows its potential to be used as intensity monitor. With these features, the new diagnostic technique also has the potential to help uncover multidimensional correlations between, e.g., the electron bunch energy and the arrival time, amplitude, and frequency of the radiation emitted by the electron bunch.

Further improvement of the temporal resolution of the undulator ATM could be achieved by using higher harmonics of the undulator pulse radiation since higher frequency components can imprint an even more finely resolved structure on the SD trace, and hence can increase the temporal resolution of the ATM further. Also, laser pulses with larger bandwidth and therefore shorter chirped pulse duration, as well as higher spectral density can improve the accuracy in determining the arrival time of the THz pulse from the SD trace.

4

THz-slicing method – proof-of-principle

4.1 Motivation

The pulse-resolved DAQ system has been successfully implemented at the TELBE facility in 2013 and is currently in routine user operation. This approach has proven itself as an efficient way to achieve high temporal resolution in the femtosecond regime and a high dynamic range in various types of pump-probe experiments, even if the initial timing and intensity are highly fluctuating. The upgrade of the pulse-resolved DAQ system to the double ATM scheme [96] as described in Chapter 3 improves the temporal resolution even further.

However, despite the numerous benefits of the pulse-resolved detection technique and the subsequent *post-mortem* data correction, this scheme has fundamental drawbacks.

Firstly, the timing information is read for each pulse by a linear array camera, which restricts the repetition rate, and therefore the experimental duty cycle, due to the limited bandwidth of the electronics available nowadays. Currently, the highest repetition rate of commercial Complementary Metal-Oxide-Semiconductor (CMOS) linear array detectors is up to 400 kHz [100], which is relatively slow when comparing to the repetition rate at modern FELs, e.g., up to 4.5 MHz at European XFEL, up to 1 MHz at the planned LCLS-II, and the high repetition rate mode of the TELBE facility of 13 MHz [62].

The second limitation is more fundamental: In envisioned, revolutionary experiments such as THz ARPES [101] or THz s-SNOM [102], additional steps in the data acquisition process, such as modulation and/or integration on the signal have to be implemented to increase the detection sensitivity due to the weak signals that are intrinsic to these techniques. As an example, similar to the operation principle of a Lock-in amplifier, in such experiments with low SNR, the pump pulses need to be modulated by a known reference signal. Then, the signal carried by the probe pulses needs to be *integrated* after signal demodulation via multiplying with the reference signal. However, under this scheme, the ATM-based pulse-resolved DAQ system cannot be applied, since the arrival time information is *lost during the signal integration.*

Therefore the experimental signal cannot be corrected *post mortem* using the real arrival time anymore. To overcome these limitations, an all-optical, passive synchronization method, namely the "THz-slicing" method was developed as part of this thesis. The theoretical description and a first proof-of-principle experiment for this approach are presented in this chapter.

4.2 The THz-slicing concept

The THz-slicing concept is inspired by the *femtoslicing* concept, which was proposed for the first time by Schoenlein et al. to generate femtosecond X-ray pulses from few 10 ps long electron bunches in storage rings [91], which otherwise exhibited characteristic pulse durations in the picosecond regime. As described in Section 2.5, in this technology, a femtosecond laser pulse propagates collinearly with a 30 ps-long electron bunch in a wiggler, resulting in energy modulation of a short portion of the electron bunch. After passing through a dispersive element, the modulated portion of the electron bunch (sliced electron bunch) can be separated transversely, and is then sent to a radiator, where a femtosecond long X-ray pulse is emitted. Thus, using two initially independent lightsources, a femtosecond X-ray pulse can be obtained using the slicing procedure. The femtosecond X-ray pulse generated by the sliced electron bunch is furthermore intrinsically synchronized to the femtosecond laser pulse because of the modulation principle.

The general idea of the slicing-based synchronization technique is shown in Figure 4.1. Two asynchronous pulses, one comparably long and one short pulse, from two independent lightsources can be synchronized by a slicing procedure. In the slicing procedure, only the portion of the long pulse that overlaps temporally with the short gate pulse can transmit through the *slicing* component. Hence, the transmitted portion (known as sliced pulse) is synchronized to the second gate pulse.

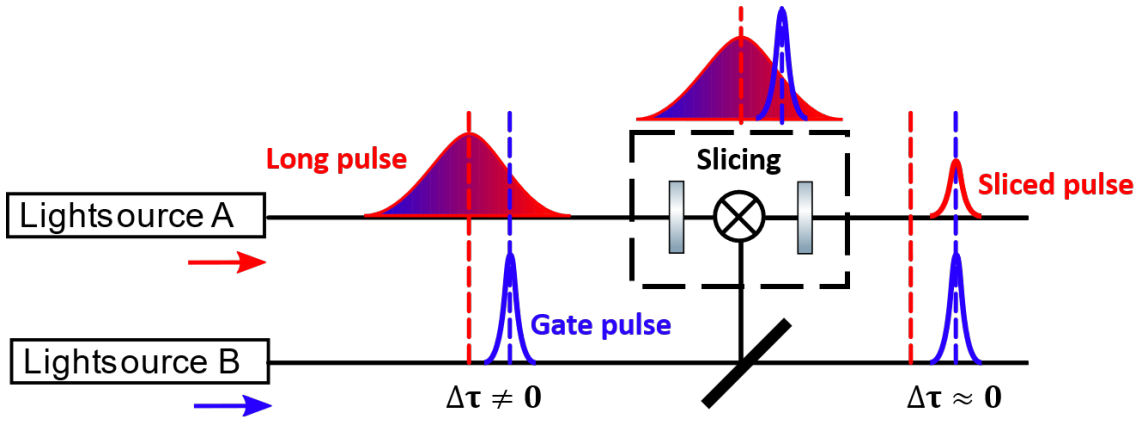

Figure 4.1: Schematic diagram of the slicing-based synchronization technology. Pulses from lightsources A and B are not synchronized at the beginning, exhibiting a nonzero jitter $\Delta\tau \neq 0$. Pulse A has a longer duration and is sent through an element that only allows the transmission of the portion of the pulse A that overlaps temporally with the short gate pulse B. The transmitted portion of the long pulse A is the so-called sliced pulse that is then synchronized with the gate pulse.

The THz-slicing process as developed within this thesis can be briefly described as follows: a comparably short THz gate pulse interacts with a sufficiently long laser pulse in an EO crystal and, as a consequence of the Pockels effect, it induces a polarization modulation of

the portion of the laser pulse that coincides with the significantly shorter THz pulses. By appropriate adjustment of optical polarization components that are placed in the path of the laser before and after the EO crystal, only the portion of the laser pulse (sliced pulse) that temporally overlaps with the THz pulse inside the EO crystal can propagate through. As a result, a sliced pulse is generated, which is intrinsically synchronized with the THz gate pulse.

Conveniently, the CDR pulse emitted from the TELBE facility has a quasi-single-cycle waveform that makes it directly applicable as a gate pulse for the THz-slicing method. As described in Section 2.2, because of the natural synchronization of CDR and undulator pulse, establishing the synchronization between the CDR source and the laser will also lead to the intrinsic synchronization of the undulator with the sliced laser pulse.

4.3 Theoretical description of the THz-slicing method

In this section the THz-slicing approach will be described in detail, including its theoretical foundations. THz-slicing in the current form is based on nonlinear optics, namely the Pockels effect in a nonlinear medium [103].

The experimental setup can be seen in Figure 4.2. The initially short 100 fs laser pulse from a Ti:sapphire laser is stretched by a grating pair to a few picoseconds through pulse chirping [1] and then sent to a ZnTe crystal collinearly with the THz gate pulse. A Half Waveplate (HWP) and a Glan-Taylor (GT) prism are placed before the ZnTe crystal to set the polarization state of the stretched pulse. Due to the Pockels effect inside the ZnTe crystal, the polarization state of the stretched pulse is modulated by the electric field of the THz gate pulse. After the ZnTe, one QWP is placed to compensate the residual birefringence of the ZnTe crystal, while another GT prism is set cross-polarized to the first GT prism. The function of the two cross-polarized GT prisms can be understood as a filter that to blocks transmission of the laser pulse without the present of the THz gate pulse and enables the transmission with the present of the THz gate pulse.

This configuration is used to achieve almost zero transmission without the THz gate pulse. By proper tuning of the polarization elements before and after the EO crystal, only the portion of the chirped pulse (known as sliced pulse) synchronized to the THz pulse is allowed to transmit through the optical system, i.e., without the gate pulse, no laser pulse can transmit through the optical system.

[1] Please note, pulse chirping is not the only way to stretch a short pulse, it can also be realized by applying a bandpass filter. In this thesis, since all the pulse stretching are realized through pulse chirping, therefore, the word “chirped pulse” is equivalent to the “stretched pulse” in this thesis.

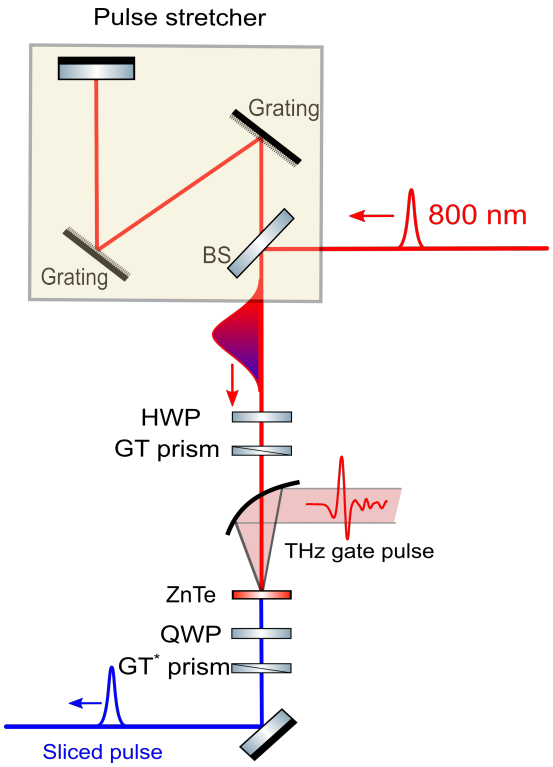

Figure 4.2: Schematic of the experimental realization of the THz-slicing concept. A laser pulse with 800 nm central wavelength is chirped by a grating-based pulse stretcher and then sent to the ZnTe crystal. An HWP is used to set the polarization state of the chirped pulse. A pair of near cross-polarized GT prisms put before and after the ZnTe crystal is used to allow the transmission of a certain portion of the chirped pulse that is modulated by the THz gate pulse. The QWP placed after the ZnTe crystal is used to compensate the intrinsic birefringence of the ZnTe crystal. The sliced pulse (blue) is intrinsically synchronized to the THz gate pulse.

The interaction between the chirped laser pulse and the THz pulse is based on the Pockels effect (described in Section 2.3). The THz electric field induces birefringence in an EO crystal, which is experienced by the laser pulse when overlapped in time and space. The electric field of the THz pulse can be considered as static because it oscillates much slower than the optical pulse. For the sake of simplicity, ideal phase matching between optical and THz pulse inside the EO crystal is assumed, since $n_{\mathrm{gr}}(\lambda_{\mathrm{probe}} = 812\,\mathrm{nm}) = n_{\mathrm{THz}}(\nu_{\mathrm{THz}} = 1.69\,\mathrm{THz}) = 3.22$ [104].

The induced second order nonlinear response in the medium is proportional to the electric field strength of the THz pulse, as given by the following equation [76]:

$$P_i^{(2)}(\omega) = 2\sum_{j,k} \epsilon_0 \chi_{ijk}^{(2)}(\omega, \omega, 0) E_{\mathrm{T},k}(0) E_{\mathrm{O},j}(\omega), \tag{4.1}$$

where $P_i^{(2)}(\omega)$ is the second order nonlinear term of the induced polarization, $\chi_{ijk}^{(2)}(\omega, \omega, 0)$ is the second-order nonlinear susceptibility tensor element of the ZnTe crystal, $E_{\mathrm{T},k}(0)$ and $E_{\mathrm{O},j}(\omega)$ are Fourier-domain representations of the THz pulse and the laser pulse, respectively, and (i, j, k) is the basis of coordinate system.

In many cases, the second order susceptibility tensor is symmetric in laser two indices, i.e., $\chi^{(2)}_{ijk}(\omega,\omega,0) = \chi^{(2)}_{ikj}(\omega,\omega,0)$, and therefor can be simplified to a d-matrix by applying the contracted notation:

$$d_{il} = \frac{1}{2}\chi^{(2)}_{ijk}, \tag{4.2}$$

where

$$\begin{array}{llllllll} l = & 1 & 2 & 3 & 4 & 5 & 6 \\ jk = & XX & YY & ZZ & YZ, ZY & XZ, ZX & XY, YX. \end{array} \tag{4.3}$$

Therefore, the vector of nonlinear polarization can be further described by Equation 4.4. Please note, d-matrix is the simplified representation of the nonlinear susceptibility applying the contracted notation:

$$\begin{pmatrix} P_X \\ P_Y \\ P_Z \end{pmatrix} = 4\epsilon_0 d_{14} \begin{pmatrix} 0 & 0 & 0 & 1 & 0 & 0 \\ 0 & 0 & 0 & 0 & 1 & 0 \\ 0 & 0 & 0 & 0 & 0 & 1 \end{pmatrix} \begin{pmatrix} E_{\mathrm{O},x}E_{\mathrm{T},x} \\ E_{\mathrm{O},y}E_{\mathrm{T},y} \\ E_{\mathrm{O},z}E_{\mathrm{T},z} \\ E_{\mathrm{O},y}E_{\mathrm{T},z} + E_{\mathrm{O},z}E_{\mathrm{T},y} \\ E_{\mathrm{O},z}E_{\mathrm{T},x} + E_{\mathrm{O},x}E_{\mathrm{T},z} \\ E_{\mathrm{O},x}E_{\mathrm{T},y} + E_{\mathrm{O},y}E_{\mathrm{T},x} \end{pmatrix}. \tag{4.4}$$

Please note, the d-matrix can be simplified to the remaining three nonvanishing independent elements $d_{14} = d_{25} = d_{36}$ since ZnTe belongs to the $\bar{4}3m$ crystal group.

For convenience, both lab coordinate system ($X'Y'Z'$) and crystal coordinate system (XYZ), where X, Y, Z are along crystallographic axes of the crystal, will be used.

The scheme in the lab coordinate system is shown in Figure 4.3, the optical and THz pulse are normally incident onto the (110) plane of the ZnTe crystal ($X' - Z'$ plane in the lab coordinate system). The Y'-axis is the beam propagation direction. Figure 4.4 demonstrates the geometrical configuration of both the optical and THz beam in the crystallographic coordinate system. Both $\boldsymbol{E}_{\mathrm{O}}$ and $\boldsymbol{E}_{\mathrm{T}}$ are in the (110) plane with its polarization angle θ and β respect to the Z-axis, respectively.

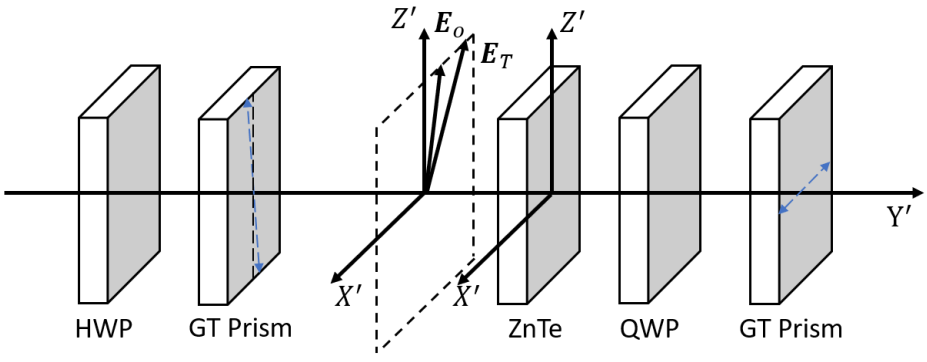

Figure 4.3: Lab coordinate system in the THz-slicing setup. The Y' direction is the propagation direction of the laser pulse. The X' and Z' are the horizontal and vertical directions, respectively. X'-Z' plane overlaps with the (110) plane of the ZnTe crystal. $\boldsymbol{E}_{\mathrm{T}}$ and $\boldsymbol{E}_{\mathrm{O}}$ represent the polarization directions of THz and laser pulse, respectively.

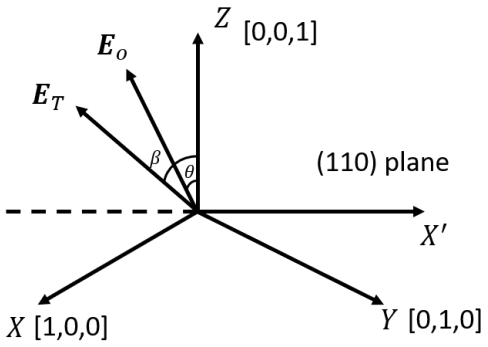

Figure 4.4: Geometry of the crystallographic coordinate system. Both $\boldsymbol{E}_{\mathrm{T}}$ and $\boldsymbol{E}_{\mathrm{O}}$ lie in the (110) plane. β and θ are angles measured with respect to the Z-axis.

The transformation relation between the lab coordinate system $X'Y'Z'$ and the crystallographic coordinate XYZ can be described by Equation 4.5 due to the (110) cut of the EO crystal. Please note, that the directions of the Z and Z' axes are the same.

$$\begin{bmatrix} X' \\ Y' \\ Z' \end{bmatrix} = \begin{bmatrix} -1/\sqrt{2} & 1/\sqrt{2} & 0 \\ -1/\sqrt{2} & -1/\sqrt{2} & 0 \\ 0 & 0 & 1 \end{bmatrix} \begin{bmatrix} X \\ Y \\ Z \end{bmatrix} \tag{4.5}$$

After applying this coordinate transformation, the relation of the nonlinear polarization between the lab and crystal coordinate system is obtained as given by Equation 4.6.

$$\begin{bmatrix} P_{X'} \\ P_{Y'} \\ P_{Z'} \end{bmatrix} = \begin{bmatrix} P_X - P_Y \\ -(P_X + P_Y) \\ P_Z \end{bmatrix} \tag{4.6}$$

As shown in Figure 4.4. The incident optical beam can be described by Equation 4.7 and the incident THz beam can be described by Equation 4.8 in the crystal coordinate system.

$$\mathbf{E}_{\mathrm{O}} = E_{\mathrm{O}}(\sin\theta/\sqrt{2}, -\sin\theta/\sqrt{2}, \cos\theta) \tag{4.7}$$

$$\mathbf{E}_{\mathrm{T}} = E_{\mathrm{T}}(\sin\beta/\sqrt{2}, -\sin\beta/\sqrt{2}, \cos\beta) \tag{4.8}$$

P_X, P_Y and P_Z can be obtained by substituting Equations 4.7 and 4.8 into Equation 4.4:

$$\begin{aligned} P_X &= -1/\sqrt{2} \cdot \sin(\theta+\beta) \cdot E_{\mathrm{O}} E_{\mathrm{T}} \cdot 4\epsilon_0 d_{14} \\ P_Y &= 1/\sqrt{2} \cdot \sin(\theta+\beta) \cdot E_{\mathrm{O}} E_{\mathrm{T}} \cdot 4\epsilon_0 d_{14} \\ P_Z &= -\sin\theta \sin\beta \cdot E_{\mathrm{O}} E_{\mathrm{T}} \cdot 4\epsilon_0 d_{14}. \end{aligned} \tag{4.9}$$

After applying the transformation matrix, the nonlinear polarization in the lab coordinate system can be obtained as:

$$\begin{aligned} P_{X'} &= -\sqrt{2} \cdot \sin(\theta+\beta) \cdot E_{\mathrm{O}} E_{\mathrm{T}} \cdot 4\epsilon_0 d_{14} \\ P_{Y'} &= 0 \\ P_{Z'} &= -\sin\theta \sin\beta \cdot E_{\mathrm{O}} E_{\mathrm{T}} \cdot 4\epsilon_0 d_{14}. \end{aligned} \tag{4.10}$$

It is clear that only $P_{X'}$ and $P_{Z'}$ are nonzero. As the nonlinear polarization $P_i^{(2)}(\omega)$ and the optical field have the same carrier frequency (see Equation 4.1), the nonlinear polarization can be considered as a source of electromagnetic waves interfering with the initial optical pulse that results in polarization rotation of the laser pulse under interaction with THz radiation.

After placing a GT prism after the ZnTe crystal with its transmission axis close to orthogonal with respect to the initial laser pulse polarization, only the THz-induced modulation of the laser pulse is transmitted, namely the sliced pulse.

The electric field of the sliced pulse is then proportional to the superposition of the leaked optical pulse and the nonlinear THz-induced term generated by the EO effect, as described by Equation 4.11 [81]:

$$\boldsymbol{E}_{\text{Sliced}}(t) \propto A \cdot \boldsymbol{E}_{\text{O}}(t) + \boldsymbol{E}_{\text{O}}(t)\boldsymbol{E}_{\text{T}}(t), \tag{4.11}$$

where coefficient A is the coefficient taking the relative magnitude and phase between chirped and sliced pulses into account. Term $A \cdot \boldsymbol{E}_{\text{O}}(t)$ denotes the transmitted leaking optical pulse, which is determined by uncompensated residual birefringence of the EO crystal and orientation offset of the GT prisms. Term $\boldsymbol{E}_{\text{O}}(t)\boldsymbol{E}_{\text{T}}(t)$ could be understood as the modulation term. Equation 4.11 shows that, the output sliced pulse can be understood as the *interference* between the leaking optical pulse and the polarization modulated by the THz field. The relative phase between $E_{\text{O}}(t)$ and $E_{\text{O}}(t)E_{\text{T}}(t)$ determines whether the interference is constructive or destructive. For example, if A has the same sign as the THz field, then the sliced pulse amplitude can be much higher with respect to the opposite case (A and THz fields have opposite signs).

Three methods can be used to control the relative phase between the THz induced modulation and the optical pulse. One is based on the polarity of the THz field variation. According to Equation 4.1, the phase can be controlled by EO crystal orientation. Another way to tune the relative phase between the terms is by changing the orientation offset of the GT prism transmission axis across the crossed-polarized configuration.

For example, by looking towards the X'-Z' plane along the $-Y'$ direction, the geometry of the polarization of different components can be seen in Figure 4.5. When the polarity of the THz electric field is negative: $E_{\text{T}} < 0$, E_{O} and $P_{X'}$ have the same phase according to Equation 4.10, since both of them have the same sign.

In one case, when the GT^* prism (the GT prism put after the EO crystal) is adjusted counterclockwise from the crossed polarization position by a small angle (marked as $GT^*(+)$), the component P_{X',GT^*} projected from $P_{X'}$ has a phase opposite to the component E_{O,GT^*} projected from E_{O} (see Figure 4.5(a)), which results in destructive interference. Please note, that the contribution from the $P_{Z'}$ will not be taken into account since the projection of $P_{Z'}$ on $GT^*(+)$-axis is too small compared to the contribution of $P_{X'}$. In another case, as shown in Figure 4.5(b), when the GT^* prism is turned clockwise from the crossed polarization position with a small angle (marked as $GT^*(-)$), P_{X',GT^*} and E_{O,GT^*} have same phases relative to each other and results in constructive interference.

The contribution of the GT^* prism can be illustrated by the value change of the coefficient A in Equation 4.11. In case of negative THz electric field when GT^* is tuned to $GT^*(+)$, the sign of A is also negative. Oppositely, when GT^* is tuned to $GT^*(-)$, A will have a

positive sign. Therefore, by tuning the transmission angle of the GT prisms, switching between constructive or destructive interference is possible (assuming the polarity of the THz electric field is fixed).

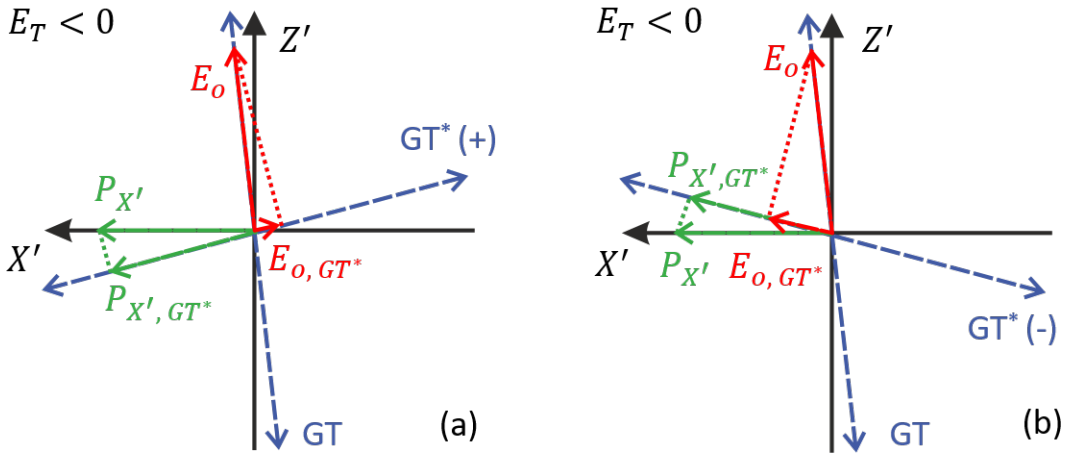

Figure 4.5: Schematic of the GT prism orientation-induced phase change. GT and GT^* denote the orientation direction of the GT prisms placed before and after the EO crystal, respectively. P_{X',GT^*} and E_{O,GT^*} are the projections of $P_{X'}$ and E_O on the GT^*-axis, respectively. (a) The scheme when GT^* is tuned counterclockwise with a small angle. (b) Another scheme when GT^* is tuned clockwise with a small angle.

Depending on the polarity of the E_{T}, constructive or destructive interference between the leaking optical pulse and the modulated term can be induced under different GT prism orientations, as it is shown in Table 4.1. As a result, the sliced pulse duration, shape and spectrum will depend on whether constructive or destructive interference has occurred.

Table 4.1: Type of interference induced by the THz-slicing. Depending on the polarity of the E_{T}, constructive or destructive interference between the leaking optical pulse and the modulated term can be induced under different GT prism orientations.

	$E_{\mathrm{T}} < 0$	$E_{\mathrm{T}} > 0$
$GT^*(-)$	constructive	destructive
$GT^*(+)$	destructive	constructive

Since the sliced pulse is used as a probe pulse for the ultrafast pump-probe experiment, its pulse duration is governing the achievable high frequency cutoff of the detection system. One example for this is THz-TDS. As Figure 2.21 in Section 2.3 shows, the cutoff frequency of EO sampling for a probe pulse with 100 fs duration is around 5 THz (when an appropriate EO crystal is used). For a probe pulse duration of 500 fs, the cutoff frequency is reduced to only around 1 THz.

As the sliced pulse duration determines the highest cut-off frequency of the EO sampling detection, by changing the (i) THz polarity, (ii) EO crystal orientation, and (iii) GT prism orientation, the sliced pulse duration can be compressed.

4.4 Proof-of-principle experiment

4.4.1 Experimental setup

Beamtime at TELBE is in very high demand. Hence before implementing the THz-slicing technique in a real-world experiment at TELBE, a demonstration experiment based on a table-top THz source has been performed to verify the feasibility and the potential of this approach. A benchmark table-top setup has been built to demonstrate the intrinsic synchronization between the accelerator-based THz source and an external laser system based on the THz-slicing concept. The experimental scheme is illustrated in Figure 4.6. Laser A and laser B provide two synchronized pulses with an 800 nm central wavelength, 100 fs pulse duration, 1 kHz repetition rate, with 1.3 mJ and 300 nJ pulse energies, respectively. Please note, Laser A and Laser B are seeded by the same oscillator with a jitter level smaller than 50 fs (RMS).

The pulses in laser line B are linearly chirped by a grating pair to around 10 ps (see red curve in Figure 4.9) and then redirected to the EO crystal for THz-slicing. The pulses in laser line A are sent into delay A, which is used to *emulate* jitter by adding an additional freely variable time delay between laser line A and laser line B. Thereafter the pulses from laser line A are split into two arms: pulses in one arm (1.2 mJ) are used to generate quasi-single-cycle THz gate pulses via optical rectification by focusing the laser onto a 2 mm thick (110) ZnTe crystal. Pulses in the second arm (10 µJ, illustrated as a green line in Figure 4.6) are used as a reference for the sliced pulse characterization. Please note, the 10 µJ pulse energy is measured after being dimmed by the neutral density filters.

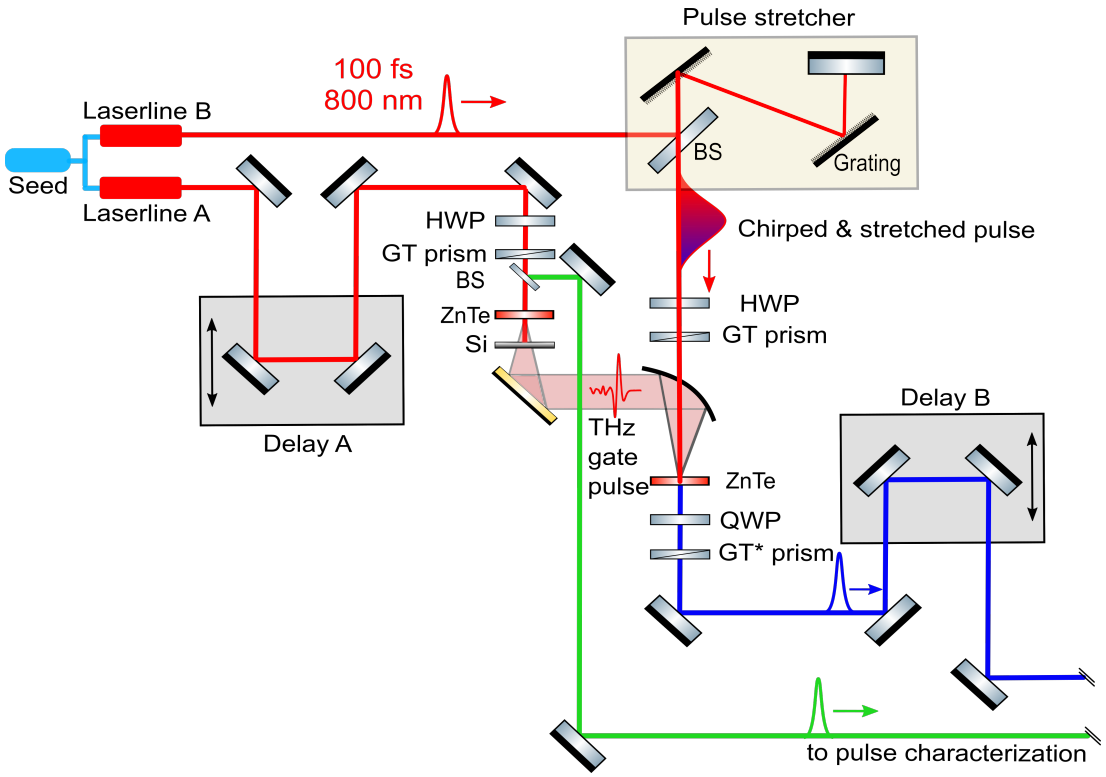

Figure 4.6: Experimental setup of the proof-of-principle experiment of THz-slicing technology. Laser A and Laser B are seeded from the same oscillator. Delay A is used to emulate jitter between laser from laser line A and laser line B. THz-slicing is induced in a ZnTe crystal by the interaction between the chirped and the THz pulse. The sliced pulse (blue line) and the reference pulse (green line) are sent to the pulse characterization section, as shown in Figure 4.8.

The chirped and stretched pulses from laser line B interact with the THz gate pulses generated by laser A in the ZnTe crystal placed in between two nearly cross-polarized GT prisms, as described in detail in Section 4.3. The HWP placed before the first GT prism is used to adjust the amplitude of the transmitted optical pulse via changing the polarization state of the optical pulse. The QWP placed after the ZnTe crystal is utilized to compensate the residual birefringence of the ZnTe. Otherwise, the residual birefringence of the ZnTe can reduce the modulation depth significantly and leads to a reduction in slicing efficiency.

The initial laser pulse energy in laser line B is about 300 nJ. After the THz-slicing process, the sliced pulse energy was measured to be about 0.096 nJ. Without THz gate pulse, the optical leakage was around 0.06 nJ. Taking into account the duration of the chirped laser and THz gate pulses, the efficiency for the pulse slicing is estimated to be around 6×10^{-3} (the efficiency here is derived as the ratio between *peak* powers of sliced pulse and initial chirped pulse).

Since the THz gate pulse energy is too small to be measured through a normal pyroelectric power meter, the THz pulse energy in the experiment was estimated according to Ref. [105]. The laser-based THz gate pulse energy is assumed to be on the order of 10 nJ. The electric field strength of the THz gate pulse is estimated to be on the order of 10 kV/cm. The waveform and the spectrum of the THz gate pulse is shown in Figure 4.7.

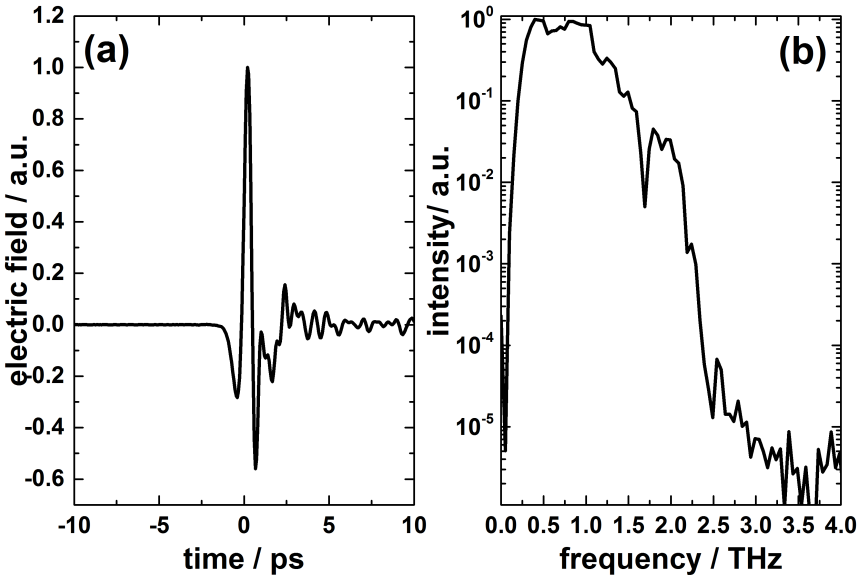

Figure 4.7: Electric field waveform and spectrum of the THz gate pulse. (a) Waveform of the THz gate pulse measured by EO sampling. (b) Derived spectrum of the THz gate pulse via Fourier transformation of (a).

After the THz-slicing process, the sliced pulse is sent to the pulse characterization module for a comprehensive analysis of the THz-slicing process. As can be seen in Figure 4.8, a cross-correlator and a spectrometer are utilized to characterize the sliced pulse's duration and its spectrum. Additionally, a THz-TDS setup (Fig. 4.8(c)) is available which uses the sliced pulse as probe and an additional THz pulse generated from the reference pulse as the pump pulse in order to characterize the jitter compensation ability of the THz-slicing process. In combination, these pulse characterization techniques yield all the information necessary to benchmark the THz-slicing process.

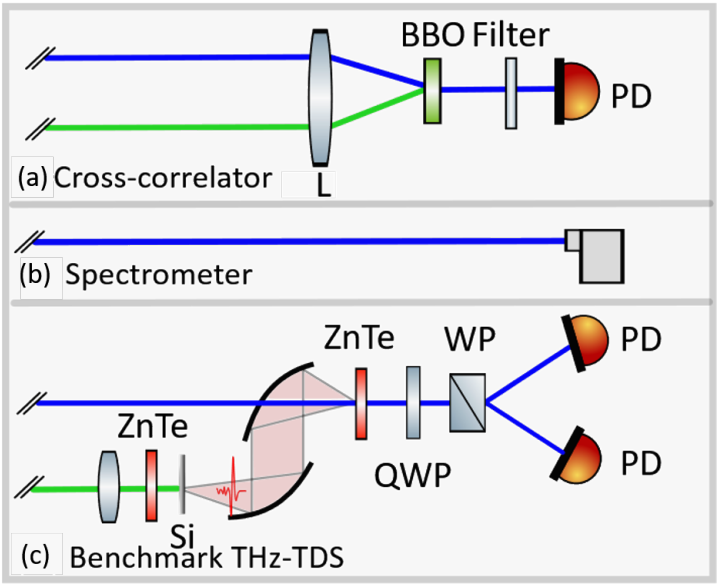

Figure 4.8: Sliced pulse characterization methods. Three methods are used to characterize the sliced pulse. (a) A cross-correlator is used to characterize the pulse duration of the sliced pulse via measuring the Second Harmonic Generation (SHG) signal of the sliced pulse and the reference pulse. (b) The spectrum of the sliced pulse is measured by a spectrometer. (c) A conventional THz-TDS system is used to characterize the jitter compensation ability by measuring the waveform of the THz pulse through EO sampling (sliced pulse is used as probe pulse in the EO sampling detection scheme).

4.5 Results and discussion

4.5.1 Sliced pulse duration

In order to give a direct impression of the ratio between the pulse durations of the chirped pulse and the THz gate pulse, a comparison of both pulses is shown in Figure 4.9.

As explained in Section 4.3, the offset of the cross-polarized GT prisms can be used to control the sliced pulse duration via changing the type of interference between the leaking optical pulse and the modulated term (the second term in Equation 4.11). A set of temporal profiles of the sliced pulses measured via cross-correlation under various positive and negative GT^* orientation angles are shown in Figure 4.10. It can be clearly seen that compared to the situation under negative GT^* orientations (see Figure 4.10(b)), the side lobe peaks next to the primary peak are strongly suppressed under positive GT^* orientations (see Figure 4.10(a)). This is because of the different types of interference induced by the polarity of the THz field and the GT prism orientation, as it was demonstrated in Table 4.1 in Section 4.3.

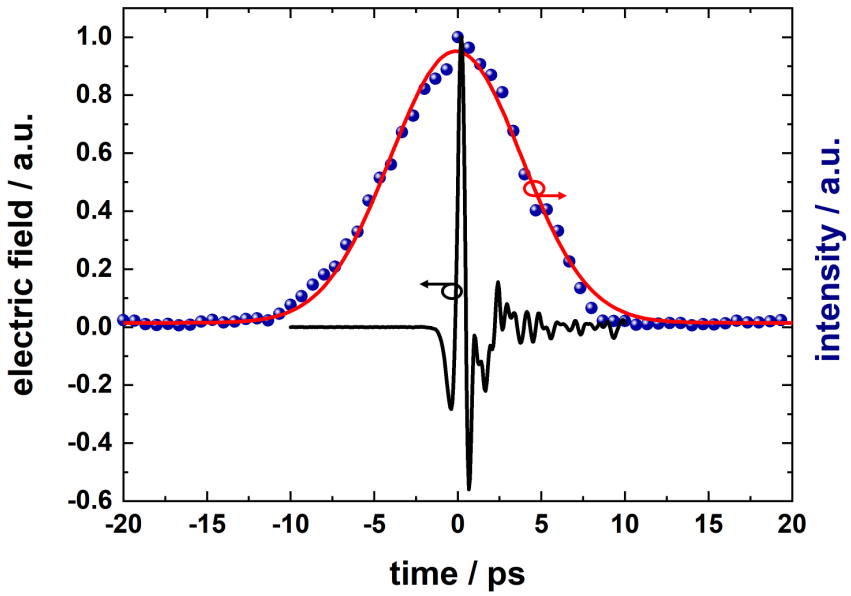

Figure 4.9: Comparison between the duration of the THz gate pulse and the chirped laser pulse. Blue circles are as-measured data points from the cross-correlator (see Figure 4.8). The red curve represents a Gaussian fit.

The existence of the side lobe peak increases the pulse duration of the sliced pulse, and therefore needs to compressed as much as possible through the GT^* orientation. Please note, the reason why the primary peak always exists regardless of the GT^* orientation direction is that the term $A \cdot \boldsymbol{E}_o(t)$ dominates term $\boldsymbol{E}_o(t)\boldsymbol{E}_T(t)$ when parameter A is tuned to an appropriate value by the GT^* prism.

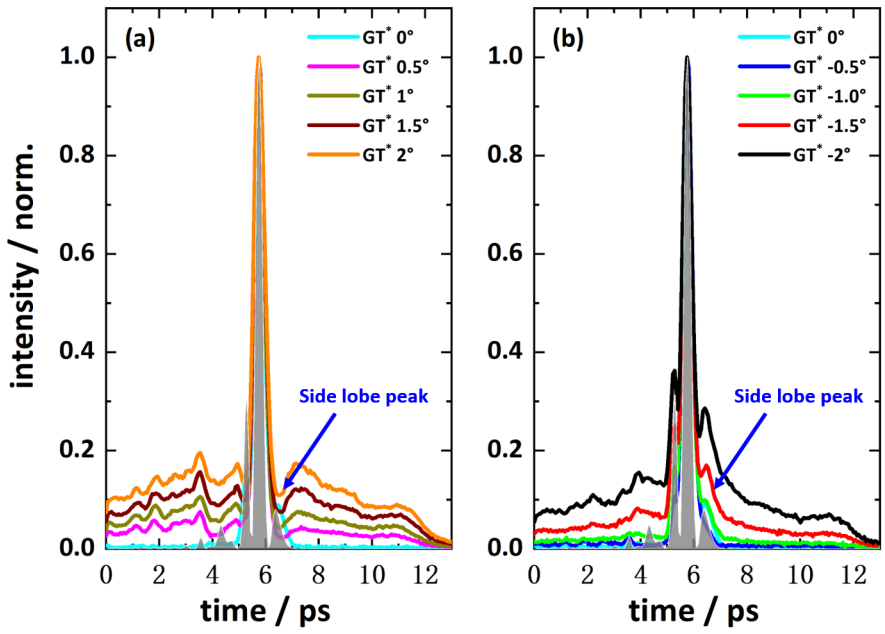

Figure 4.10: Comparison between the cross-correlation signal of the sliced pulse measured under opposite GT^* orientation. The gray-shaded area is the intensity profile of the THz-gate pulse. The red "+" and "-" signs represent the polarity of the electric field of the THz gate pulse. (a) Temporal profiles of the sliced pulse under various positive GT^* orientations, and (b) another set of measurements under negative orientations.

The relationship between the GT^* orientation and the side lobe peak height is shown in Figure 4.11. It can be clear seen that, the minimal sliced pulse duration could be reached under a small GT^* orientation offset, e.g., 0.5° and -0.5°.

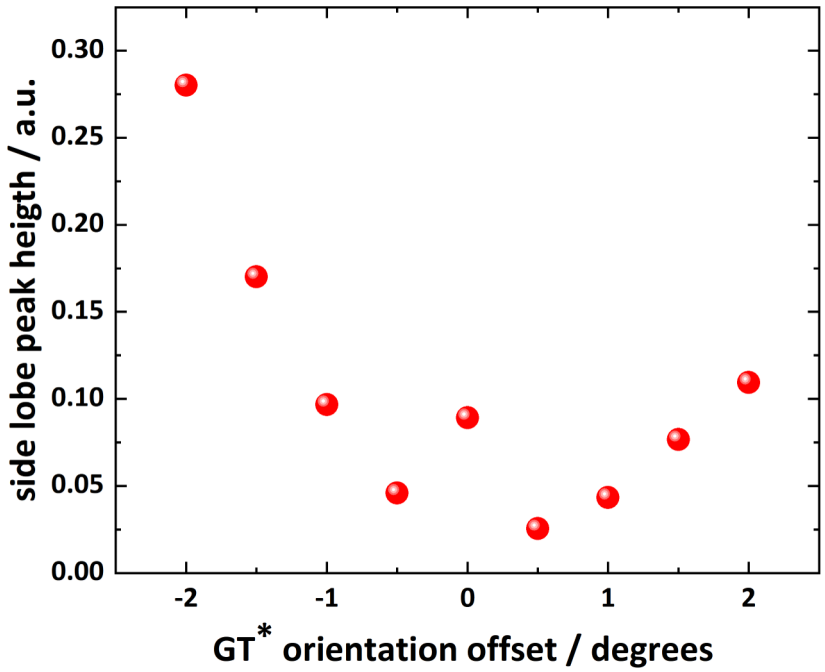

Figure 4.11: Dependence between the side lobe peak height and the GT^* orientation.

After applying a Gaussian fit on the cross-correlation signal of the sliced pulse measured under 0.5° GT^* orientation, the minimal sliced pulse duration of 183 fs (RMS) can be obtained (see Figure 4.12).

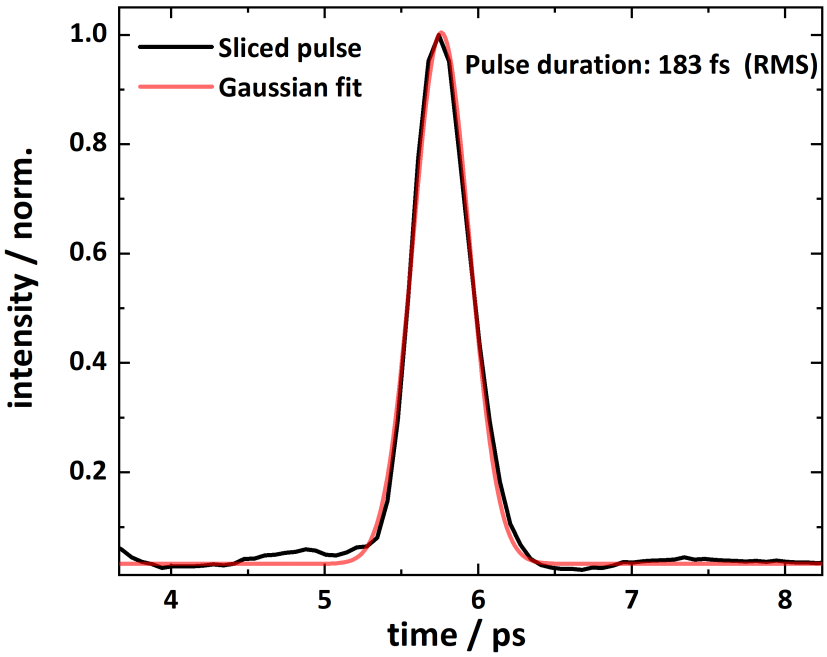

Figure 4.12: Gaussian fit of the cross-correlation signal of the sliced pulse. The black curve is the cross-correlation signal of the sliced pulse obtained when the GT^* orientation is tuned to 0.5°. The red curve is the Gaussian fit of the cross-correlation signal.

Please note that the minimum pulse duration is determined by two main factors: (i) the pulse duration of the THz gate pulse and (ii) the phase matching condition between the THz and the optical pulse within the EO crystal. To achieve shortest sliced pulses, the duration of the THz gate pulse needs to be the shortest.

4.5.2 Sliced pulse spectrum

Besides the sliced pulse duration, the spectrum of the sliced pulses under various GT^* orientations are also measured. There are two reasons why the spectrum needs to be characterized. The first one is that the theory of THz-slicing can be verified by comparing the simulation results with the measured spectrums.

Figure 4.13 shows a set of measurements including the cross-correlation result and its corresponding spectrum when GT^* is tuned to various positive angles from 0° to 1.5°. Similarly, the same set of results when GT^* is rotated by different negative angles is given in Figure 4.14.

It can be clearly seen that the spectrum of the sliced pulse under a positive GT^* tuning angle exhibits multiple peaks. Conversely, the spectrum under negative angles tends to have a shape with two primary peaks, as illustrated in Figure 4.14(e,f,h). This special feature could help in verifying the applicability of the theory discussed in Section 4.3 and also could be used as a the rule of thumb in determining the GT^* orientation.

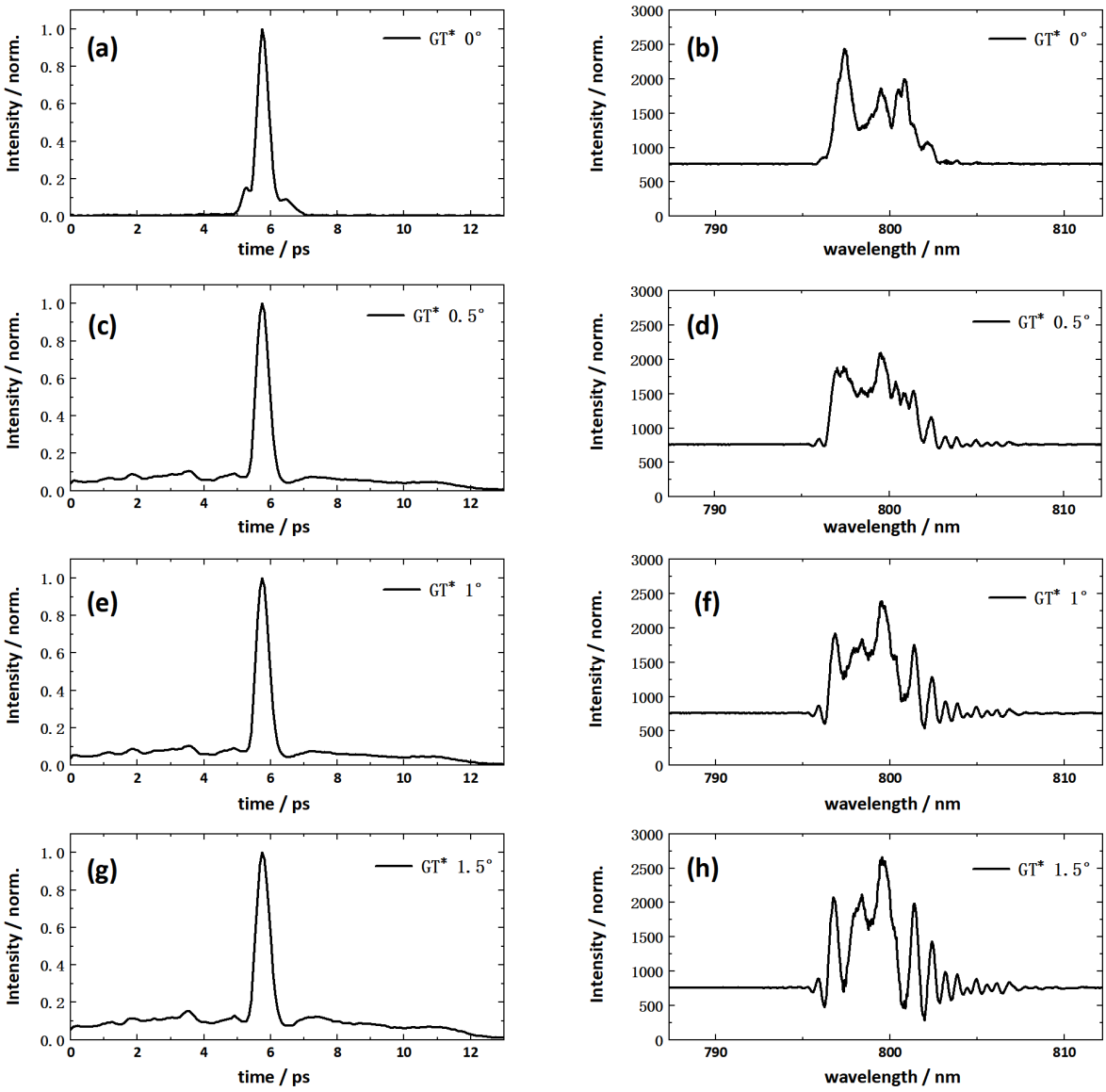

Figure 4.13: Sliced pulse characterization when GT^* is tuned clockwise from the crossed polarization position. (a), (c), (e), (g) are results of the cross-correlation measurement of the sliced pulse when GT^* is tuned to 0°, 0.5°, 1° and 1.5°. (b), (d), (f), (h) are the corresponding spectra measured by the spectrometer.

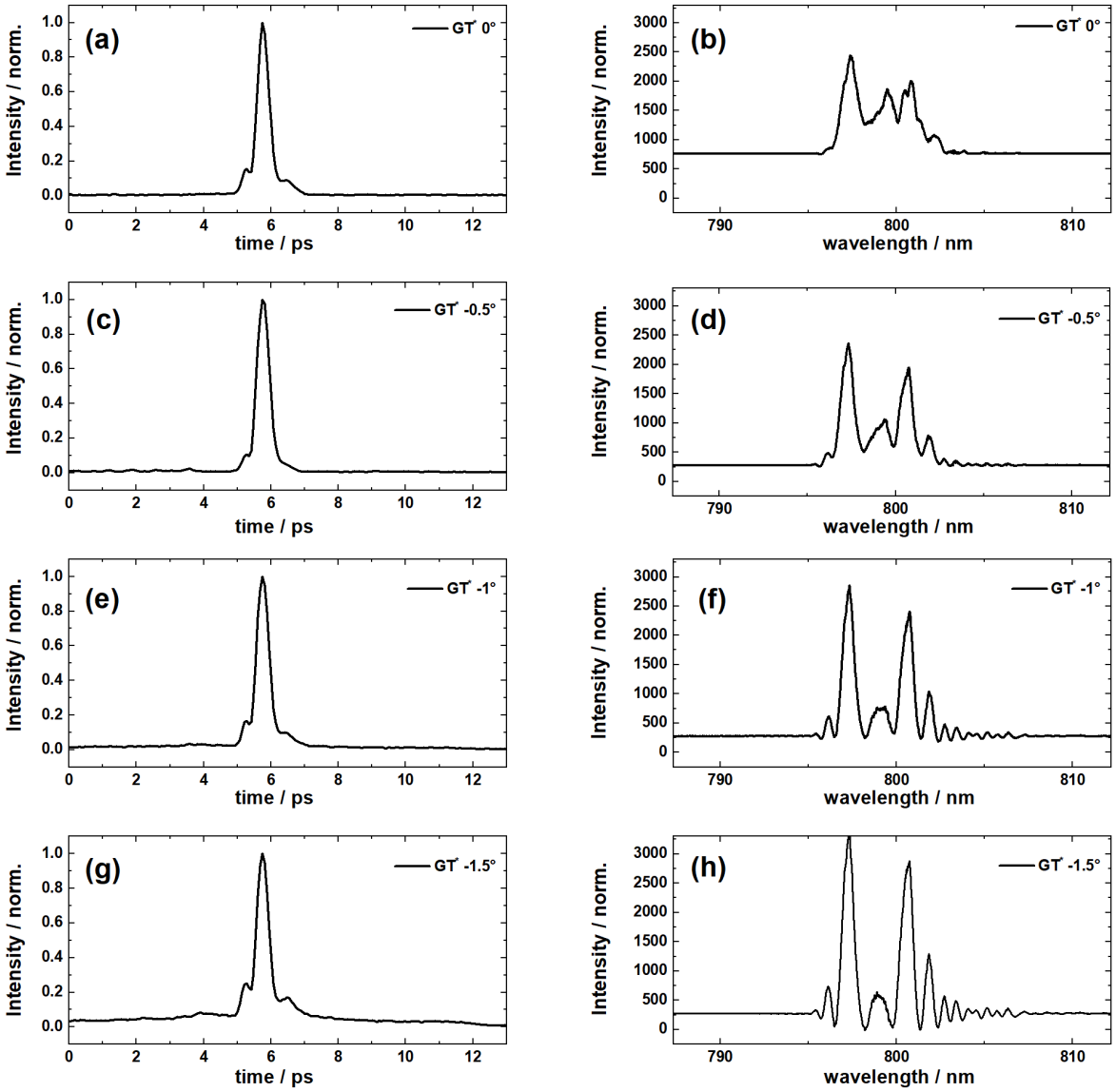

Figure 4.14: Sliced pulse characterization when GT^* is tuned anticlockwise. (a), (c), (e), (g) are results of the cross-correlation measurement of the sliced pulse when GT^* is tuned to 0, -0.5, -1 and -1.5 degrees. (b), (d), (f), (h) are the corresponding spectrum measured by the spectrometer.

This significant difference in the sliced pulses' spectra agrees well with the simulation result that is shown in Figure 4.15. For this simulation, the relation $\boldsymbol{E}_{\text{Sliced}}(t) \propto A \cdot \boldsymbol{E}_{\text{O}}(t) + \boldsymbol{E}_{\text{O}}(t)\boldsymbol{E}_{\text{T}}(t)$ (Equation 4.11) is used to calculate the sliced output pulse. The optical chirped input pulse can be described as follows: $E_{\text{chirp}}(t) = \sin\left(\omega t + \frac{\alpha}{2}t^2\right) \text{Exp}\left(-\frac{t^2}{0.72\tau^2}\right)$, where $\tau = 10\,\text{ps}$, $\alpha = 2.77\,\text{ps}^{-2}$ are determined through cross-correlation with the reference pulse. As mentioned before, A is the coefficient taking into account the relative magnitude and phase between the chirped and the nonlinear term [106]. In the simulation, the data taken from the actual measurement is used as the input for $\boldsymbol{E}_{\text{O}}(t)$ and $\boldsymbol{E}_{T}(t)$, and A is the only fitting parameter. The fitting parameters A, is found to be +0.21 and -0.07 to match the experimental result of +1° and -1°, respectively (see Figure 4.15). The difference of these two estimations can be attributed to the error of the zero angle determination that has a magnitude of around 0.5°.

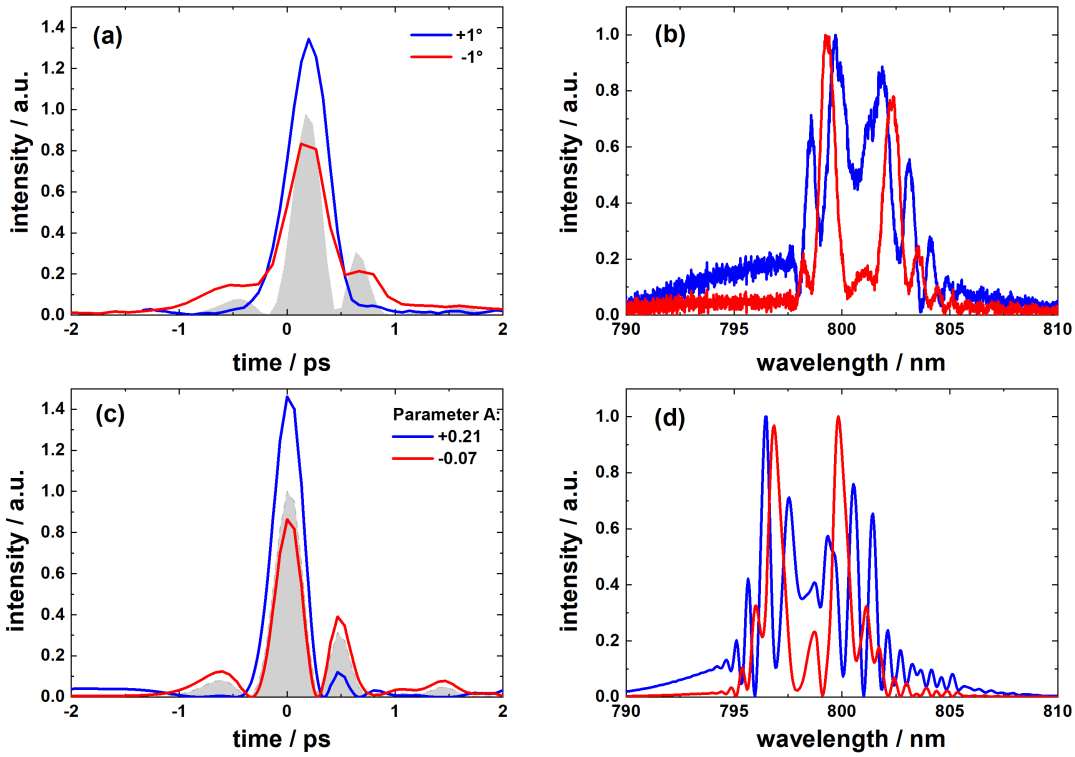

Figure 4.15: Comparison between the simulated and the experimental result in the cross-correlation and the spectrum of the sliced pulse. Experimental characterization of the sliced laser pulse: (a) pulse temporal shape from cross-correlation measurements between sliced and laser line A reference pulses. The intensity of the THz gate pulse is also shown (gray-shaded). (b) spectrum at different GT^* prism tilts (1° and −1°) around its crossed orientation. Simulation of the (c) pulse shape of the sliced pulse and (d) sliced laser pulse spectrums at GT^* prism tilts around its crossed orientation. The spectrums are obtained through Fourier transform.

4.5.3 Jitter compensation ability

The jitter compensation ability of the THz-slicing technology has been tested by a benchmark THZ-TDS experiment. In this experiment, an additional temporal delay (*emulated jitter*) is added into Laser A (through adjusting Delay A, see Figure 4.6) to emulate jitter between Laser A and Laser B. By verifying the arrival time changes of the EO sampling trace of the THz pulse measured under various input emulated jitter, the jitter compensation ability the of THz-slicing approach can be benchmarked.

More specifically, the emulated jitter (generated by Delay A) is added into Laser A pulse, which later generates the THz pulse in the ZnTe crystal in the benchmark THz-TDS setup (see Figure 4.8). Thereafter, the THz pulse is measured by a conventional EO sampling method using *sliced pulse* as probe pulse.

If the THz-slicing approach failed in enabling the synchronization between the THz pulse and the probe pulse, i.e., the sliced pulse is not synchronized with the THz pulse, then the measured EO sampling trace will show a temporal shift proportional to the input emulated jitter. Oppositely, if the THz-slicing approach successfully established the synchronization between the THz pulse and the laser pulse, then the measured EO sampling trace will not show any temporal shift, i.e., the THz-TDS system is immune from the emulated jitter. For details about the principle of EO sampling please refer to Subsection 2.3.2.

In the benchmark experiment, discrete emulated jitter: −6.7 ps, −3.3 ps, 3.3 ps and 6.7 ps are added to Laser A by changing optical path length of Laser A via Delay A. The THz pulses probed by the slice under various emulated jitter values are shown in 4.16(a). It can be clearly seen that EO sampling traces only show a small change in terms of the arrival time of the THz pulse and its shape under various emulated jitter values between -6.7 to 6.7 ps. In other words, the THz-slicing technology successfully enables the probe pulse to be immune from a broad range of timing offsets which correspond to significant jitter (13.4 ps)in a real-world experiment. Moreover, as shown by Figure 4.16(b), normalized power spectra of the measured THz pulses also show consistency under various jitter values. In summary, using the sliced as the probe pulse can reduce the large jitter without affecting the detection spectrum of the EO sampling.

To estimate the residual jitter value after applying the THz-slicing approach, the relative arrival time between the THz and the sliced pulse is deduced from the primary peak position of each EO sampling trace. As shown in Figure 4.17, the emulated arrival time variation is compensated dramatically: it reduces from a few picoseconds to a few tens of femtoseconds, i.e., the intrinsic synchronization scheme yields an arrival time variation reduction by more than two orders of magnitude [106].

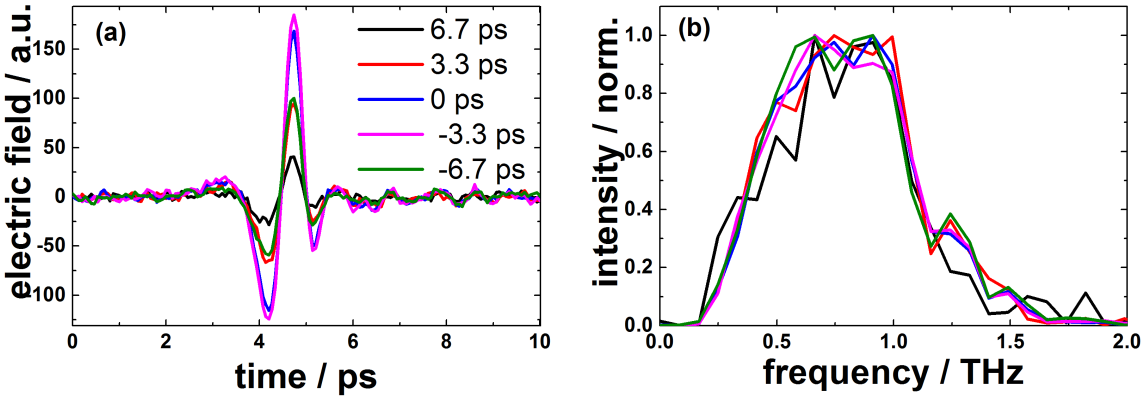

Figure 4.16: Benchmarking of the THz-slicing technology. (a) The THz waveforms measured by EO sampling under various timing offsets. (b) The corresponding normalized spectra of the THz pulses (calculated by Fourier transformation). Taken from [106].

The origins of the remaining arrival time jitter is not fully clear. It could originate from the fact that the THz-slicing process converts the timing instabilities into wavelength variations of the sliced pulse due to its linear chirp, as different spectral components of the sliced pulse are dispersed differently by the optical elements such as the polarizers, waveplates and lenses.

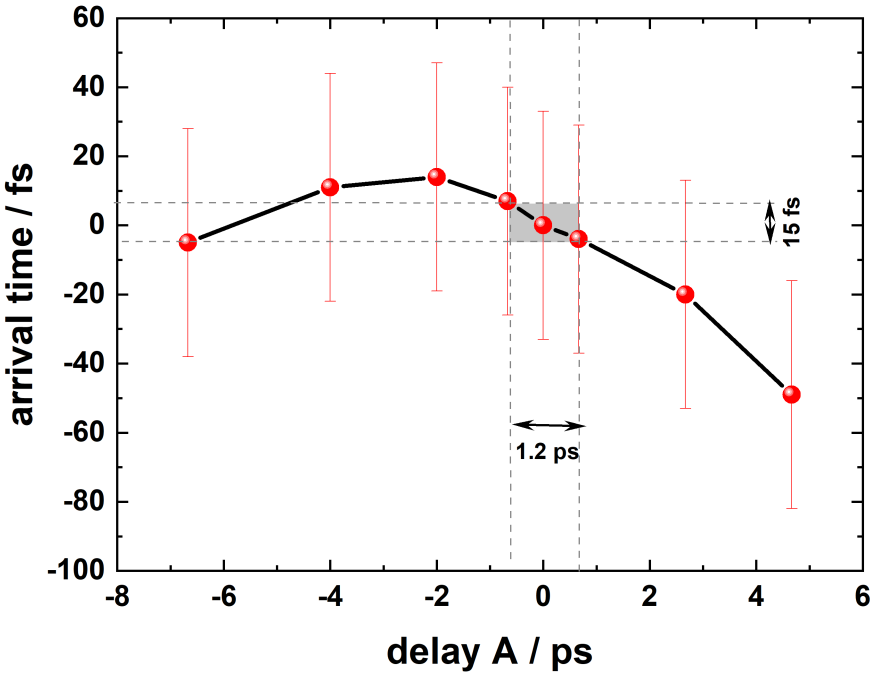

Figure 4.17: Deduced arrival time variation for different emulated jitter values. The gray-shaded area represents the typical arrival time variation (FWHM) of TELBE. Taken from [106].

The amplitudes of the resulting EO sampling traces are not stable but change with the emulated jitter value (see Figure 4.16(a)). This can be attributed to the fact that different sliced pulses have different amplitudes that changes with the emulated jitter. This is further because of (i) the different overlapping position between the THz gate pulse and the chirped pulse and (ii) the Gaussian shape of the chirped pulse.

The jitter compensation ability can be clearly seen in Figure 4.17, which plots the arrival time of the THz pulses against the emulated jitter (Delay A). In the case of TELBE, with arrival time variation less than 1.2 ps (Figure 4.17 vertical dashed lines), the jitter can be reduced to 15 fs (Figure 4.17 horizontal dashed lines).

Figure 4.18(a) shows the measured cross-correlation signal of the sliced pulses that varies with the input jitter. The Gaussian shape of the chirped pulse makes the amplitude of the sliced pulse change with the emulated jitter. As can be seen in Figure 4.18(b), the amplitude of the sliced pulses corresponding to various emulated jitter values (represented by red dots), coincides with the chirped pulse profile very well.

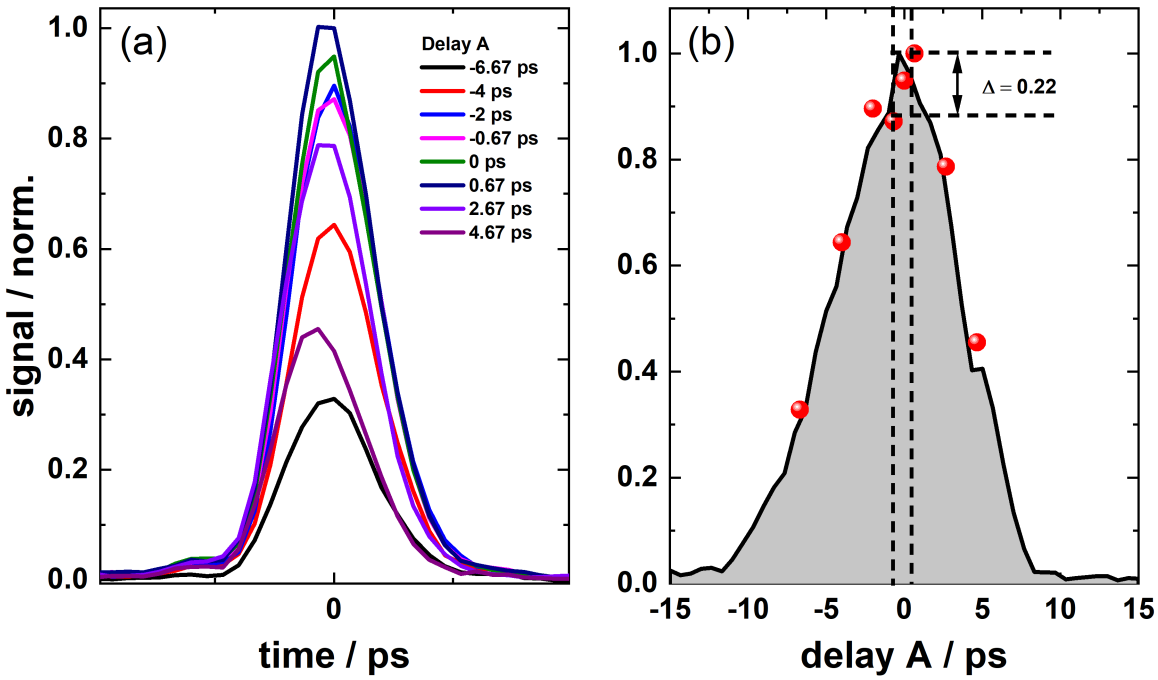

Figure 4.18: Cross-correlation measurements of sliced pulses under different emulated jitter values (By changing Delay A). (a) Sliced pulse cross-correlation measurements under different emulated jitter values. (b) The black curve is the cross-correlation result of the chirped pulse and red dots represent the peak height of the corresponding sliced pulse cross-correlation signal measured under the same emulated jitter value. Two vertical dash lines indicates the typical 1.2 ps (FWHM) arrival time variation. The horizontal dash lines denote the corresponding 22 % sliced pulse intensity variation resulting from the arrival time variation.

Most important is that the 183 fs (RMS) pulse duration of the sliced pulses does not change with the emulated jitter. Please note, that for the sake of demonstration, timing offsets that correspond to jitter values of up to 6.7 ps are used, which is much bigger than the jitter value of 1.2 ps (FWHM) in experiments using the actual accelerator-based THz sources at TELBE. Therefore, the amplitude variation of the sliced pulse will be around 10 % when taking the typical 1.2 ps THz-laser pulses jitter at TELBE into consideration (see Figure 4.18(b)).

4.6 Conclusion and outlook

In conclusion, the THz-slicing method has been experimentally demonstrated for the first time. It is shown that gating with single-cycle THz fields can result in a sliced pulse with a single peak temporal distribution with half the duration of the gate pulse. It is demonstrated that the technique is a fully passive alternative to both fundamental concepts currently utilized in large-scale XFEL facilities: (i) pulse-resolved *post mortem* timing and data correction [107, 62, 28, 108] and (ii) sophisticated active feedback loops correcting for arrival time drifts by fast adjustment of the accelerator phase [65]. In the tabletop proof-of-principle experiment, we have successfully demonstrated that an initial timing jitter in the order of tens of ps can be compressed to the scale of 10 fs.

The next step was to employ, demonstrate and test the THz-slicing method in a real-world experiment at the TELBE facility. The ultrafast pump-probe experimental setup implementing the THz-slicing method at TELBE as developed within this thesis is shown in Figure 4.19.

In this setup, the pulses from the CDR emitter is acting as THz gate pulse. The results of different benchmark pump-probe experiments conduced at the TELBE facility are represented in Chapter 5.

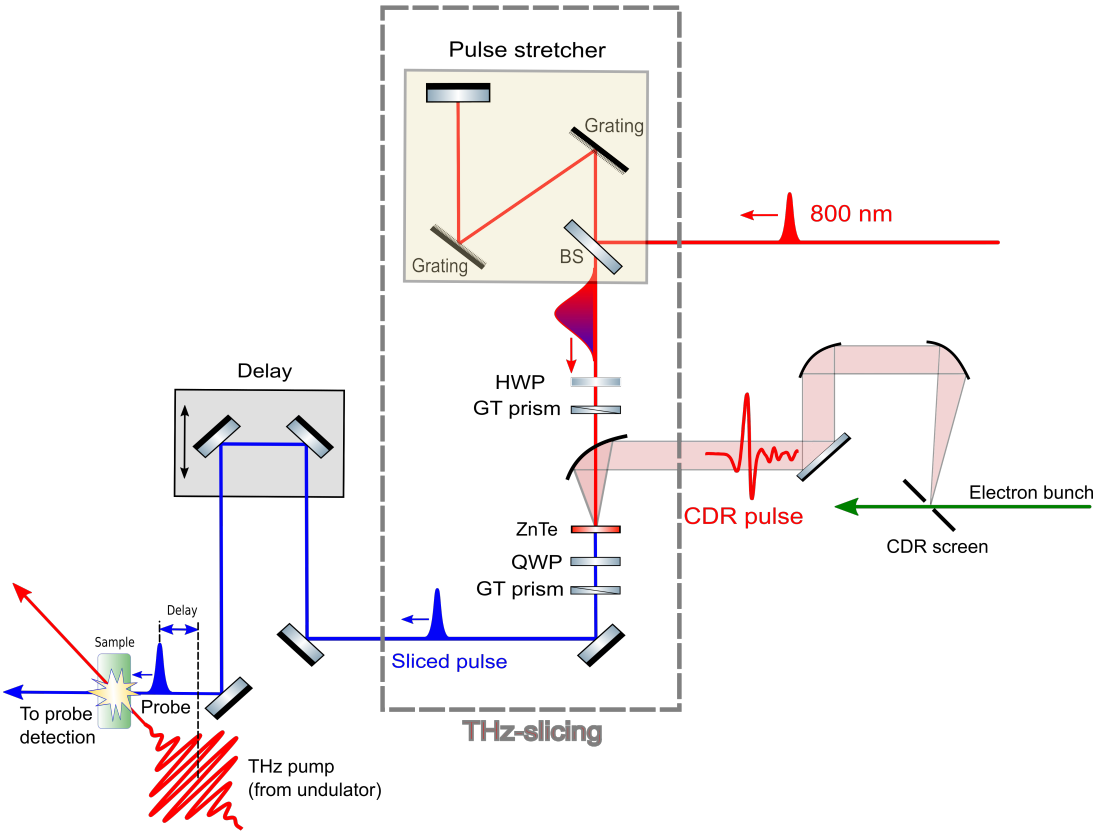

Figure 4.19: Ultrafast pump-probe experimental setup of TELBE utilizing the new THz-slicing concept. The 100 fs long 800 nm probe pulse is stretched by a grating pair stretcher and then interact with the CDR pulse in the ZnTe crystal. The CDR THz pulse slices a portion of the chirped laser pulse and generates an intrinsically synchronized femtosecond sliced pulse, which is directly used to probe the sample excited by multicycle THz pulse from the undulator. The gray dash frame indicates the THz-slicing module, which enables the synchronization between the sliced pulse and the CDR pulse.

5

THz-slicing method – benchmark experiments

In this chapter, benchmark experiments applying the THz-slicing approach – conducted at the TELBE facility – are presented. As a first step, the dynamic range and the signal-to-noise ratio of a THz-slicing-based linear THz Time-domain Spectroscopy (THz-TDS) measurement are characterized. Further, two additional experiments are performed to prove the applicability of the THz-slicing method. Both of these experiments are also based on the THz-TDS technique but the detected THz signals are extremely small in magnitude.

One is a nonlinear THz spectroscopy experiment (Section 5.2), measuring the High Harmonic Generation (HHG) signal from a grating-graphene metamaterial. The other one is a time-domain THz near-field microscopy experiment based on a novel THz Scattering-type Scanning Near-field Optical Microscopy (s-SNOM) (Section 5.3),

5.1 THz time-domain spectroscopy

5.1.1 Experimental setup

Figure 5.1 shows the setup of the benchmark THz Time-domain Spectroscopy (THz-TDS) experiment. The setup consists of two main modules: (i) the THz-slicing module to generate the sliced pulses and (ii) the ultrafast experiment module which in this case is a State-of-the-art THz-TDS setup.

In this experimental setup, laser pulses with 35 fs pulse duration, 800 nm central wavelength, and 250 kHz repetition rate are chirped and stretched by one 15 cm-long glass rod made of N-SF6 glass to a duration of around 0.5 ps (RMS). The laser pulse is chirped and stretched by a 15 cm long glass rod made of NSF-6 glass.

The THz pulse generated by the electron bunch at the CDR screen is guided to and focused onto a 2 mm-thick ZnTe crystal where it acts as the THz gate pulse in the THz-slicing process, as described in Chapter 4. The experimental setup for the THz-slicing module is the same as the one used in the proof-of-principle experiment shown in Figure 4.2 in Chapter 4.

Here, the CDR pulse is used as the THz gate pulse in the THz-slicing module because of its quasi-single-cycle waveform that allows a comparably short sliced pulse duration. Besides, the CDR pulse is intrinsically synchronized to any other secondary coherent radiation that is generated from the *same* electron bunch. Therefore, the sliced pulse generated using the CDR gate pulse is intrinsically synchronized[1] to the undulator pulse, which allows using the sliced pulse as a synchronous probe pulse for the majority of experiments at TELBE, in which the undulator pulse serve as pump pulse.

After obtaining the minimal sliced pulse duration (see Section 4.5 in Chapter 4), the sliced probe pulses are sent to the 100 µm thick (110)-cut ZnTe crystal, onto which the undulator pulse is also focused and overlapped in time and space with a pulse energy of 36 nJ in order to to measure the electric field of the undulator pulses by THz-TDS based on EO sampling (see Figure 5.1). Please note, a mechanical chopper combined with a Lock-in amplifier is used to increase the detection sensitivity

[1]Please note, the intrinsic synchronization between the CDR and the undulator pulses still shows a small jitter of up to a few hundred fs, which could affect the performance of the THz-slicing method (see Section 3.4 in Chapter 3).

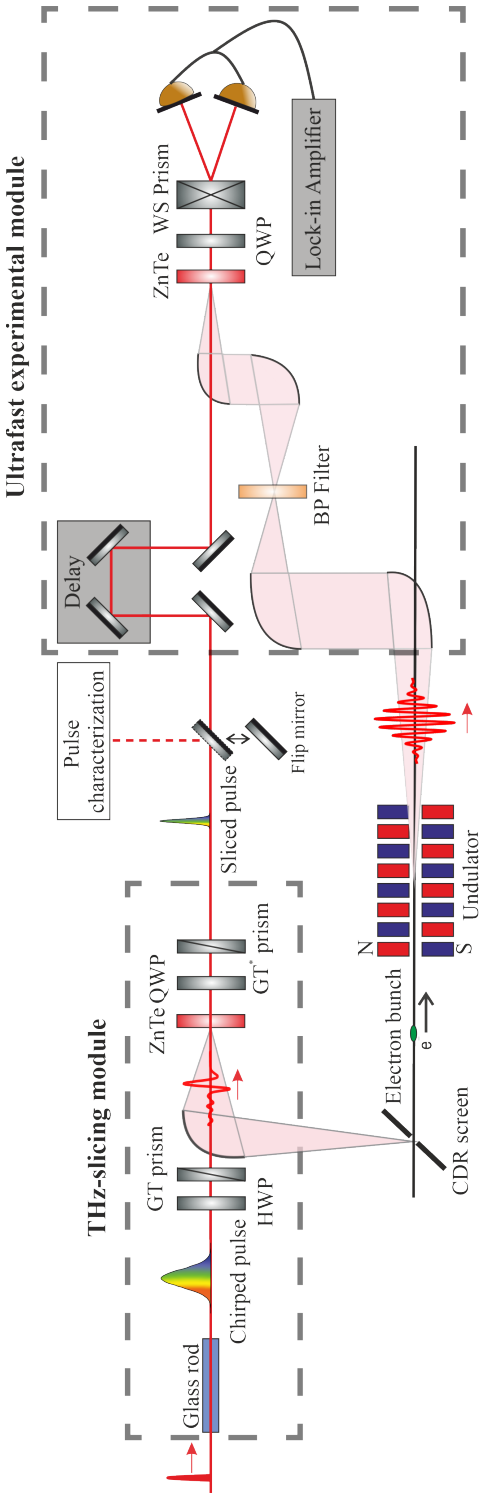

Figure 5.1: Experimental setup of the THz time-domain spectroscopy experiment using THz-slicing technology in conjunction with the THz pulses from the TELBE undulator source. Two dashed rectangular boxes indicate the THz-slicing module and the ultrafast experimental module, respectively. In the THz-slicing module, a glass rod and a set of optical polarization components are used. A flip mirror is used to redirect the sliced pulse to characterize its pulse duration and spectrum. In the ultrafast experimental module, a Bandpass (BP) filter is placed in the undulator beampath to reduce the higher harmonic frequency components of the undulator pulse. After the BP filter, the undulator pulse is focused on the ZnTe crystal for the EO sampling measurement.

5.1.2 Sliced pulse characterization

As described in Section 4.5, the duration of the sliced pulse is critical since it determines the achievable temporal resolution and therefore the higher cut-off frequency of the THz-TDS measurement when using the sliced pulse as probe pulse. Other relevant parameters are the pulse energy of the sliced pulse and the ratio between the pulse energy of the sliced pulse and the overall leakage in the absence of the THz gate pulse, i.e. the probe contrast.

The sliced pulse duration can be determined by measuring its intensity autocorrelation, in our case through non-collinear SHG in a 100 µm Beta Barium Borate (BBO) crystal [103]. After adjustment of the polarization components, i.e., the GT prisms and the QWP placed in the THz-slicing module after the EO crystal, a minimum pulse duration of the sliced pulse of 150 fs (RMS) can be obtained. The corresponding autocorrelation signal of the sliced pulse is shown in Figure 5.2 as a black-colored solid curve.

This minimal 150 fs (RMS) sliced pulse duration can be attributed to the limited bandwidth and hence finite pulse duration of the CDR pulse due to the aperture size of the CDR screen and the electron bunch length [62, 63]. Currently, the upper limit of the spectral bandwidth of the CDR pulse is about 1 THz with a 4 mm aperture diameter of the CDR screen (see supplementary material in Ref. [62]) corresponding to a CDR pulse duration of around 2 ps. The sliced pulse energy is measured to be 18 nJ, which corresponds to around 0.3 % slicing efficiency (initial energy of the stretched pulse was 5.5 µJ). The leaking pulse, which is the transmitted probe pulse with the absence of the THz gate pulse, is measured to be 1.2 nJ. This corresponds to 6.7 % of the sliced pulse energy.

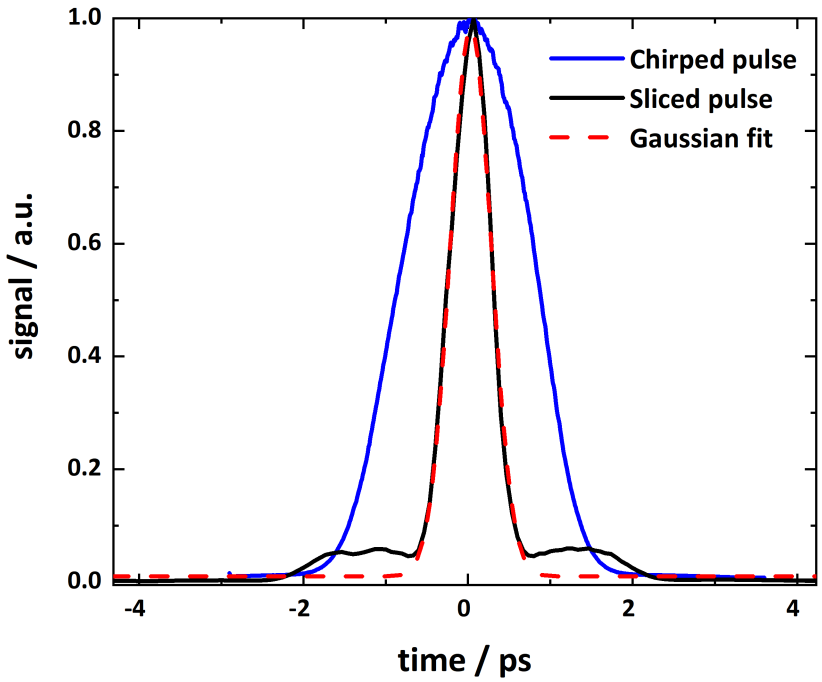

Figure 5.2: Autocorrelation signal of the chirped (blue) and the sliced (black) pulse. The measurements yield pulse durations of 0.5 ps (RMS) for the chirped and 150 fs (RMS) (353 fs (FWHM)) for the sliced pulse. The red dashed curve is a Gaussian fit.

5.1.3 Experimental results

Signal to noise ratio and dynamic range of the THz-slicing method

In order to characterize the performance of the THz-TDS measurement with the THz-slicing method, THz-TDS measurements were performed to sample the THz fields of the pulses from the TELBE undulator source. In this experiment, the frequency of the undulator pulse is tuned to 0.3 THz. The CDR pulse (pulse energy of 96 nJ) is utilized as gate pulse in THz-slicing. As introduced before, the 0.5 ps (RMS) long chirped 800 nm pulse is focused collinearly with the CDR pulse onto the ZnTe crystal in the THz-slicing module, as shown in Figure 5.1.

To estimate the SNR of the THz-slicing technology, the range of the scanned delay of the probe pulse is set to be around five times of the undulator pulse duration so that the signal before the THz pulse arrival can be analyzed in parallel.

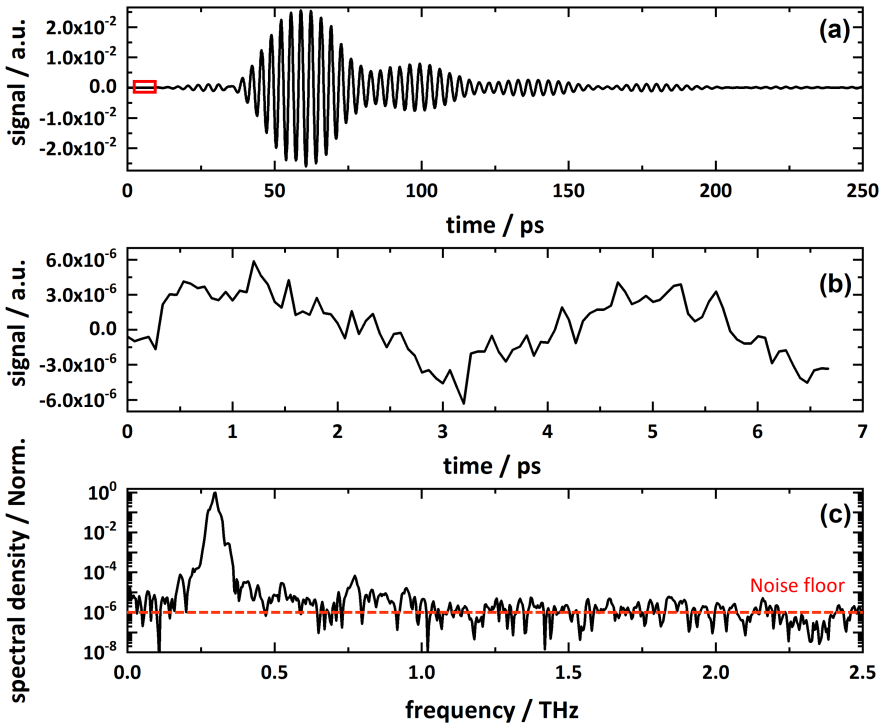

Figure 5.3: Benchmark THz-TDS measurement of the undulator pulse probed by the sliced pulse. (a) EO sampling of undulator radiation tuned to 0.3 THz. Please note, one 0.3 THz bandpass filter is put in the undulator beampath to suppress other residual spectral components from the source. (b) Noise signal measured in the time interval from 0 to 7 ps by the EO sampling method without the THz field (corresponding to the red rectangular area in (a)). (c) Power spectrum of the EO sampling trace. The narrow dashed red line indicates the top-down estimate of the noise signal.

Figure 5.3(a) shows the normalized electric field waveform of the undulator pulse measured using EO sampling. The noise amplitude of around 6×10^{-6} can be deduced from the noise measurement (see Figure 5.3(b)), with the absence of the THz pulse. Thus, by dividing the maximal signal strength with the noise amplitude, a SNR of the order of 10^4 can be deduced. A dynamic range in the frequency domain of 10^6 can be also extracted from Figure 5.3(c) by comparing the maximal signal with the noise floor.

For the *post mortem* method, the dynamic range is also in the order of 10^6, while the SNR is in the order of 10^3 [32]. As the dynamic range and the SNR of the THz-slicing method are comparable with those of the *post mortem* method, the high sensitivity and

therefore applicability of THz-slicing is clearly demonstrated for this general type of THz TDS experiments.

Drift compensation ability of the THz-slicing method

The drift compensation ability of the THz-slicing approach is tested through measuring the THz-TDS of the undulator pulse under different THz-probe pulse jitter levels. In this experiment, the frequency of the undulator pulse is tuned to 0.5 THz and a 0.5 THz BP filter is put into the undulator beampath before focusing onto the ZnTe crystal. Please note, that the undulator-laser jitter is manually adjustable from 540 fs to 4 ps (RMS) through tuning the "Gain" value of the Synchrolock (for details about jitter adjusting, please refer to Appendix A). The whole measurement of four traces took around four hours. It can be seen from Figure 5.4 that the shape and the arrival time of the undulator pulses are almost identical when the THz-probe pulse jitter varies in the range from 540 fs to 4 ps (RMS). The drift observed between the different traces, shown by the inset in Figure 5.4, is below 25 fs. This small drift indicates excellent performance of the THz-slicing approach under an extensive range of THz-probe pulse jitter levels and demonstrates the robustness of the THz slicing approach.

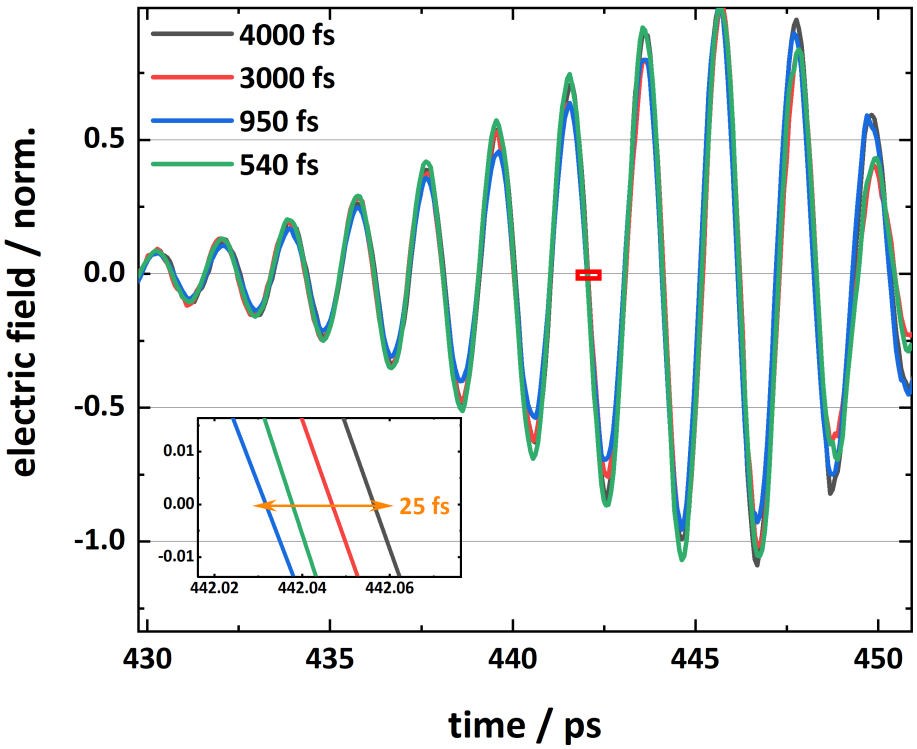

Figure 5.4: Stability of the jitter compensation ability of the THz-slicing technique. Time-domain waveforms of the undulator pulse probed by the sliced pulse when the initial THz-probe pulse jitter is tuned to 540 fs, 950 fs, 3000 fs, and 4000 fs, respectively. Inset: The zoom-in view of the red rectangular area at one zero-crossing position.

5.2 THz high harmonic generation in grating-graphene metamaterial

5.2.1 Experimental setup

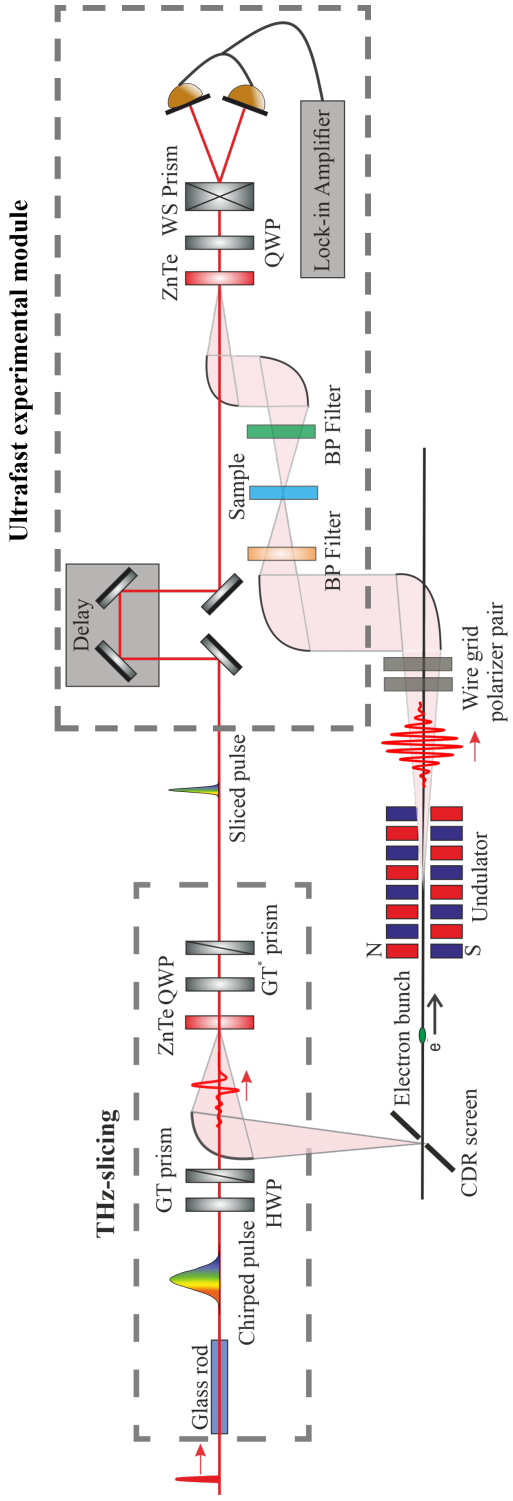

Figure 5.5: Experimental setup of the nonlinear THz-TDS experiment. A pair of wire grid polarizers are used to change the intensity of the undulator radiation. Two BP filters are put before and after the sample for the purpose of frequency purification. The THz radiation emitted from the sample is measured by EO sampling with the sliced pulse as probe pulse.

Besides the linear THz-TDS for the characterization of the THz field generated by the undulator, a benchmark experiment has been performed to verify the application of the THz-slicing technique in a *nonlinear* THz-TDS experiment. The chosen example experiment is THz HHG in a grating-graphene metamaterial which had previously been pioneered at TELBE with the pulse-resolved DAQ scheme [109, 36]. The recently demonstrated novel grating-graphene metamaterial was chosen, because it has proven to exhibit a particularly high conversion efficiency in generating THz harmonics owing to the characteristic carrier dynamics in the Dirac-type electronic band structure [110, 111, 112] combined with the field enhancement in a plasmonic structure. A metallic grating structure on the graphene enhances the pump field strength and thereby increases the overall conversion efficiency. (For details about the sample, please refer to [109].)

The experimental is schematically shown in Figure Figure 5.5. Two additional wire grid polarizers are placed into the undulator beampath to control the pump pulse's field strength. The graphene sample is put in the focus of the undulator THz radiation under normal incidence in the ultrafast experiment module. The fundamental frequency of the undulator source is tuned to 300 GHz and the pulses are spectrally cleaned with one 300 GHz BP filter. Behind the sample, a 900 GHz BP filter is inserted to suppress any residual fundamental in order to increase the detection sensitivity of the 3rd harmonic of the fundamental frequency.

5.2.2 Experimental results

THz-TDS measurements of the generated 3rd harmonic under various fundamental pump field strengths (shown as percentage with respect to full power) are shown in Figure 5.6. The maximum pump field strength (shown as 100 % in Figure 5.6) corresponds to 13 kV/cm.

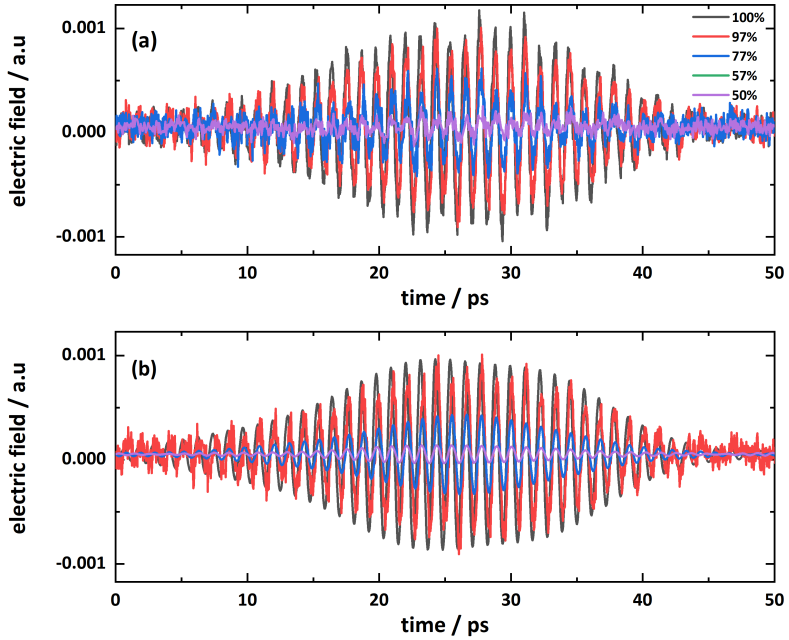

Figure 5.6: Electric field Waveform of the THG signal from graphene metamaterial. (a) The waveform of the 3rd THz harmonic under different fundamental pump field strengths (100 % corresponds to 13 kV/cm). (b) To enhance the visibility of the harmonic signal, the set of 3rd THz harmonic is also shown after applying a digital 0.8-1 THz BP filter.

The corresponding pump field strength-dependent power spectra of the 3rd harmonic can be seen in Figure 5.7.

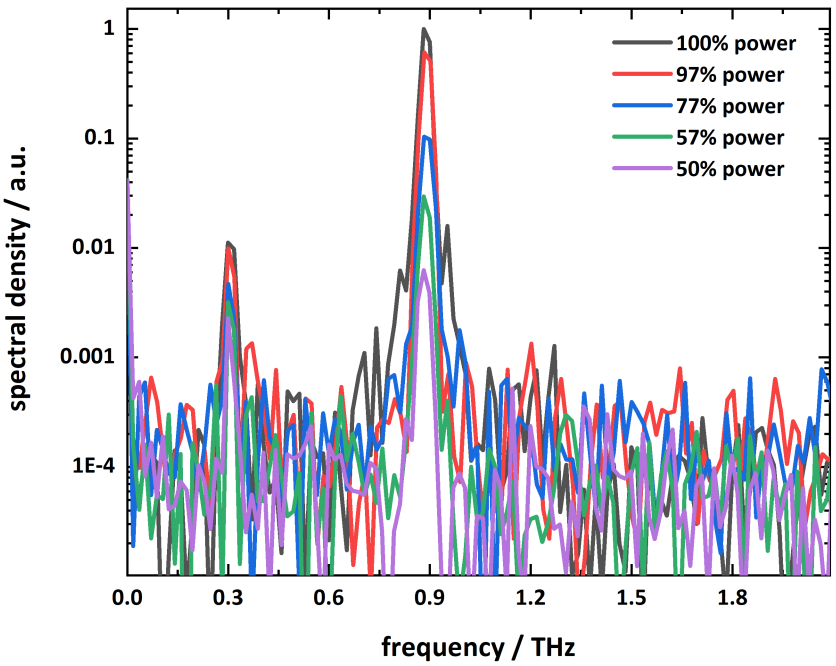

Figure 5.7: Normalized spectra of the 3rd harmonic signal at different pump field strengths with the 900 GHz bandpass filter placed right after the sample.

The normalized 3rd harmonic peak field strength is plotted as a function of the normalized fundamental peak field strength on a logarithmic scale in Figure 5.7. A nonlinear relationship can be extracted from the slope of the linear fit [2]. As shown by the dashed line, the slope is 1.67, which is smaller than the value of 3, which would be expected for a 3rd order perturbative process, indicating that the experiment is in the so-called saturation regime where the absorption saturation limits the energy transfer. The result is comparable with the results obtained through the conventional ATM-based *post mortem* DAQ method from the same metamaterial, where it was shown that the saturation regime is already reached for incident field strengths on the order of < 10 kV/cm (See Ref. [109]). Due to the limited scope of this thesis, please refer to Refs. [15, 109] for details about the THG mechanism in the grating-graphene.

[2] By taking the logarithm on both sides of an arbitrary power function, e.g., $y = x^n$, the power function can be rewritten as a linear function $\log y = n \cdot \log x$ where the exponent n is the slope of the linear function.

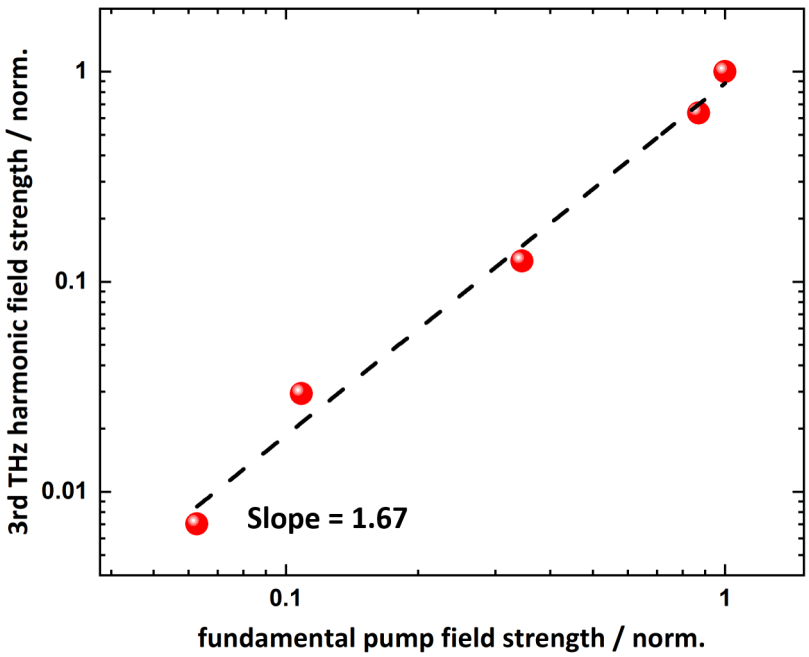

Figure 5.8: Normalized THG strength of grating-graphene as a function of pump field strength in association with the THz-slicing method. The red dots symbolize the normalized THG response deduced from the 900 GHz peak height in the spectrum (as deduced from the spectra in Figure 5.7). The dashed line is the linear fit of the data points with a slope of 1.67. The maximum pump field strength is 13 kV/cm.

5.3 THz time-domain s-SNOM benchmark experiment

5.3.1 Introduction of the THz time-domain s-SNOM

Besides pursuing higher temporal resolution for resolving faster dynamic processes, achieving a higher spatial resolution at the same time is also of great interest, both for fundamental and applied science. Resolving spatially resolved sample responses in the range beyond the diffraction limit with THz radiation could play a significant role in the research of quantum materials, polaritonic systems, plasmonic materials, etc.

However, normal free space THz-TDS experiments can only reach a spatial resolution of 1.5 mm to 5 µm decided by the spot dimension of the THz beam, when the central frequency of the THz radiation is in the range of 100 GHz to 30 THz [113]. In recent decades, a number of methods have been developed to increase the spatial resolution, such as Laser Terahertz Emission Microscopy (LTEM) [114], aperture-based scanning terahertz microscopy techniques [115] and Scattering-type Scanning Near-field Optical Microscopy (s-SNOM) [116, 102, 117, 118, 119], allowing the observation of sub-wavelength structures.

Among these methods, s-SNOM, is a method that can achieve a uniquely high spatial resolution (< 100 nm). s-SNOM utilizes a sharp scanning probe, that interacts with the surface and scatters the near-field radiation to the far field for detection.

In s-SNOM, a metalized tip (tip-apex radius of curvature is around 10-100 nm) oscillating in the vicinity of the sample surface acts as a highly localized probe. A sketch of the working principle can be seen in Figure 5.9. After illuminating an object, two types of fields are reflected from the object: the propagating and the non-radiative field. These can also be

referred to as far-field and near-field zones, respectively. The local dielectric properties of the sample are contained in the non-radiative component. The most prominent approach to detect a non-radiative near-field signal is to bring a sharp metalized probe into very close proximity of the object's surface. The near-field probes, which are typically standard metalized atomic force microscopy tips, make use of the following effects, namely, (i) they enhance the weak local near-field signals, and (ii) they modulate the local fields through oscillation to allow background-free near-field signal extraction.

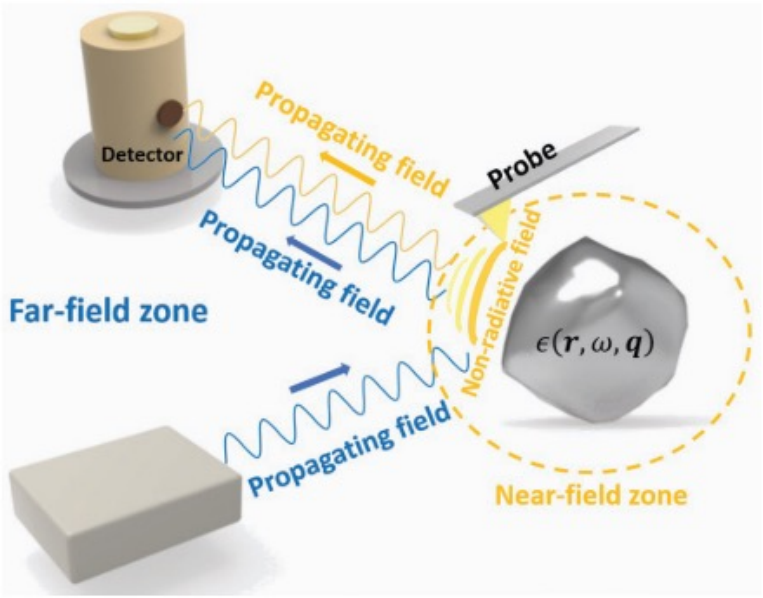

Figure 5.9: Schematic of the principle of s-SNOM. After being illuminated by the propagating field (shown in blue), a nanoscale object reflects the propagating and non-radiative fields (shown in blue and yellow, respectively). The information on the optical dielectric constant of the object $\epsilon(\mathbf{r}, \omega, \mathbf{q})$ (ϵ is a function of $\mathbf{r}$–position, ω–frequency and $\mathbf{q}$–momentum) is encoded into the scattering field that is scattered by the oscillating probe. Taken from [116].

The biggest challenge in s-SNOM is to distinguish between the far-field background and the extremely weak near-field signals, which are typically less than 10^{-4} of the total signal (in terms of intensity). The widely utilized method to suppress the background signal is to apply modulation on the near-field signal at close proximity to the probed surface (typically $<$ 100 nm).

Atomic Force Microscopy (AFM) directly provides such a possibility, wherein one typically uses an oscillating cantilever at its mechanical resonance frequency (typically around 20-250 kHz). By this modulation of the tip height, the near-field signal scattering varies strongly non-linearly as a function of the tip-sample distance, whereas the far-field component scattering varies mainly linearly (especially for long wavelengths). Therefore, through signal demodulation at a higher harmonic of the tip resonance frequency, the near-field signal can be extracted with dramatically reduced contribution from parasitic signals [120, 121, 122]. Please note, in order to effectively demodulate the signal at a higher harmonic of the tip resonance frequency, the laser repetition rate should be at least twice of the demodulation frequency to fulfill the Nyquist-Shannon sampling limit [123].

Conducting s-SNOM experiments in the THz range is highly challenging, as the scattering efficiency from small volumes (such as the tip apex of a s-SNOM tip) scales with λ^{-4}. As

the excitation frequency is reduced to the sub-THz regime, wavelengths increase dramatically, thus compromising the total scattered near-field signal. TELBE, as an accelerator-based THz source, is a unique source for THz radiation for s-SNOM because of its (i) relatively high pulse energy, thus compensating the weak scattering efficiencies at these frequencies, (ii) its relatively narrow bandwidth (in case of the undulator source), and (iii) the high repetition rate up to a few hundreds of kilohertz, as previously described in Section 2.2.

Integrating s-SNOM with the TELBE source is therefore highly promising, as it would be a unique near-field microscopy instrument able to access THz-driven processes with pulse energies up to several tens of µJ. However, integration of the TELBE source with s-SNOM proved to be extremely challenging due to THz pulse intensity fluctuations and timing jitters. One possible approach is to use the ATM-based *post mortem* DAQ technology – that has been applied successfully in a variety of nonlinear THz photonics experiments as explained in Chapter 2 – in combination with pulse-resolved cantilever phase-domain sampling [124].

However, such a method has so far not been successful, as for s-SNOM, complex alignment iterations are required to obtain and optimize a signal. By using such a ATM-based pulse-resolved methodology, for each alignment iteration, data post-processing of over 30 minutes would be required to verify potential near-field signals. Such long waiting times are prohibitive for regular operation. Therefore, developing a method that enables real-time signal feedback is of paramount importance for such an experiment.

The THz-slicing technique exactly fulfills this requirement as it allows the *real synchronization* between the THz and the laser pulse with a precision of a few tens of femtoseconds, as demonstrated by the first benchmark experiments presented earlier in this chapter. Importantly, this method therefore enables direct lock-in based signal demodulation, equivalent to all-based based S-SNOM experiments. This allowed for the very first time a successful demonstration of s-SNOM with an accelerator-based, superradiant THz source.

5.3.2 Experimental setup of the THz s-SNOM

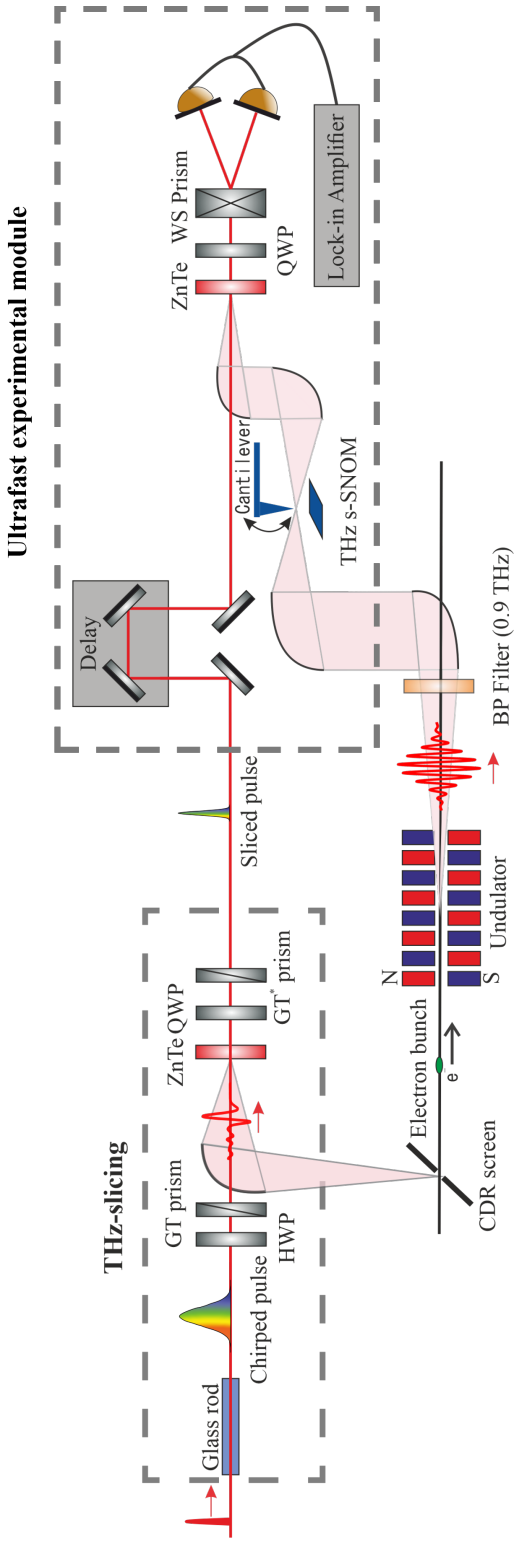

Figure 5.10: Experimental setup of the ultrafast THz s-SNOM benchmark experiment in conjunction with accelerator-based superradiant THz radiation. The dashed rectangular box indicates the THz-slicing module. A delay line is used to change the relative arrival time between the sliced pulse and the undulator pulse. After passing through a 0.9 THz BP filter, the undulator pulse is focused onto the tip of the cantilever and after scattering by the tip it is collected by a parabolic mirror. The scattered THz radiation is measured by means of EO sampling using the sliced pulse as probe pulse.

The experimental setup can be seen in Figure 5.10. As pump pulse, the frequency of the undulator pulse was tuned to 900 GHz with a pulse energy of 36 nJ and a repetition rate of 250 kHz. The sliced pulse generated by THz-slicing is used as probe pulse with pulse duration of 150 fs (RMS) and a pulse energy of 6 nJ.

In the experiment, the undulator pulse is focused on the sample by a parabolic mirror to the position of the sharp tip. The used probe is a commercial full metal PtIr tip (Rocky Mountain Nanotechnology LLC, Model 25PtIr300B, resonant frequency: 21 kHz (± 30 %), with a shaft length of around 80 µm and tip apex radius of curvature of about 20 nm). The near-field signal scattered by the tip as well as the background signal are collected by another parabolic mirror for a conventional EO sampling measurement using the sliced pulse as probe.

5.3.3 Experimental results of the THz s-SNOM benchmark experiment

THz s-SNOM of Au on Si sample

In the first benchmark experiment, a sample with a patterned 200 nm thick Au layer in the center of a Si substrate is chosen as the reflectively difference between Au and Si in the THz range is expected to provide a large contrast in the s-SNOM signal. A sketch of the experimental set-up can be seen in the inset of Figure 5.11(b). The sample is excited with the 900 GHz pulse incident obliquely onto the sample surface. The scattered THz wave is collected by the second parabolic mirror in forward scattering geometry and is transported towards the EO detection scheme.

During the measurement, the vibration frequency of the tip is set to the resonant frequency $\Omega = 22.65$ kHz. The scattering THz signal is demodulated at the fundamental frequency Ω, the 2nd harmonic $2\Omega = 45.3$ kHz and the third harmonic $3\Omega = 67.95$ kHz, respectively. The repetition rate of the THz pulses in this experiment was limited to 250 kHz, so only 3.68 pulses are effectively sampling one cycle of the third harmonic. As the sampling rate is low, long integration times (300 ms) were necessary for the signal demodulation of the waveforms shown in Figure 5.11.

After optimizing the signal at 0.9 THz on a highly reflective Au surface, we recorded for the first time an s-SNOM signal with the TELBE undulator source. The temporal waveforms and the corresponding spectra of the results are shown in Figure 5.11. It can be clearly seen from Figure 5.11(b) that the primary spectral peak is always located at 900 GHz, which is the central frequency of the THz pulse.

Moreover, when performed with FEL sources, typical dynamic ranges of the obtained 1Ω, 2Ω, and 3Ω components were 10^4, 10^3 and 10, respectively. The dynamic ranges achieved with the TELBE source in a highly undersampled regime: 10^4, 10^3 and 10 of 1Ω, 2Ω, and 3Ω components, respectively, are comparable to typical s-SNOM measurements done with FEL sources [125].

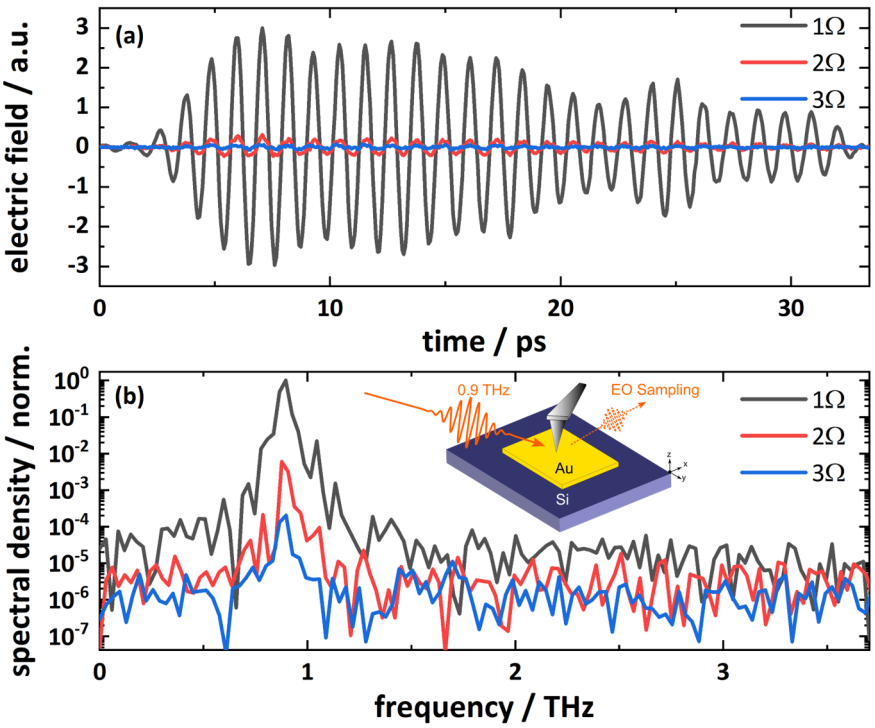

Figure 5.11: THz s-SNOM near-field signal from the Au sample. (a) EO sampling traces demodulated at Ω, 2Ω and 3Ω. (b) The corresponding power spectrum of the EO sampling traces shown in (a). The inset in (b) shows the sketch of of the THz s-SNOM experiment on Au/Si sample. The 200 nm thick Au patterned structure is on the bulk Si substrate. During the experiment, the multicycle undulator pulse is focused on the tip-sample region. The scattered THz wave is collected and detected by EO sampling.

THz s-SNOM on n-Bi_2Se_3 on Si sample

In the second benchmark experiment, the topography (see Figure 5.13(a)) and and the near field signal (see Figure 5.13(b),(c)) of another sample, namely the n-doped 186 nm thick Bi_2Se_3 flake sample on the High resistivity float zone silicon (HRFZ-Si) substrate are measured. The n-doped Bi_2Se_3 crystal is a commercially available crystal (purity $>$ 99.9999 %, 2D Semiconductors Inc., USA) exfoliated onto double-side polished, THz-grade, high resistivity float-zone silicon substrate (Tydex LCC, Russia) The substrate was thoroughly cleaned with deionized water, acetone and isopropyl alcohol. Following a drying process (nitrogen air blow), the substrate surface was plasma treated (O2, 1 mbar, 5 min.) in a low energy plasma cleaning chamber (Pico, Diener electronic GmbH + Co. KG, Germany).

The experimental scheme is exactly the same as the one used for the Au sample (see Figure 5.12).

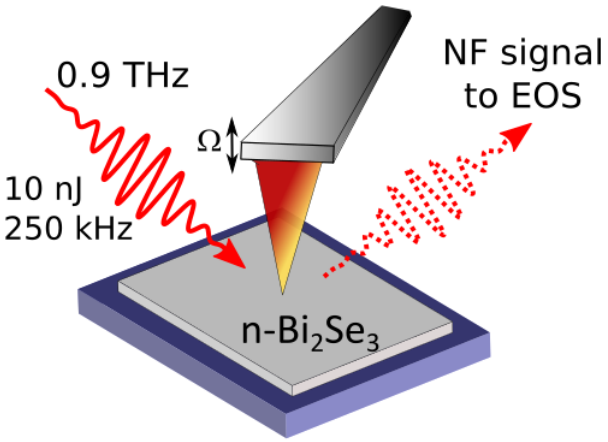

Figure 5.12: Sketch of the THz s-SNOM experiment on a Bi_2Se_3 sample. The 186 nm thick n-doped Bi_2Se_3 flake sample is on the HRFZ-Si substrate. During the experiment, the multicycle undulator pulse is focused on the the tip-sample region. The scattered THz wave is collected and detected by EO sampling.

The undulator pulse energy is 10 nJ at 250 kHz repetition rate. As Figure 5.13(b) shows, the s-SNOM signal from Bi_2Se_3 demodulated at the second harmonic of the tip oscillation frequency is notably higher than that from the substrate. From Figure 5.13(c), similar to the spatial resolution definition used in Reference [126], a spatial resolution in the order of 200 nm can be conservatively estimated from the 2Ω signal variation crossing the sample boundary. Please note, in this experiment, the 200 nm is not the ultimate achievable spatial resolution as the sampling pixel size chosen in the experiment was not optimized because of the time limit of the experiment. Nevertheless, the 200 nm spatial resolution is 3 orders of magnitude smaller than diffraction limit (around 100 µm) when the sample is illustrated by THz pulse with a central frequency of 0.9 THz.

Please note, that the details about the interaction mechanism between the tip and the sample is out of the scope of this thesis.

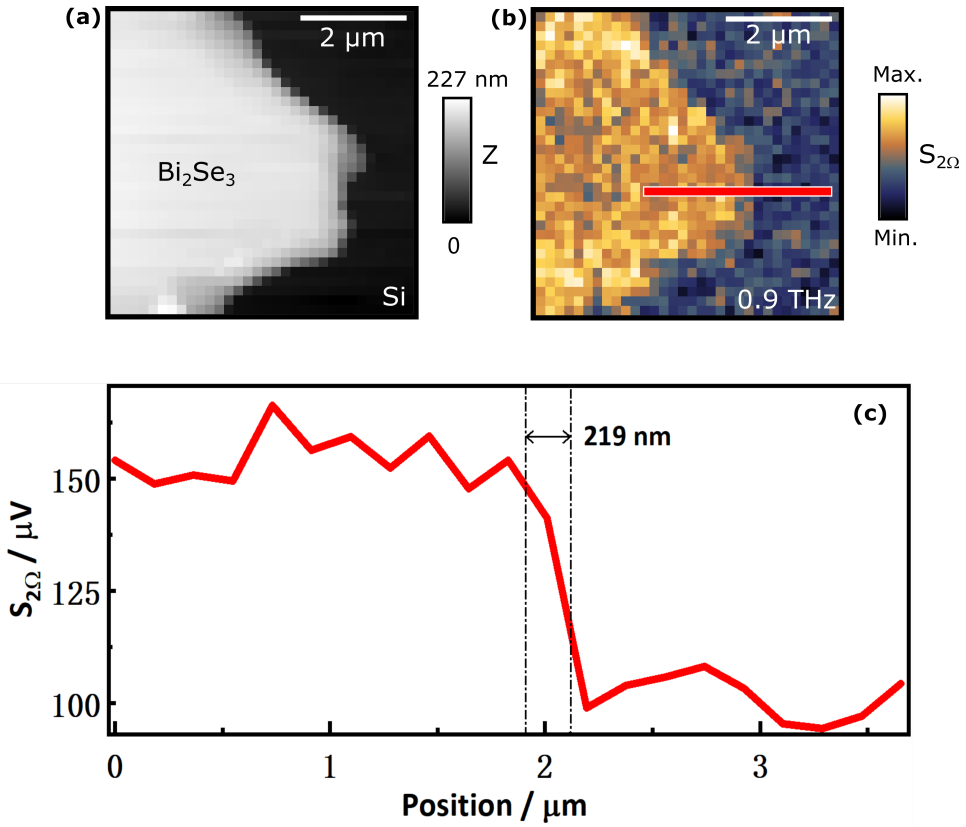

Figure 5.13: Experimental results of the THz s-SNOM experiment on an n-doped Bi_2Se_3 flake. (a) AFM topography image. The gray scale value of each pixel indicates the height. (b) The 2Ω THz s-SNOM image and (c) the 2Ω near-field signal strength along the red bar shown in (b). A spatial resolution of in the order of 200 nm can be conservatively estimated from the near-field signal variation.

5.4 Conclusion and outlook

In this chapter, the applicability and performance of the THz-slicing method have been characterized at TELBE by performing different benchmark experiments. It is experimentally shown that the THz-slicing technique can reduce an initial undulator-laser jitter in the range from 500 fs to 4 ps (RMS) (See Appendix A) down to 44 fs (RMS) (see Appendix B.2). This means that fs-level synchronization can be achieved even when the initial jitter is in the ps range. Besides, due to the passive nature of the THz-slicing method, experiments that require heterodyne detection or long signal acquisition times become feasible without losing temporal resolution. Using Lock-in amplifier-based detection techniques with the THz-slicing method, a high SNR up to 10^4 can be achieved in electro-optic detection schemes, which is a prerequisite for nonlinear THz spectroscopy.

In the THz-slicing method-associated nonlinear THz-TDS benchmark experiment – THz HHG from a grating-graphene metamaterial – the application of the THz-slicing method has yielded similar results compared to an experiment using the *post mortem* data correction method, but with significantly reduced data acquisition time and data volume.

Compared to the *post mortem* data correction method, another advance brought by the THz-slicing technique is that it enables types of experiments that cannot be realized with the data correction method, one of which is THz s-SNOM. The THz s-SNOM technique is based

on a coherent detection technique measuring the signal carried by the higher harmonics of the oscillations of an AFM tip. In the *post mortem* data correction method, the randomly arriving THz pulses couple to the tip oscillation phase and render the demodulation technique inapplicable. On the contrary, it is demonstrated within this thesis that the THz-slicing method achieves a *real synchronization* between the undulator and the probe laser pulse and enables the s-SNOM signal extraction by demodulation.

In the THz-slicing method-associated benchmark THz time-domain s-SNOM experiment at TELBE, a sub-diffraction-limit spatial resolution of about 200 nm has been observed, which is three orders of magnitude higher than the diffraction limit (around 100 µm) when the sample is illuminated by THz pulses with a central frequency of 0.9 THz.

Moreover, the THz-slicing method can also overcome the operation speed limitation of the data correction method, which is given by the readout speed of the line scan camera in the ATM. The passive nature of the THz-slicing method enables its application under megahertz repetition rates, which is demanded at modern FELs facilities, e.g., European XFEL, LCLS-II or FELBE.

The performance of the THz-slicing method in a THz-TDS experiment is mainly limited by the sliced pulse duration, since a longer sliced pulse duration reduces the upper cutoff frequency of the THz-TDS experiment, as previously introduced in Section 2.3. In the case of the benchmark THz-TDS experiment, the cutoff frequency of the 353 fs (FWHM) sliced pulse is around 1.5 THz. One direct way to reduce the sliced pulse duration is using a shorter THz gate pulse. In facilities such as LCLS, Fermi, or FLASH, that can provide electron bunches with durations of a few tens of fs, THz pulses generated from a CDR screen or bending magnet could be much shorter than in the case of TELBE, and therefore a few tens of fs long sliced pulse can be achieved in principle.

Another possible way is to compress the sliced pulse duration through nonlinear optical techniques. In this case, one needs to consider using Fourier-transform-limited pulses instead of chirped pulses. Because compared to the chirped pulse, the sliced pulse generated from the Fourier-transform-limited pulses has much less frequency components and therefore will be much easier to be compressed using dispersion compensation methods based on nonlinear optical techniques.

6

Summary and outlook

Accelerator-based superradiant THz sources have many unique advantages compared to conventional table-top laser-based THz sources, such as having a high repetition rate, high spectral density, high electric field strength, and large wavelength tunability of the emitted radiation at the same time.

However, because of the complexity of an accelerator-driven lightsource, reaching a synchronization between the accelerator-based source and external laser pulses with an accuracy in the sub-100 fs regime is challenging. Without precise synchronization or timing between the THz pump and external probe pulses, ultrafast time-resolved pump-probe experiments cannot be performed with competitive temporal resolution. Therefore, achieving accelerator-based THz vs. laser pulse synchronization is crucial in enabling ultrafast pump-probe experiments with accelerator-driven lightsources. There are two major ways that can increase the temporal resolution. One way is to increase the timing accuracy by monitoring the arrival time between the THz and the laser pulse and correcting the data after the measurement. Another way is to improve the actual synchronization between both pulses.

In this thesis, novel methods are implemented and characterized, which follow both of these routes. First, with the goal to improve the measurement of the timing accuracy between THz and external laser pulses, this thesis introduces the double-Arrival Time Monitor (ATM). This upgrade to the single-ATM scheme significantly enhances the accuracy of the *post mortem* data correction method (see Chapter 3): the top-down[1] pulse to pulse temporal resolution of the ultrafast THz pump laser probe experiment is improved from around 50 fs (RMS) (achieved by the single-ATM scheme) to around 25 fs (RMS) [96]. Moreover, the double Arrival Time Monitor (ATM) now provides multi-dimensional information of individual THz pulses such as wavelength, arrival time, and pulse energy. By studying the correlation between the arrival time difference, the pulse frequency, and the pulse energy, a deeper understanding of the origin of accelerator instabilities could be potentially obtained from the analysis of these correlations.

For experiments that require long integration times such as THz ARPES or techniques that need frequency demodulation in coherent detection, such as time-domain THz s-SNOM,

[1] Taking into account the effect of all components in the entire system.

the applicability of the *post mortem* data correction technique is limited, since during the signal integration or demodulation, the arrival time information is lost and cannot be retrieved anymore. In other words, such experiments that need signal integration require *passive synchronization* (not timing accuracy provided by the ATM) between each THz pump pulse and probe laser pulse.

A novel *THz-slicing*-based all-optical passive synchronization method has been developed to realize the *passive synchronization* between the pump THz pulse and probe laser pulse. As described in Chapter 4, the THz-slicing method utilizes a short single-cycle THz pulse to "slice" a portion of the time-stretched laser pulse through EO interaction in an EO crystal, and thereby generates a synchronous *sliced* probe pulse. It is demonstrated in a table-top proof-of-principle experiment that this new method is capable of reducing the timing drift between two independent sources from 1.2 ps to 15 fs – a reduction by two orders of magnitude [106].

Going beyond the proof-of-principle demonstration of the THz-slicing method, three different benchmark experiments have been performed to characterize the *real world* performance of the THz-slicing method at the superradiant THz facility at TELBE, the results of which are described in Chapter 5.

(I) In the benchmark linear THz-TDS experiment, the THz-slicing method was used to characterize the transient electric field of the THz pulses emitted from the accelerator-based TELBE source via EO sampling. As a main result, a jitter reduction from 540 fs (RMS) to 44 fs (RMS) (see Appendix B.2), with a SNR of the order of 10^4 and a dynamic range in the frequency domain of 10^6 was achieved. (II) In the second benchmark experiment, the THz-slicing method was used to measure THz-induced nonlinear processes, more precisely THz HHG in a grating-graphene metamaterial. The experimental results obtained in this experiment turned out to be comparable with those measured using the ATM-based *post mortem* method. Besides, the HHG signal measured with the THz-slicing method shows a high spectral dynamic range of 10^6 – meaning that the detection of weak high harmonics signals in the presence of a strong fundamental background is possible. (III) In a first benchmark experiment, the THz-slicing method was used to perform a THz time-domain s-SNOM experiment. Thereby, it became the key factor enabling *for the first time* THz time-domain s-SNOM at an accelerator-based THz source. In the s-SNOM experiment measuring the optical properties of a Bi_2Se_3 on Si sample, a spatial resolution in the order of 200 nm could be achieved, which is three orders of magnitude smaller than the diffraction limit when the sample is illuminated by a THz pulse with a central frequency of 0.9 THz.

Several new superradiant THz sources have been proposed to enable multicolor pump-probe experiments with intense THz radiation. For instance, a superradiant THz undulator has been proposed at European XFEL that could generate narrowband, CEP stable THz pulses in the range between 3 to 30 THz with pulse energies from 10 to 280 µJ [57]. Another example is the proposal for a new large scale photon facility at HZDR, called Dresden Advanced Light Infrastructure, which plans to implement superradiant THz sources generating narrowband THz pulses in the range of 0.1 to 25 THz with pulse energies from 100 µJ to 1 mJ at repetition rate up to 1 MHz [127]. To perform ultrafast multicolor pump-probe experiments such as THz pump X-ray probe, THz pump XUV probe, or THz pump laser probe, even higher

requirements regarding the synchronization between these sources is required. The THz-based diagnostics methods and the THz-slicing-based passive synchronization method researched in this thesis are hence of high relevance.

References

[1] S. S. Dhillon et al. “The 2017 terahertz science and technology roadmap”. In: *Journal of Physics D: Applied Physics* 50.4 (2017). ISSN: 13616463. DOI: 10.1088/1361-6463/50/4/043001.

[2] E. Bründermann, H.-W. Hübers, and M.F. Kimmitt. *Terahertz techniques*. Springer, Berlin, Heidelberg, (2012). ISBN: 9783642025914. DOI: 10.1007/978-3-642-02592-1.

[3] P.H. Siegel. “THz instruments for space”. In: *IEEE TRANSACTIONS ON ANTENNAS AND PROPAGATION*. Vol. 55. 11. 2007, pp. 2957–2965. DOI: 10.1109/TAP.2007.908557.

[4] P.H. Siegel. “Terahertz technology in biology and medicine”. In: *IEEE Transactions on Microwave Theory and Techniques*. Vol. 52. 10. 2004, pp. 2438–2447. DOI: 10.1109/TMTT.2004.835916.

[5] A.J. Fitzgerald et al. “Terahertz pulsed imaging of human breast tumors”. In: *Radiology* 239.2 (2006), pp. 533–540. DOI: 10.1148/radiol.2392041315.

[6] Tobias Kampfrath, Koichiro Tanaka, and Keith A. Nelson. “Resonant and nonresonant control over matter and light by intense terahertz transients”. In: *Nature Photonics* 7.9 (2013), pp. 680–690. DOI: 10.1038/nphoton.2013.184.

[7] S. Kovalev et al. “Selective THz control of magnetic order: New opportunities from superradiant undulator sources”. In: *Journal of Physics D: Applied Physics* 51.11 (2018). ISSN: 13616463. DOI: 10.1088/1361-6463/aaac75.

[8] J.L. Larue et al. “THz-Pulse-Induced Selective Catalytic CO Oxidation on Ru”. In: *Physical Review Letters* 115 (2015), p. 036103. ISSN: 10797114. DOI: 10.1103/PhysRevLett.115.036103.

[9] J. Federici and L. Moeller. “Review of terahertz and subterahertz wireless communications”. In: *Journal of Applied Physics* 107.11 (2010). ISSN: 00218979. DOI: 10.1063/1.3386413.

[10] E. Heinz et al. “Passive 350 GHz Video Imaging Systems for Security Applications”. In: *Journal of Infrared, Millimeter, and Terahertz Waves* 36.10 (2015), pp. 879–895. DOI: 10.1007/s10762-015-0170-8.

[11] R.J. Falconer and A.G. Markelz. “Terahertz spectroscopic analysis of peptides and proteins”. In: *Journal of Infrared, Millimeter, and Terahertz Waves* 33.10 (2012), pp. 973–988. DOI: 10.1007/s10762-012-9915-9.

[12] V. P. Wallace et al. “Terahertz pulsed imaging of basal cell carcinoma ex vivo and in vivo”. In: *British Journal of Dermatology* 151.2 (2004), pp. 424–432. ISSN: 00070963. DOI: 10.1111/j.1365-2133.2004.06129.x.

[13] T. Kampfrath et al. “Coherent terahertz control of antiferromagnetic spin waves”. In: *Nature Photonics* 5.1 (2011), pp. 31–34. ISSN: 17494885. DOI: 10.1038/nphoton.2010.259.

[14] D. Nicoletti and A. Cavalleri. “Nonlinear light–matter interaction at terahertz frequencies”. In: *Advances in Optics and Photonics* 8.3 (2016), p. 401. DOI: 10.1364/aop.8.000401.

[15] H.A. Hafez et al. “Extremely efficient terahertz high-harmonic generation in graphene by hot Dirac fermions”. In: *Nature* 561.7724 (2018), pp. 507–511. ISSN: 14764687. DOI: 10.1038/s41586-018-0508-1.

[16] A. Rice et al. “Terahertz optical rectification from 110 zinc-blende crystals”. In: *Applied Physics Letters* 64.11 (1994), pp. 1324–1326. ISSN: 00036951. DOI: 10.1063/1.111922.

[17] J. Hebling et al. “Velocity matching by pulse front tilting for large area THz-pulse generation”. In: *Optics Express* 10.21 (2002), p. 1161. ISSN: 1094-4087. DOI: 10.1364/OE.10.001161.

[18] K.Y. Kim et al. “Coherent control of terahertz supercontinuum generation in ultrafast laser-gas interactions”. In: *Nature Photonics* 2.10 (2008), pp. 605–609. ISSN: 17494885. DOI: 10.1038/nphoton.2008.153.

[19] N.T. Yardimci et al. “High-power terahertz generation using large-area plasmonic photoconductive emitters”. In: *IEEE Transactions on Terahertz Science and Technology* 5.2 (2015), pp. 223–229. ISSN: 2156342X. DOI: 10.1109/TTHZ.2015.2395417.

[20] J.A. Fülöp et al. “Efficient generation of THz pulses with 0.4 mJ energy”. In: *Optics Express* 22.17 (Aug. 2014), pp. 20155–20163. DOI: 10.1364/OE.22.020155.

[21] M.C. Hoffmann et al. “Coherent single-cycle pulses with MV/cm field strengths from a relativistic transition radiation light source”. In: *Optics Letters* 36.23 (2011), p. 4473. ISSN: 0146-9592. DOI: 10.1364/ol.36.004473.

[22] Z. Wu et al. “Intense terahertz pulses from SLAC electron beams using coherent transition radiation”. In: *Review of Scientific Instruments* 84.2 (2013). ISSN: 00346748. DOI: 10.1063/1.4790427.

[23] B. Faatz et al. “Development of a pump-probe facility combining a far-infrared source with laser-like characteristics and a VUV free electron laser”. In: *Nuclear Instruments and Methods in Physics Research, Section A: Accelerators, Spectrometers, Detectors and Associated Equipment* 475.1-3 (2001), pp. 363–367. DOI: 10.1016/S0168-9002(01)01540-6.

[24] M. Gensch et al. “New infrared undulator beamline at FLASH”. In: *Infrared Physics and Technology* 51.5 (2008), pp. 423–425. ISSN: 13504495. DOI: 10.1016/j.infrared.2007.12.032.

[25] K. Jung and J. Kim. "Subfemtosecond synchronization of microwave oscillators with mode-locked Er-fiber lasers". In: *Optics Letters* 37.14 (2012), p. 2958. ISSN: 0146-9592. DOI: 10.1364/ol.37.002958.

[26] J. Kim et al. "Long-term femtosecond timing link stabilization using a single-crystal balanced cross-correlator". In: *Conference on Lasers and Electro-Optics, 2007, CLEO 2007* 32.9 (2007), pp. 1044–1046. ISSN: 0146-9592. DOI: 10.1109/CLEO.2007.4452578.

[27] M.Y. Peng et al. "Long-term stable, sub-femtosecond timing distribution via a 1.2-km polarization-maintaining fiber link: approaching 10^{-21} link stability". In: *Optics Express* 21.17 (2013), p. 19982. ISSN: 1094-4087. DOI: 10.1364/OE.21.019982.

[28] A. Azima et al. "Time-resolved pump-probe experiments beyond the jitter limitations at FLASH". In: *Applied Physics Letters* 94.14 (2009). ISSN: 00036951. DOI: 10.1063/1.3111789.

[29] M. Harmand et al. "Achieving few-femtosecond time-sorting at hard X-ray free-electron lasers". In: *Nature Photonics* 7.3 (2013), pp. 215–218. ISSN: 17494885. DOI: 10.1038/nphoton.2013.11.

[30] M.R. Bionta et al. "Spectral encoding method for measuring the relative arrival time between x-ray/optical pulses". In: *Review of Scientific Instruments* 85.8 (2014), p. 083116. ISSN: 10897623. DOI: 10.1063/1.4893657.

[31] M. Diez et al. "A self-referenced in-situ arrival time monitor for X-ray free-electron lasers". In: *Scientific Reports* 11.1 (2021), pp. 1–11. ISSN: 20452322. DOI: 10.1038/s41598-021-82597-3. eprint: 2009.12484.

[32] S. Kovalev et al. "Probing ultra-fast processes with high dynamic range at 4th-generation light sources: Arrival time and intensity binning at unprecedented repetition rates". In: *Structural Dynamics* 4.2 (2017), p. 024301. ISSN: 23297778. DOI: 10.1063/1.4978042.

[33] H. Rubens and R.W. Wood. "Focal isolation of long heat-waves". In: *The London, Edinburgh, and Dublin Philosophical Magazine and Journal of Science* (1911), pp. 249–261. DOI: 10.1080/14786440208637025.

[34] E.K. Plyler, D.J.C. Yates, and H.A. Gebbie. "Radiant Energy from Sources in the Far Infrared". In: *Journal of the Optical Society of America* 52.8 (1962), p. 859. ISSN: 0030-3941. DOI: 10.1364/josa.52.000859.

[35] S.-W. Huang et al. "High conversion efficiency, high energy terahertz pulses by optical rectification in cryogenically cooled lithium niobate". In: *Optics Letters* 38.5 (2013), p. 796. ISSN: 0146-9592. DOI: 10.1364/ol.38.000796.

[36] H.A. Hafez et al. "Intense terahertz radiation and their applications". In: *Journal of Optics* 18.9 (Aug. 2016), p. 093004. DOI: 10.1088/2040-8978/18/9/093004.

[37] A.-S. Müller. "Accelerator-Based Sources of Infrared and Terahertz Radiation". In: *Reviews of Accelerator Science and Technology* 03.01 (2010), pp. 165–183. ISSN: 1793-6268. DOI: 10.1142/s1793626810000427.

[38] N. Stojanovic and M. Drescher. *Accelerator- and laser-based sources of high-field terahertz pulses*. 2013. DOI: 10.1088/0953-4075/46/19/192001.

[39] A. Hofmann. *Reviews of Accelerator Science and Technology.* Vol. 1. World Scientific, (2008), pp. 121–141. ISBN: 978-981-283-520-8.

[40] U. Happek, A. J. Sievers, and E. B. Blum. "Observation of coherent transition radiation". In: *Physical Review Letters* 67.21 (1991), pp. 2962–2965. ISSN: 00319007. DOI: 10.1103/PhysRevLett.67.2962.

[41] A.P. Potylitsyn. "Smith-Purcell effect as resonant diffraction radiation". In: *Nuclear Instruments and Methods in Physics Research, Section B: Beam Interactions with Materials and Atoms* 145.1-2 (1998), pp. 60–66. ISSN: 0168583X. DOI: 10.1016/S0168-583X(98)00016-0.

[42] B. Green. "Superradiant Terahertz Sources and their Applications in Accelerator Diagnostics and Ultra-fast Science". PhD thesis. Karlsruher Institut für Technologie, (2017).

[43] E. Dyunin et al. "A new THz FEL development project". In: *IEEE Convention of Electrical and Electronics Engineers in Israel, Proceedings.* IEEE, (2008), pp. 825–829. ISBN: 9781424424825. DOI: 10.1109/EEEI.2008.4736655.

[44] L.I. Schiff. "Production of particle energies beyond 200 Mev". In: *Review of Scientific Instruments* 17.1 (1946), pp. 6–14. ISSN: 00346748. DOI: 10.1063/1.1770395.

[45] M. Abo-Bakr et al. "Steady-State Far-Infrared Coherent Synchrotron Radiation detected at BESSY II". In: *Physical Review Letters* 88.25 (2002), p. 4. ISSN: 10797114. DOI: 10.1103/PhysRevLett.88.254801.

[46] H.-Ch. Schröder et al. "Bunch length measurement for PETRA III light source storage ring". In: *DIPAC2011.* Hamburg, 2011, pp. 113–115.

[47] M. Abo-Bakr et al. "Brilliant, Coherent Far-Infrared (THz) Synchrotron Radiation". In: *Physical Review Letters* 90.9 (2003), p. 4. ISSN: 10797114. DOI: 10.1103/PhysRevLett.90.094801.

[48] G. Wüstefeld. "Short bunches in electron storage rings and coherent synchrotron radiation". In: *EPAC 2008 - Contributions to the Proceedings.* (2008), pp. 26–30.

[49] J. Andruszkow et al. "First observation of self-amplified spontaneous emission in a free-electron laser at 109 nm wavelength". In: *Physical Review Letters* 85.18 (2000), pp. 3825–3829. ISSN: 00319007. DOI: 10.1103/PhysRevLett.85.3825. eprint: 0006010 (physics).

[50] U. Frühling et al. "Single-shot terahertz-field-driven X-ray streak camera". In: *Nature Photonics* 3.9 (2009), pp. 523–528. ISSN: 17494885. DOI: 10.1038/nphoton.2009.160.

[51] Z. Wu et al. "Intense terahertz pulses from SLAC electron beams using coherent transition radiation". In: *Review of Scientific Instruments* 84.2 (2013). ISSN: 00346748. DOI: 10.1063/1.4790427.

[52] W. Ackermann et al. "Operation of a free-electron laser from the extreme ultraviolet to the water window". In: *Nature Photonics* 1.6 (2007), pp. 336–342. ISSN: 17494885. DOI: 10.1038/nphoton.2007.76.

[53] K. Tiedtke et al. "The soft x-ray free-electron laser FLASH at DESY: Beamlines, diagnostics and end-stations". In: *New Journal of Physics* 11 (2009), p. 023029. ISSN: 13672630. DOI: 10.1088/1367-2630/11/2/023029.

[54] R. Pan et al. "Photon diagnostics at the FLASH THz beamline". In: *Journal of Synchrotron Radiation* 26.3 (2019), pp. 700–707. ISSN: 16005775. DOI: 10.1107/S1600577519003412.

[55] T. Tanikawa et al. "Volt-per-Angstrom terahertz fields from X-ray free-electron lasers". In: *Journal of Synchrotron Radiation* 27 (2020), pp. 796–798. ISSN: 16005775. DOI: 10.1107/S1600577520004245.

[56] G. Penco et al. "Two-bunch operation with ns temporal separation at the FERMI FEL facility". In: *New Journal of Physics* 20 (2018), p. 053047. ISSN: 13672630. DOI: 10.1088/1367-2630/aac059.

[57] T. Tanikawa et al. "A superradiant THz undulator source for XFELs". In: *Journal of Instrumentation* 14.05 (May 2019), P05024–P05024. DOI: 10.1088/1748-0221/14/05/p05024.

[58] Z. Zhang et al. "A high-power, high-repetition-rate THz source for pump-probe experiments at Linac Coherent Light Source II". In: *Journal of Synchrotron Radiation* 27 (2020), pp. 890–901. ISSN: 16005775. DOI: 10.1107/S1600577520005147.

[59] G.L. Carr et al. "High-power terahertz radiation from relativistic electrons". In: *Nature* 420.6912 (2002), pp. 153–156. ISSN: 00280836. DOI: 10.1038/nature01175.

[60] Y. Shen et al. "Nonlinear cross-phase modulation with intense single-cycle terahertz pulses". In: *Physical Review Letters* 99.4 (2007), pp. 1–4. ISSN: 00319007. DOI: 10.1103/PhysRevLett.99.043901.

[61] X. Wen et al. "Superradiant THz undulator radiation source based on a superconducting photo-injector". In: *Nuclear Instruments and Methods in Physics Research, Section A: Accelerators, Spectrometers, Detectors and Associated Equipment* 820 (2016), pp. 75–79. ISSN: 01689002. DOI: 10.1016/j.nima.2016.03.003.

[62] B. Green et al. "High-Field High-Repetition-Rate Sources for the Coherent THz Control of Matter". In: *Scientific Reports* 6 (2016), p. 22256. ISSN: 2045-2322. DOI: 10.1038/srep22256.

[63] J. Teichert et al. "Successful user operation of the superconducting radio-frequency photo electron gun with Mg cathodes at ELBE J." In: *Physical Review Accelerators and Beams* 24 (2021), p. 033401. DOI: 10.1103/PhysRevAccelBeams.24.033401.

[64] M. Kuntzsch. "Optische Synchronisation am cw-Beschleuniger ELBE." PhD Thesis. Technische Universität Dresden, 2015.

[65] S. Schulz et al. "Femtosecond all-optical synchronization of an X-ray free-electron laser". In: *Nature Communications* 6 (2015), p. 5938. ISSN: 20411723. DOI: 10.1038/ncomms6938.

[66] Coherent Synchrolock-AP. URL: https://www.coherent.com/lasers/laser/synchrolock-ap.

[67] S. Kovalev. Personal communication.

[68] P. Evtushenko. "Electron Beam Diagnostic at the ELBE Free Electron Laser". PhD thesis. Technische Universität Dresden, 2004.

[69] J.D. Jackson. *Classical Electrodynamics*. Third Edition. Wiley, 2012.

[70] K. Satoh. "New beam postion monitor by detecting wall currents". In: *Review of Scientific Instruments* 50.4 (1979), pp. 450–453. ISSN: 00346748. DOI: 10.1063/1.1135849.

[71] P. Rov et al. "New higher-brilliance sources of infrared synchrotron radiation". In: *Nouv Cim D* 20 (1998), pp. 415–437. ISSN: 03926737. DOI: 10.1007/bf03185539.

[72] M. Beye et al. "X-ray pulse preserving single-shot optical cross-correlation method for improved experimental temporal resolution". In: *Applied Physics Letters* 100.12 (2012), pp. 1–5. ISSN: 00036951. DOI: 10.1063/1.3695164.

[73] Y.-S. Lee. *Principles of Terahertz Science and Technology*. Springer US, (2009). ISBN: 9780387095400.

[74] S. Wesch et al. "A multi-channel THz and infrared spectrometer for femtosecond electron bunch diagnostics by single-shot spectroscopy of coherent radiation". In: *Nuclear Instruments and Methods in Physics Research, Section A: Accelerators, Spectrometers, Detectors and Associated Equipment* 665 (2011), pp. 40–47. ISSN: 01689002. DOI: 10.1016/j.nima.2011.11.037. eprint: 1109.0458.

[75] DIAS Infrared GmbH. *Pyroelectric infrared detectors*. (accessed 17 September 2020). 2006. URL: http://www.dias-infrared.de/pdf/basics_eng.pdf.

[76] R.W. Boyd. *Nonlinear Optics*. Third Edition. USA: Academic Press, Inc., (2008). ISBN: 0123694701.

[77] Q. Wu and X.-C. Zhang. "Free-space electro-optic sampling of terahertz beams". In: *Applied Physics Letters* 67.1995 (1995), p. 3523. ISSN: 00036951. DOI: 10.1063/1.114909.

[78] G. Gallot et al. "Measurements of the THz absorption and dispersion of ZnTe and their relevance to the electro-optic detection of THz radiation". In: *Applied Physics Letters* 74.23 (1999), p. 3450. ISSN: 00036951. DOI: 10.1063/1.124124.

[79] Z. Jiang and X.-C Zhang. "Electro-optic measurement of THz field pulses with a chirped optical beam". In: *Applied Physics Letters* 72 (1998), p. 1945. DOI: 10.1063/1.121231.

[80] S.M. Teo et al. "Invited Article: Single-shot THz detection techniques optimized for multidimensional THz spectroscopy". In: *Review of Scientific Instruments* 86 (2015). ISSN: 10897623. DOI: 10.1063/1.4921389.

[81] B. Yellampalle et al. "Algorithm for high-resolution single-shot THz measurement using in-line spectral interferometry with chirped pulses". In: *Applied Physics Letters* 87.21 (2005), pp. 1–3. ISSN: 00036951. DOI: 10.1063/1.2135869.

[82] S.P. Jamison et al. "Temporally resolved electro-optic effect". In: *Optics Letters* 31.11 (2006), pp. 1753–1755. DOI: 10.1364/OL.31.001753.

[83] X.-Y. Peng et al. “Distortion analysis of pulsed terahertz signal measured with spectral-encoding technique”. In: *Journal of Applied Physics* 108 (2010). DOI: 10.1063/1.3499639.

[84] R. Lai and A.J. Sievers. “On using the coherent far IR radiation produced by a charged-particle bunch to determine its shape: I Analysis”. In: *Nuclear Instruments and Methods in Physics Research, Section A: Accelerators, Spectrometers, Detectors and Associated Equipment* 397.2-3 (1997), pp. 221–231. ISSN: 01689002. DOI: 10.1016/S0168-9002(97)00690-6.

[85] D. Mihalcea et al. “Longitudinal electron bunch diagnostics using coherent transition radiation”. In: *Physical Review Special Topics - Accelerators and Beams* 9 (2006), p. 082801. ISSN: 1098-4402. DOI: 10.1103/physrevstab.9.082801.

[86] F.G. Sun, Z. Jiang, and X.-C. Zhang. “Analysis of terahertz pulse measurement with a chirped probe beam”. In: *Applied Physics Letters* 73 (1998), pp. 2233–2235. ISSN: 00036951. DOI: 10.1063/1.121685.

[87] I. Wilke et al. “Single-Shot Electron-Beam Bunch Length Measurements”. In: *Physical Review Letters* 88 (2002), p. 124801. ISSN: 0031-9007. DOI: 10.1103/PhysRevLett.88.124801.

[88] B.R. Steffen. “Electro-Optic Methods for Longitudinal Bunch Diagnostics at FLASH”. PhD thesis. Universität Hamburg, (2007). DOI: 10.3204/DESY-THESIS-2007-020.

[89] A.L. Cavalieri et al. “Clocking Femtosecond X Rays”. In: *Physical Review Letters* 94 (2005), p. 114801. DOI: 10.1103/PhysRevLett.94.114801.

[90] A.A. Zholents and M.S. Zolotorev. “Femtosecond X-ray pulses of synchrotron radiation”. In: *Physical Review Letters* 76 (1996), pp. 912–915. ISSN: 10797114. DOI: 10.1103/PhysRevLett.76.912.

[91] R.W. Schoenlein. “Generation of Femtosecond Pulses of Synchrotron Radiation”. In: *Science* 287.5461 (2000), pp. 2237–2240. ISSN: 00368075. DOI: 10.1126/science.287.5461.2237.

[92] M. Ferianis et al. “How the optical timing system, the longitudinal diagnostics and the associated feedback systems provide femtosecond stable operation at the FERMI free electron laser”. In: *High Power Laser Science and Engineering* 4 (2016), pp. 1–15. ISSN: 20523289. DOI: 10.1017/hpl.2016.6.

[93] M.B. Danailov et al. “Towards jitter-free pump-probe measurements at seeded free electron laser facilities”. In: *Optics Express* 22.11 (2014), pp. 12869–12879. ISSN: 1094-4087. DOI: 10.1364/oe.22.012869.

[94] P. Cinquegrana et al. “Optical beam transport to a remote location for low jitter pump-probe experiments with a free electron laser”. In: *Physical Review Accelerators and Beams* 17.4 (2014). ISSN: 10984402. DOI: 10.1103/PhysRevSTAB.17.040702.

[95] H. Chu et al. “Phase-resolved Higgs response in superconducting cuprates”. In: *Nature Communications* 11 (2020), p. 1793. ISSN: 20411723. DOI: 10.1038/s41467-020-15613-1.

[96] M. Chen et al. “Pulse- and field-resolved THz-diagnostics at 4th generation lightsources”. In: *Optics Express* 27.22 (2019), p. 32360. ISSN: 1094-4087. DOI: 10.1364/oe.27.032360.

[97] Z. Jiang et al. “Electro-optic sampling near zero optical transmission point”. In: *Applied Physics Letters* 74.9 (1999), pp. 1191–1193. ISSN: 00036951. DOI: 10.1063/1.123495.

[98] Basler Line Scan Camera. URL: https://www.baslerweb.com/en/products/cameras/line-scan-cameras/.

[99] E. Savelyev et al. “Jitter-correction for IR/UV-XUV pump-probe experiments at the FLASH free-electron laser”. In: *New Journal of Physics* 19 (2017). ISSN: 13672630. DOI: 10.1088/1367-2630/aa652d.

[100] Teledyne Digital Imaging Inc. 2021. URL: https://www.teledynedalsa.com/en/products/imaging/cameras/linea-hs/.

[101] J. Reimann et al. *Subcycle observation of lightwave-driven Dirac currents in a topological surface band*. 2018. DOI: 10.1038/s41586-018-0544-x.

[102] M. Eisele et al. “Ultrafast multi-terahertz nano-spectroscopy with sub-cycle temporal resolution”. In: *Nature Photonics* 8.11 (2014), pp. 841–845. ISSN: 17494893. DOI: 10.1038/nphoton.2014.225.

[103] B.E.A Saleh and M.C. Teich. *Fundamentals of photonics*. Third Edition. John Wiley Sons, Inc., (2019). ISBN: 9780471839651.

[104] A. Nahata, A.S. Weling, and T.F. Heinz. “A wideband coherent terahertz spectroscopy system using optical rectification and electro-optic sampling”. In: *Citation: Appl. Phys. Lett* 69 (1996). DOI: 10.1063/1.117511.

[105] F. Blanchard et al. “Generation of 1.5 µJ single-cycle terahertz pulses by optical rectification from a large aperture ZnTe crystal”. In: *Optics Express* 15.20 (2007), p. 13212. ISSN: 1094-4087. DOI: 10.1364/oe.15.013212.

[106] M. Chen et al. “Towards femtosecond-level intrinsic laser synchronization at fourth generation light sources”. In: *Optics Letters* 43.9 (2018), pp. 2213–2216. ISSN: 0146-9592. DOI: 10.1364/OL.43.002213.

[107] F. Tavella et al. “Few-femtosecond timing at fourth-generation X-ray light sources”. In: *Nature Photonics* 5.3 (2011), pp. 162–165. ISSN: 1749-4885. DOI: 10.1038/nphoton.2010.311.

[108] H. Redlin et al. “The FLASH pumpprobe laser system: Setup, characterization and optical beamlines”. In: *Nuclear Instruments and Methods in Physics Research, Section A: Accelerators, Spectrometers, Detectors and Associated Equipment* 635.1 (2011), s88–s93. ISSN: 01689002. DOI: 10.1016/j.nima.2010.09.159.

[109] J.-C. Deinert et al. “Grating-graphene metamaterial as a platform for terahertz nonlinear photonics”. In: *ACS Nano* 15.1 (2020), pp. 1145–1154. DOI: 10.1021/acsnano.0c08106. eprint: 2009.11730.

[110] K.S. Novoselov et al. “Two-dimensional gas of massless Dirac fermions in graphene”. In: *Nature* 438.7065 (2005), pp. 197–200. ISSN: 00280836. DOI: 10.1038/nature04233.

[111] A.H. Castro Neto et al. "The electronic properties of graphene". In: *Reviews of Modern Physics* 81 (2009), p. 109. ISSN: 00346861. DOI: 10.1103/RevModPhys.81.109. arXiv: 0709.1163.

[112] S. Das Sarma et al. "Electronic transport in two-dimensional graphene". In: *Reviews of Modern Physics* 83 (2011), p. 407. ISSN: 00346861. DOI: 10.1103/RevModPhys.83.407. eprint: 1003.4731.

[113] T.L. Cocker et al. "Nanoscale terahertz scanning probe microscopy". In: *Nature Photonics* 15.8 (2021), pp. 558–569. ISSN: 1749-4885. DOI: 10.1038/s41566-021-00835-6.

[114] T. Kiwa et al. "Laser terahertz-emission microscope for inspecting electrical faults in integrated circuits". In: *Optics Letters* 28.21 (Nov. 2003), pp. 2058–2060. DOI: 10.1364/OL.28.002058.

[115] Y. Kawano and K. Ishibashi. "An on-chip near-field terahertz probe and detector". In: *Nature Photonics* 2.10 (2008), pp. 618–621. ISSN: 17494885. DOI: 10.1038/nphoton.2008.157.

[116] X. Chen et al. "Modern Scattering-Type Scanning Near-Field Optical Microscopy for Advanced Material Research". In: *Advanced Materials* 31.24 (2019), p. 1804774. ISSN: 15214095. DOI: 10.1002/adma.201804774.

[117] M. Wagner et al. "Ultrafast and nanoscale plasmonic phenomena in exfoliated graphene revealed by infrared pump-probe nanoscopy". In: *Nano Letters* 14.2 (2014), pp. 894–900. ISSN: 15306984. DOI: 10.1021/nl4042577.

[118] M.A. Huber et al. "Femtosecond photo-switching of interface polaritons in black phosphorus heterostructures". In: *Nature Nanotechnology* 12.3 (2017), pp. 207–211. ISSN: 17483395. DOI: 10.1038/nnano.2016.261.

[119] Z. Yao et al. "Nanoimaging and Nanospectroscopy of Polaritons with Time Resolved s-SNOM". In: *Advanced Optical Materials* 8.5 (2020), pp. 1–18. ISSN: 21951071. DOI: 10.1002/adom.201901042.

[120] G. Wurtz, R. Bachelot, and P. Royer. "Imaging a GaAlAs laser diode in operation using apertureless scanning near-field optical microscopy". In: *EPJ Applied Physics* 5.3 (1999), pp. 269–275. ISSN: 12860042. DOI: 10.1051/epjap:1999139.

[121] B. Knoll and F. Keilmann. "Enhanced dielectric contrast in scattering-type scanning near-field optical microscopy". In: *Optics Communications* 182.4-6 (2000), pp. 321–328. ISSN: 0030-4018. DOI: https://doi.org/10.1016/S0030-4018(00)00826-9.

[122] R. Hillenbrand and F. Keilmann. "Complex optical constants on a subwavelength scale". In: *Physical Review Letters* 85 (2000), pp. 3029–3032. ISSN: 00319007. DOI: 10.1103/PhysRevLett.85.3029.

[123] C.E. Shannon. "Communication Theory in the presence of Noise". In: *Proceedings of the IRE* 37.1 (1949), pp. 10–21. ISSN: 0018-9219. DOI: 10.1109/JRPROC.1949.232969.

[124] H. Wang, L. Wang, and X.G. Xu. "Scattering-type scanning near-field optical microscopy with low-repetition-rate pulsed light source through phase-domain sampling". In: *Nature Communications* 7 (2016), p. 13212. ISSN: 20411723. DOI: 10.1038/ncomms13212.

[125] T.V.A.G. de Oliveira et al. “Nanoscale-confined terahertz polaritons in a van der Waals crystal”. In: *Advanced Materials* 33.2 (2021). ISSN: 15214095. DOI: 10.1002/adma.202005777.

[126] X. Chen et al. “THz Near-Field Imaging of Extreme Subwavelength Metal Structures”. In: *ACS Photonics* 7.3 (2020), pp. 687–694. ISSN: 23304022. DOI: 10.1021/acsphotonics.9b01534.

[127] *Dresden Advanced Light Infrastructure Pre-Conceptional Design Report*. 2020.

A

Adjustable Undulator-laser pulse jitter

As described in Section 2.2 (see Figure 2.9). The last step of the synchronization system between the laser and the electron bunch, as well as the THz pulse, is achieved by the Synchrolock. The undulator-laser jitter can be adjusted by the "Gain" value of the Synchrolock device (See Section 2.2 for details) from 500 fs to 5 ps (RMS).

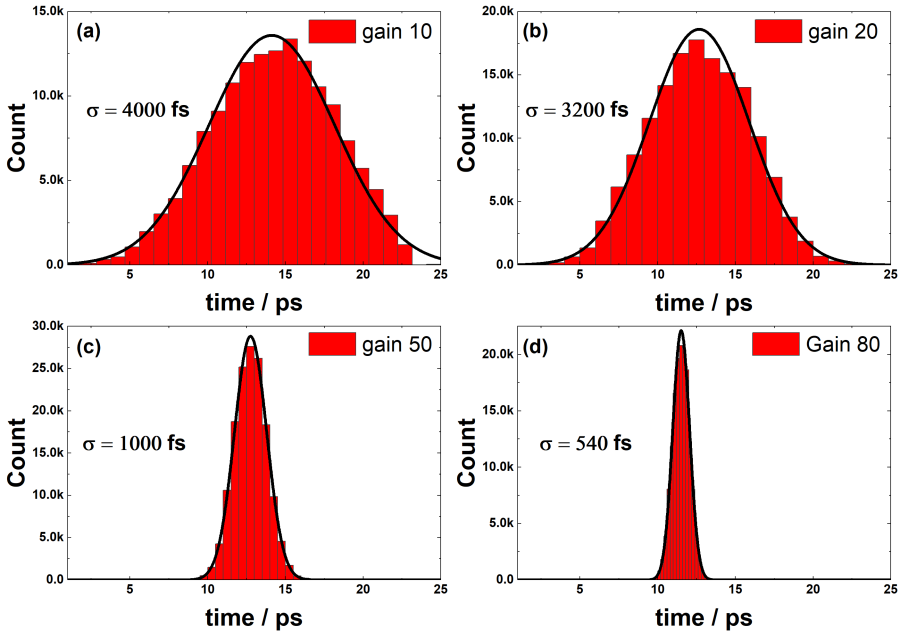

Figure A.1: Undulator-laser jitter measurement measurement at different Synchrolock settings. (a), (b), (c) and (d) are the histograms of the arrival time measured by the ATM when the gain values of the Synchrolock are set to 10, 20, 50 and 80, respectively. The black curves are the fitted Gaussian distributions of arrival time distributions. The standard deviation of the arrival time distributions are calculated to be 4000 fs, 3200 fs, 1000 fs and 540 fs under each Synchrolock setting. Please note, that each histogram contains 150 000 events.

Figure A.1 shows the arrival time distribution measured by the ATM when the gain[1] of the Synchrolock is set to values of 10, 20, 50, and 80. These settings are corresponding to

[1] A setting of the commercial Synchrolock from Coherent, Inc.

undulator-laser jitter values of 4000 fs (RMS), 3200 fs (RMS), 1000 fs (RMS) and 540 fs (RMS), respectively, which were obtained by fitting Gaussian distributions as shown in the figure. Using this feature, the Synchrolock can be used to set different undulator-laser jitter level according to the needs of experiments.

B

Limitations of the THz-slicing method

B.1 Sliced pulse duration limited higher cutoff frequency in THz-TDS

In order to show the higher cutoff frequency in EO sampling induced by the sliced pulse duration, the 5th harmonics of the undulator radiation (fundamental frequency is 300 GHz) is measured. Please note, one 1.5 THz BP filter is inserted into the undulator radiation beam path. As shown by Figure B.1(b), instead of showing a peak at 1.5 THz, a sharp signal drop appears at around 1.5 THz indicating a cutoff frequency around 1.5 THz. This limited bandwidth of the EO sampling measurement can be attributed to the relatively long 150 fs (RMS) (corresponding to 353 fs (FWHM)) pulse duration of the sliced pulse. For details about the relationship between the spectral response of the EO sampling method and the probe pule (sliced pulse) duration, please refer to Equation 2.15 and Figure 2.21 in Chapter 2.

To increase the higher cutoff frequency, the pulse duration of the sliced pulse needs to be shorted. One possible solution is to compress the sliced pulse by means of dispersion compensation. However, the complexity of the sliced pulse spectrum (see Section 4.5) could make the compression very difficult. Therefore, the pulse compression can only be applied in combination with the Fourier-transform limit pulse instead of the chirped pulse, as the Fourier-transform limit pulse has much fewer frequency components and is much easier to compress. Another solution is to use the THz gate pulse that has higher peak electric-field strength and shorter pulse duration.

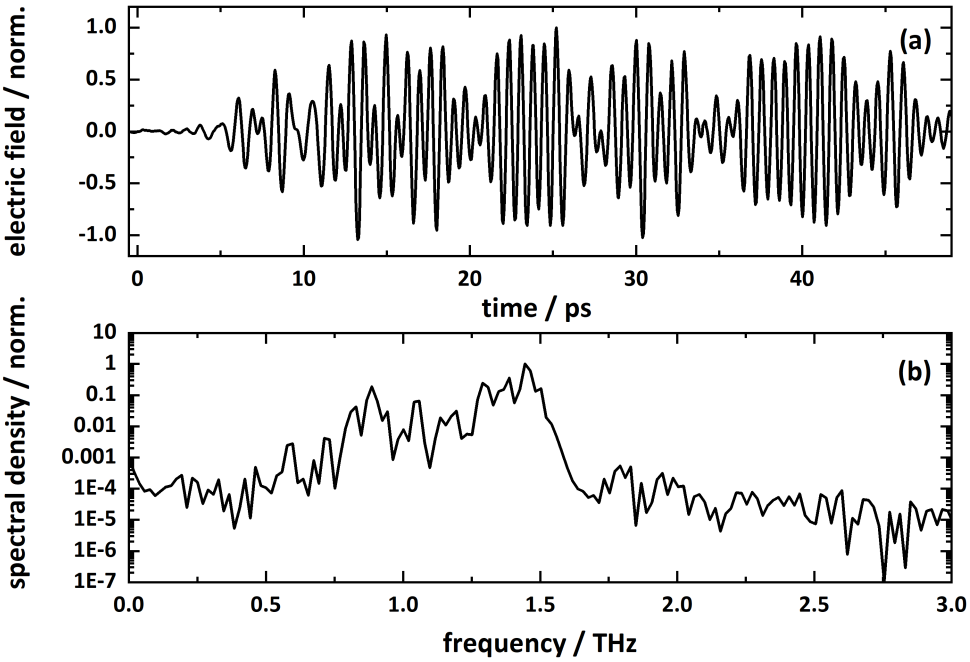

Figure B.1: Electric field waveform of the undulator pulse measured by EO sampling in associated with sliced pulse with one 1.5 THz BP filter (short scan). (a) THz electric waveform measured by EO sampling using the passive synchronization technique with one 1.5 THz BP filter. (b) The spectrum of the THz electric waveform. (Spectrum is obtained by Fourier transformation.)

B.2 Residual jitter of the THz-slicing method

Even though the jitter between the sliced pulse and the undulator pulse is very small, the dispersion of the sliced pulse still induces some residual jitter in the case of the THz-slicing technique, as previously discussed in Section 4.5.

The residual jitter was characterized by measuring the electric field strength fluctuation at one zero-field position of the THz pulse (i.e., by fixing the position of the delay line mirror). Recalling the principle of EO sampling shown in Figure 2.20, ideally, when there is no jitter between the THz and the laser pulse, the signal fluctuation should constantly be zero. However, with the existence of residual jitter, a fluctuation of the signal strength is expected to occur. The residual jitter can be quantitatively measured from the distribution of the fluctuating signal by converting this intensity distribution into *temporal fluctuation (residual jitter)* via the known THz electric field gradient ∇E_{zero} at the chosen zero-field position.

A schematic view of the measurement principle can be seen in Figure B.2. During the measurement, the delay is fixed at the zero-field position. The residual jitter σ_t can be deduced from the relationship $\sigma_t = \sigma_s / \nabla E_{\text{zero}}$, where σ_s is the average RMS distribution of the signal when the delay line is fixed at a zero-field position and ∇E_{zero} is the local gradient of the THz electric field.

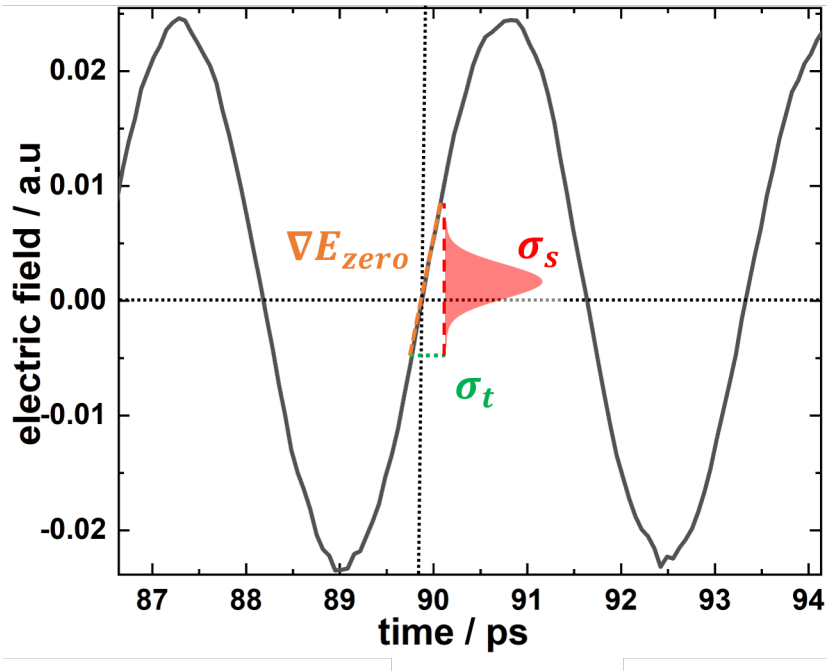

Figure B.2: Principle of the residual jitter determination of the THz-slicing technique. The black curve is the undulator pulse measured by EO sampling with the sliced pulse. Two orthogonal black dashed lines indicate the zero-field position where the probe pulse is fixed. σ_s (in red) is the RMS distribution of the signal. ∇E_{zero} (in orange) is the gradient of the THz field at one zero-field position. σ_t (in green) is the residual jitter. The dash lines in orange, red and green indicate the geometric relationship between σ_s, ∇E_{zero} and σ_t.

In an actual experiment, the signal of the EO sampling is measured at a set of delay positions around the zero-field position to measure both the fluctuations and gradient of the signal (see Figure B.3). At each delay position, more than 3×10^5 pulses are measured. As shown by Figure B.3, the standard deviation σ_{s_n} of the fluctuated signals are calculated for each delay position n. From the linear fit (the green dash line in Figure B.3) of the mean signal values at each delay position, $\nabla E_{\text{zero}} = 0.29\,\text{ps}^{-1}$ can be deduced. By dividing the signal standard distribution at the "zero-crossing" position $\sigma_{s_0} = 0.013$ (indicated by the black arrow in Figure B.3) with ∇E_{zero}, a residual jitter (shot-to-shot) of 44 fs (RMS) can be obtained. Please note, the 44 fs (RMS) residual jitter is a reference value under specific condition but not the ultimate jitter compensation ability of the THz-slicing method, as the jitter calculation involves lots of instabilities and jitter of the accelerator such as intensity fluctuation of the CDR pulse and the undulator-CDR jitter. The ultimate jitter compensation ability of THz-slicing method, please refer to Section 4.5.

Though the 44 fs (RMS) is larger than the 25 fs (RMS) achieved by the double-ATM-based arrival time correction method (without considering the operation parameter difference of the accelerator), it is still sufficient for most of the experiments and foreseeable optimization could decrease the jitter further. The estimated 44 fs jitter is a top-down estimation including all the possible noises, and the real timing jitter can be several times smaller.

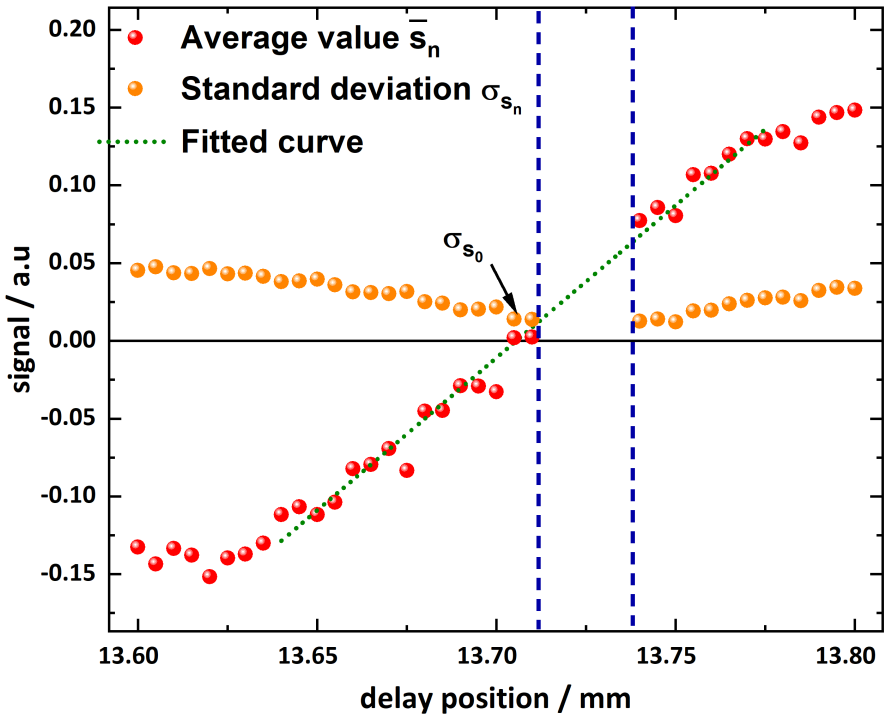

Figure B.3: Residual jitter determination of THz-slicing technique. The orange and red dots represent the standard deviation and the signal's mean value at each specific delay line position, respectively. The Green dashed line is the fitted curve of the average values within the half-cycle range of the undulator pulse. The black arrow indicates the data point at the "zero-field" position. Please note, no data is measured in the interval between two blue dash lines because of the malfunction of the optical delay line.

C

List of publications

PUBLICATIONS IN REFEREED JOURNALS

- **M. Chen**, S. Kovalev, N. Awari, Z. Wang, S. Germanskiy, B. Green, J.-C. Deinert, and M. Gensch. "Towards femtosecond-level intrinsic laser synchronization at fourth generation light sources". In: Optics Letters 43.9 (2018), p. 2213. ISSN: 0146-9592. DOI:10.1364/OL.43.002213.

- **M. Chen**, J.-C. Deinert, B. Green, Z. Wang, I. Ilyakov, N. Awari, M. Bawatna, S. Germanskiy, T. V. A. G. de Oliveira, G. Geloni, T. Tanikawa, M. Gensch, and S. Kovalev. "Pulse- and field-resolved THz-diagnostics at 4 t h generation lightsources". In: Optics Express 27.22 (2019), p. 32360. ISSN: 1094-4087. DOI: 10.1364/oe.27.032360.

- S. Kovalev, K.-J. Tielrooij, J.-C. Deinert, I. Ilyakov, N. Awari, **M. Chen**, A. Ponomaryov, M. Bawatna, T.V.A.G de Oliveira, L.M. Eng, K.A. Kuznetsov, D.A. Safronenkov, G.Kh. Kitaeva, P.I. Kuznetsov, H.A. Hafez, D. Turchinovich and M. Gensch. "Terahertz signatures of ultrafast Dirac fermion relaxation at the surface of topological insulators at room temperature," In: npj Quantum Materials. 6, 84 (2021). DOI: 10.1038/s41535-021-00384-9.

- I.E. Ilyakov, B.V. Shishkin, V.L. Malevich, D.S. Ponomarev, R.R. Galiev, A. Yu. Pavlov, A.E. Yachmenev, S.P. Kovalev, **M. Chen**, R.A. Akhmedzhanov, and R.A. Khabibullin, "Efficient optical-to-terahertz conversion in large-area InGaAs photo-Dember emitters with increased indium content," In: Optics Letters 46(2021), p. 3360. ISSN: 0146-9592. DOI: 10.1364/OL.428599.

- S. Kovalev, H.A. Hafez, K.-J. Hielrooij, J.-C. Deinert, I. Ilyakov, N. Awari, D. Alcaraz, K. Soundarapandian, D. Saleta, S. Germanskiy, **M. Chen**, M. Bawatna, B. Green, F.H.L. Koopens, M. Mittendorff, M. Bonn, M.Gensch and D. Turchinovich. "Electrical tunability of terahertz nonlinearity in graphene," In: Science Advances, vol. 7, no. 15, (2021), DOI: 10.1126/sciadv.abf9809.

- K. Neeraj, N. Awari, S. Kovalev, D. Polley, N.Z. Hagström, SSPK. Arekapudi, A. Semisalova, K. Lenz, B. Green, J.-C. Deinert, I. Ilyakov, **M. Chen**, M. Bawatna, V. Scalera, M. d'Aquinl, C. Serpico, O. Hellwig, J.-E Wegrowe, M. Gensch and S. Bonetti. "Inertial spin dynamics in ferromagnets". In: Nat. Phys. 17, 245–250 (2021). DOI: 10.1038/s41567-020-01040-y.

- H. Chu, M.-J Kim, K. Katsumi, S. Kovalev, R.D. Dawson, L. Schwarz, N. Yoshikawa, G.K. Putzky, Z. Li, H. Raffy, S. Germanskiy, J.-c. Deinert, N. Awari, I. Ilyakov, B. Green, **M. Chen**, M. Bawatna, G. Cristiani, G. Logvenov, Y. Gallais, A.V. Boris, B. Keimer, A.P. Schnyder,D. Manske, M. Gensch, Z. Wang, R. Shimano and S. Kaiser. "Phase-resolved Higgs response in superconducting cuprates," In: Nat. Commun., vol. 11, no. 1, pp. 6–11 (2020), DOI: 10.1038/s41467-020-15613-1.

- J.-C. Deinert, D. A. Iranzo, R. Pérez, X. Jia, H.A. Hafez, I. Ilyakov, N. Awari, **M. Chen**, M. Bawatna, A.N. ponomaryov, S. Germanskiy, M. Bonn, F.H.L. Koppens, D. Turchinovich, M. Gensch, S. Kovalev and K.-J. Tielrooij. "Grating-graphene metamaterial as a platform for terahertz nonlinear photonics". In: ACS Nano 15, 1, 1145–1154 (2020). DOI: 10.1021/acsnano.0c08106.

- S. Kovalev, R.M.A. Dantas, S. Germanskiy, J.-C Deinert, B. Green, I. Ilyakov, N. Awari, **M. Chen**, M. Bawatna, J. Ling, F. Xiu, P.H.M. van Loosdrecht, P. Surówka, T. Oka and Z. Wang. "Non-perturbative terahertz high-harmonic generation in the three-dimensional Dirac semimetal Cd_3As_2," In: Nat. Commun., vol. 11, no. 1, pp. 6–11 (2020), DOI: 10.1038/s41467-020-16133-8.

- H.A. Hafez, S. Kovalev, J.-C. Deinert, Z. Mics, B. Green, N. Awari, **M. Chen**, S. Germanskiy, U. Lehnert, J. Teichert, Z. Wang, K.-J. Tielrooij, Z. Liu, Z. Chen, A. Narita, K. Müller, M. Bonn, M. Gensch and D. Turchinovich. "Extremely efficient terahertz high-harmonic generation in graphene by hot Dirac fermions". In: Nature 561.7724 (2018), pp. 507–511. ISSN:14764687. DOI: 10.1038/s41586-018-0508-1.

- S. Kovalev, Z. Wang, J.-C. Deinert, N. Awari, **M. Chen**, B. Green, S. Germanskiy, TVAG de Oliveira, J.S. Lee, A. Deac, D. Turchinovich, N. Stojanovic, S. Eisebitt, I. Radu, S. Bonetti, T. Kampfrath and M. Gensch. "Selective THz control of magnetic order: New opportunities from superradiant undulator sources," In: J. Phys. D. Appl. Phys., 51 114007 (2018). ISSN:13616463. DOI: 10.1088/1361-6463/aaac75.

- Z. Wang, S. Kovalev, N. Awari, **M. Chen**, S. Germanskiy, J.-C. Deinert, T. Kampfrath, J. Milano and M. Gensch. "Magnetic field dependence of antiferromagnetic resonance in NiO," In: Appl. Phys. Lett., vol. 112, no. 25, p. 252404, (2018), DOI: 10.1063/1.5031213.

CONFERENCE PAPER

- **M. Chen** et al., "Pulse and field-resolved photon diagnostics at a superradiant THz user facility," In: 44th International Conference on Infrared, Millimeter, and Terahertz Waves (IRMMW-THz), Paris, France (2019), pp. 1-1, DOI: 10.1109/IRMMW-THz.2019.8873872.